

Chapter 2

Dense Plasma Focus—High-Energy-Density Pulsed Plasma Device Based Novel Facility for Controlled Material Processing and Synthesis

Rajdeep Singh Rawat

2.1 Introduction

Plasma, a term that Irving Langmuir ascribed in 1928 to a volume of ionized gas, consists of positive and negative charge particles and neutrals which are generated from the physical process of gas discharge or ionization of a gas. Plasma seems simple as it is largely governed by physical laws known to nineteenth-century physicists. Yet the sophisticated and often mysterious behavior of plasma is anything but simple. One of the greatest virtues of plasma is that this seemingly simple ionized fluid exhibits bewildering variety and complexity. Currently, the plasma science is at the edge of embarking into a new era where is poised to make significant breakthroughs in next decade in the field of nuclear fusion research which uses the high-temperature high-density plasmas. For example, the International Thermonuclear Experimental Reactor (ITER), currently being built at Cadarache, France with huge international collaboration, is expected to go for deuterium–tritium operation [1] with full-scale electricity-producing fusion reactor while the National Ignition Facility (NIF), US aims to ignite the fusion capsule [2]; as a critical step to commercial fusion in future. At the same time, the low-temperature plasma applications are already creating new products and techniques that are changing our everyday lives.

The ever-expanding scope of plasma science and technology is creating a plethora of new scientific opportunities and challenges. The plasma science and technologies are playing increasingly important and critical roles in the economy, energy security, energy efficiency, environmental safety, health care and fundamental scientific knowledge and discoveries.

R.S. Rawat (✉)

National Institute of Education, Nanyang Technological University,
Singapore 637616, Singapore
e-mail: rajdeep.rawat@nie.edu.sg

- *Economy and Plasmas*: The economic impact of plasmas is evident through its extensive use in etching tiny features onto a semiconductor wafer for micro-electronic industry. The semiconductor industry uses plasmas for surface hardening, texturing or coating and simply cannot exist without the support of plasma science and technology. The low-temperature cold plasmas have also established a market base in several industries that include textile industry (finishing, printing, and sterilization), polymer and paper industry (surface treatment, printability, and adhesion), and food and agriculture industry (packaging decontamination, food surface decontamination, seed germination and wastewater treatment).
- *Energy Security*: The thermonuclear fusion using hot dense deuterium plasmas has been identified as one of the future sustainable and clean energy source to provide energy security for mankind. Great progress has been made in heating and confinement of plasmas for fusion and according to ITER's timeline; it will start exploring deuterium–tritium plasmas by 2027. The success of these experiments will very much decide the fate of fusion as long-term energy security for mankind.
- *Energy-Efficient Processes*: The plasma science is also contributing to innovations in energy-efficient technologies for various applications. The energy that is not consumed does not have to be generated! Plasma-based processes are replacing old energy-intensive manufacturing processes with new energy-efficient processes. For example, the drying stage in conventional, wet chemistry processes consumes many times more energy compared to the dry, inline plasma process through energy-efficient surface pretreatment. Similarly, material synthesis and processing using plasma-assisted or plasma-enhanced approaches are energy- and cost-efficient. Another example of higher energy efficiency of the plasma-based product is that of plasma lighting system (plasma lamp). It is a proven fact that the plasma lighting systems have a longer life, higher efficacy, better lumen maintenance, improved color rendering, and enhanced dimming performance compared to conventional high-intensity discharge lighting systems. Even compared to the new technology of light-emitting diode systems, the plasma lighting systems have higher light output and lower overall system price while maintaining a small optical package and high system efficiency.
- *Environmental Applications*: There is a growing use of plasmas for various environmental applications. These applications mostly include air pollutant treatment, wastewater and drinking water decontamination, and thermal disposal of solid waste using thermal and non-thermal plasmas (defined later). These applications exploit the ability of plasmas, which is composed of excited species, free radicals, electrons, ions and/or UV photons, to break down harmful chemicals and kill microbes to purify water and destroy pollutants.
- *Biomedical Applications*: The biomedical applications of plasmas in healthcare industry is on the rise with plasmas being used for sterilization, surface treatment of human implants, plasma-aided surgery and more recently for plasma cosmetics. Plasmas are a rich source of reactive neutral species and UV light which can destroy biological activity providing local sterilization. Plasma

treatment also makes surgical implants biocompatible by either depositing material or modifying the surface of the implant. The plasma knives (plasma streamers) are already in use for long to cut and cauterize tissue. More recently, the cold plasma jet is now being used for the cosmetic purpose for the treatment of facial skin to make it brighter, clearer and tighter. The other applications include wound healing, blood coagulation, dentistry, cancer treatment, and others.

- *Contribution to Other Sciences and Discoveries:* In addition, the development and studies in plasma science have also bred new avenues of basic science. Plasma physicists were among the first to open up and develop the new and profound science of chaos and nonlinear dynamics which has found its applications in many fields that include electronics, robotics, fluid dynamics, communication, etc. Plasma science has also contributed greatly to studies of wave phenomena, instabilities, and turbulences, important for flow, transport, and other applications. In addition, new discoveries in understanding extremely cold plasmas created from laser-cooled atoms are unleashing a flood of new ideas in atomic physics, particle acceleration through laser-plasma wakefield for future tabletop particle accelerators, the study of high-intensity laser interactions, new highly efficient lighting systems etc.

The brief introduction given above highlights the versatility and diversity of plasma applications. The focus of this chapter is the application of non-conventional high-energy-density pulsed plasma generated in dense plasma focus device for controlled synthesis and processing of a variety of materials.

2.2 Material Synthesis and Processing

Materials with different properties, shapes, and sizes are fundamental to different functional structures ranging from the smallest integrated circuit to the largest man-made structure. In almost every technology, the performance, reliability, or cost is determined by the materials used. As a result, there is always a relentless drive to develop new materials and processes (or to improve existing ones). Understanding the relationships among the structures, properties, processing, and performance of materials are crucial to optimize their functional performance and equally important is the continuous development of technologies that can provide new tools for materials processing and synthesis. The material processing and synthesis technologies help in the development of new novel materials with better properties. For example, the surface engineering of metal surface can help to protect it against all forms of wear. The surface engineering of metals can be achieved either through coatings (material syntheses/depositions) or through surface/material processing, as shown in Fig. 2.1. It may be noticed in Fig. 2.1 that two key material deposition or synthesis methods are chemical vapor deposition (CVD) [3] and physical vapor deposition (PVD) [4] methods. Since plating is mostly common to

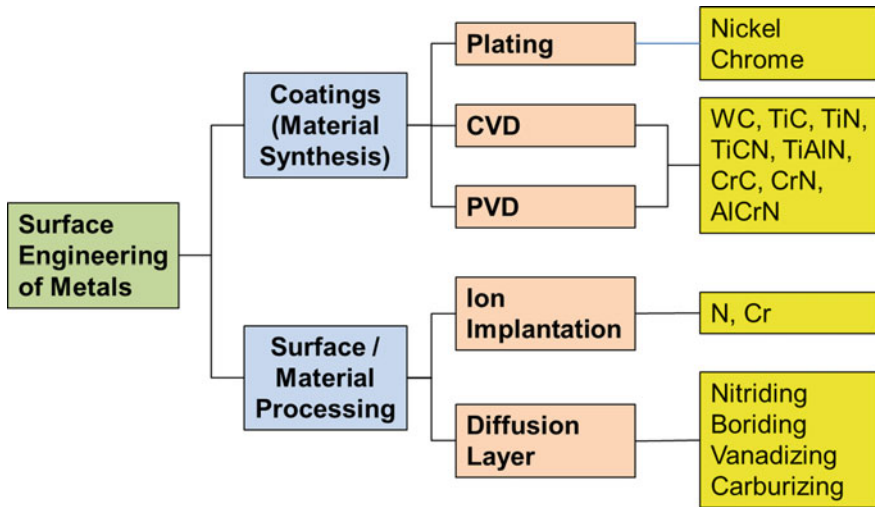


Fig. 2.1 Material synthesis/deposition and processing as tools for surface engineering of metals to protect them against different kinds of wear. Note CVD and PVD stand for chemical and physical vapor deposition methods

metals only, we will not discuss that. The typical setups of CVD and PVD systems are shown in Fig. 2.2.

Chemical Vapor Deposition (CVD): The CVD process involves the formation of a non-volatile solid thin film or nano-structured morphology on the substrate placed in heated reactor zone by the reaction of vapor phase chemicals (reactants) that contain the required constituents. As shown in Fig. 2.2a the cold gaseous or vapor precursor(s) of the reactant(s) are introduced into the heated reaction chamber that are decomposed and reacted at the heated substrate surface to form the thin film. The controlled transport of the reactants, controlled by mass flow controllers and evacuation pumping speed, is further forced by convection to the deposition region which is a heated substrate in heated reactor region. The reactants are decomposed by the heat or any other energy source such as plasma discharge or radiation energy and are transported by diffusion from the main gas/vapor stream to the substrate surface. At the substrate surface, many different processes take place which include (i) further chemical decomposition or reaction of the reactants, (ii) surface adsorption or nucleation at certain nucleation or attachment sites which are atomic-level ledges, kinks or grain boundaries, and (iii) surface migration and other surface reactions. Some of the byproducts get desorbed from the surface and transported back to the main gas stream by diffusion and are finally evacuated by the vacuum pump. The schematic of the process is shown in Fig. 2.2a. There exists a very large variety of CVD systems which are named either on the basis of method/type of precursor injection or on the basis of the method of precursor gas/vapor decomposition. The names of these CVD systems are self-explanatory such as Aerosol-Assisted CVD (AACVD) [5], Direct Liquid Injection CVD

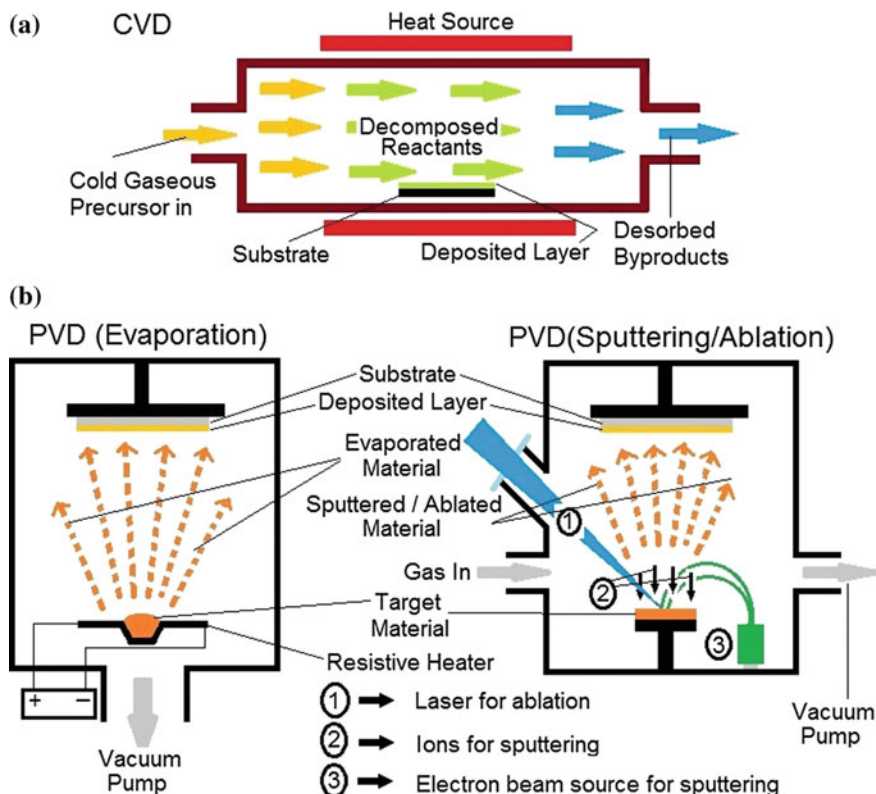


Fig. 2.2 Material synthesis/deposition methods. **a** Chemical vapor deposition (CVD), and **b** physical vapor deposition (PVD) methods

(DLICVD) [6], Plasma-Enhanced CVD (PECVD) [7], Hot Wire CVD (HWCVD) [6], Atomic Layer CVD (ALCVD) [8], Rapid Thermal CVD (RTCVD) [9], Combustion CVD (CCVD) [10], Hybrid Physical-Chemical VD (HPCVD) [11], etc. Among these, PECVD systems are becoming increasingly popular as the use of plasma discharge based decomposition of precursor gas is much more efficient compared to purely thermal decomposition in other CVD systems. This allows PECVD systems to operate at relatively less reactor zone temperature and in relatively shorter time scale, making them energy- and cost-efficient. The CVD-based thin films deposition systems have the advantages of the possibility of high growth rate synthesis, good reproducibility and ability to grow epitaxial thin films. The disadvantages of CVD include the typical use of high temperatures (though in PECVD the temperature can be lower), complex processes and toxic and corrosive gases.

Physical Vapor Deposition (PVD): The PVD is fundamentally a vaporization coating technique involving the transfer of material on an atomic level. The PVD process is quite similar to CVD except for the usage of the different physical form

of raw material. In PVD, the material that is being deposited starts out in solid form rather than in gaseous form. In addition to vaporization of solid raw material by heating normally using resistive heater (left configuration in Fig. 2.2b), other methods of vaporization such as sputtering of the solid target by plasma or ions and ablation by an intense laser pulse or energetic electron beam are also used in PVD as shown in configuration on the right in Fig. 2.2b. Various different types of PVD systems which use different evaporation methods are cathodic arc PVD [12], electron beam PVD, evaporative PVD, pulsed laser PVD, magnetron sputtering PVD, etc. [13]. The PVD is carried out under vacuum conditions with three key steps involved: evaporation, material transport, and deposition. The evaporation/sputtering/ablation stage of PVD involves either the direct resistive heating of solid material or the bombardment or irradiation of solid target by a high energy source such as a beam of electrons or ions, or plasma or concentrated laser light beam. During this stage, the atoms in neutral and ionized form are dislodged from the target surface. Evaporation is followed by transportation of vaporized material species from the target to the substrate surface. Finally, the impinging material is deposited in the form of coating at the substrate surface which may be heated or kept at room temperature. The thin films of various different materials such as metals, bi-metals, metal nitrides/oxides/carbides, etc. can be deposited using the PVD system with above-mentioned three processes using the corresponding targets in same exact stoichiometry. For example, the coating of Al or AlN can be deposited using targets of Al or AlN with inert gases being used as the background gas in the PVD chamber. The PVD system can also be used as hybrid physical-chemical vapor deposition system where an additional step of the chemical reaction is introduced by using reactive background medium. For example, to deposit AlN thin film on a substrate the Al solid target is vaporized by plasma or ions or electrons or laser and reactive background gas containing nitrogen, such as molecular N_2 or ammonia, is used to obtain nitrogen atoms. The atoms of Al metal will then react with nitrogen atoms during the transport stage from target to the substrate to form AlN coating on the substrate. If the heated substrate is used then the chemical reaction can also take place between the vaporized target material and decomposed reactive background gas at the substrate surface. The advantages of PVD are (i) ability to produce high-quality hard coatings with better corrosion and abrasion resistance, (ii) ability to utilize any type of inorganic and organic target material for deposition on an equally diverse group of substrates, and (iii) little damage to the target and the substrate. The disadvantages are (i) line of sight transfer and deposition in most PVD process making it difficult to coat undercuts and similar surface features, (ii) to require high vacuum conditions and high temperatures and hence resource requirements are stringent, and (iii) deposition rates of coatings are usually quite low.

Material Processing: In the context of this chapter, the material synthesis simply refers to creating new thin films or coatings on substrates using CVD or PVD processes, while the material processing refers to the modification of the preexisting material, either in bulk or thin film, by thermally activated diffusion, ion implantation or plasma exposure. As an example, the deposition of thin film of ZnO

on Si substrate using pulsed laser ablation of solid ZnO target is an example of material synthesis. The ZnO thin films synthesized in this fashion are mostly oxygen deficient and exhibit n-type behavior. The annealing of oxygen-deficient ZnO thin film in a furnace at a suitable temperature with partial oxygen flow can reduce the oxygen deficiency in ZnO due to oxygen diffusion. Alternatively, one can bombard oxygen-deficient ZnO with nitrogen ions to implant nitrogen in ZnO lattice to convert it to p-type material. Both, the thermal treatment in oxygen ambience and nitrogen ion implantation which modify the physical properties of ZnO, in this case, are the examples of material processing. The material processing, however, is not just limited to ion implantation or changing the chemical or stoichiometric composition of the thin film as mentioned in the example above but it is also referred to a much wider range of processes shown in Fig. 2.3. This includes (i) etching to make nano- or micro-structures by chemical or plasma-based processes particularly for device fabrication as is normally used in microelectronic industry, (ii) doping of suitable atoms by thermal diffusion or ion implantation or plasma treatments to change material properties, (iii) changing the crystal structure and surface facet of the material by various processing methods, (iv) surface functionalization of material to make it behave differently for different applications,

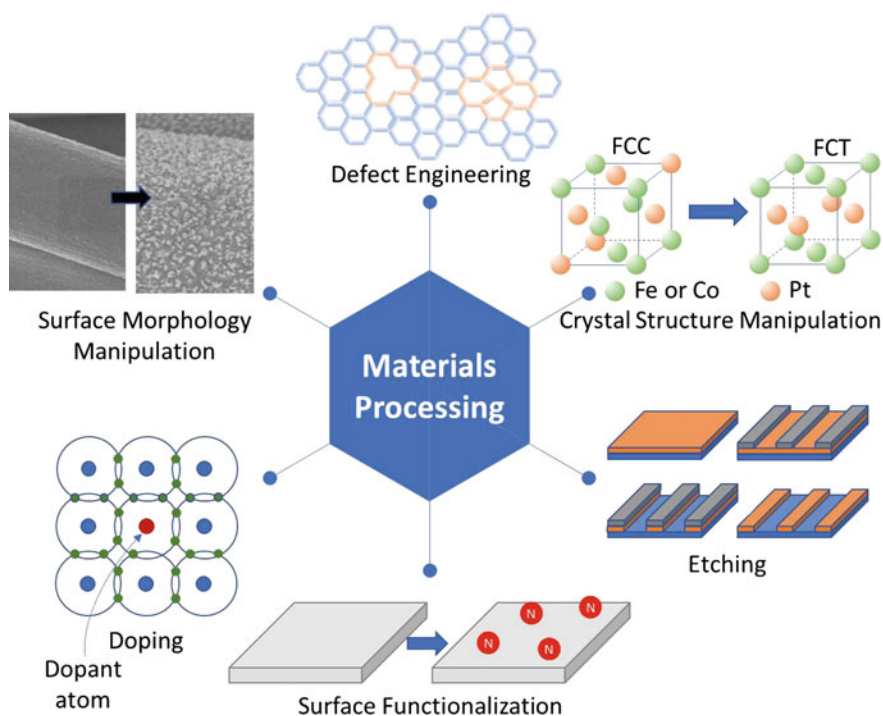


Fig. 2.3 Various types of material processing which changes the material characteristics and materials functional behavior

(v) surface morphological manipulation to increase the surface for the materials which is beneficial for many applications, (vi) defect engineering of materials, etc.

2.3 Plasmas for Material Synthesis and Processing

Plasma, the ionized gas, can be formed when an external energy source is introduced to the matter in gaseous, liquid, or solid form. External energy sources include heat, concentrated light such as in a laser, electric, and electromagnetic field. The solid, liquid, and gas can be either converted directly into plasma state or may go through other intermediate states before being converted into plasma when the energy is provided as shown in Fig. 2.4. For example, the solid can directly be ablated in a plasma state by focused laser light or electron/ion beams or the solid may first change into the liquid state followed by vaporization of the liquid to gas phase and finally the decomposition of a significant fraction of atoms into electrons and positive ions. The energy sources can be used in a controlled way to achieve plasma conditions with specific outcomes. If the energy received by atoms or molecules of the matter is sufficient enough to release the outermost electron(s) and create a significant number of ions and electrons then “plasma” is said to be formed. The temperature required to form plasmas from substances in thermal equilibrium range from 4000 K for easy-to-ionize elements like cesium to 20,000 K for hard-to-ionize elements like helium. In addition to ions and electrons, the plasma contains neutrals, excited neutrals, excited ions, and photons.

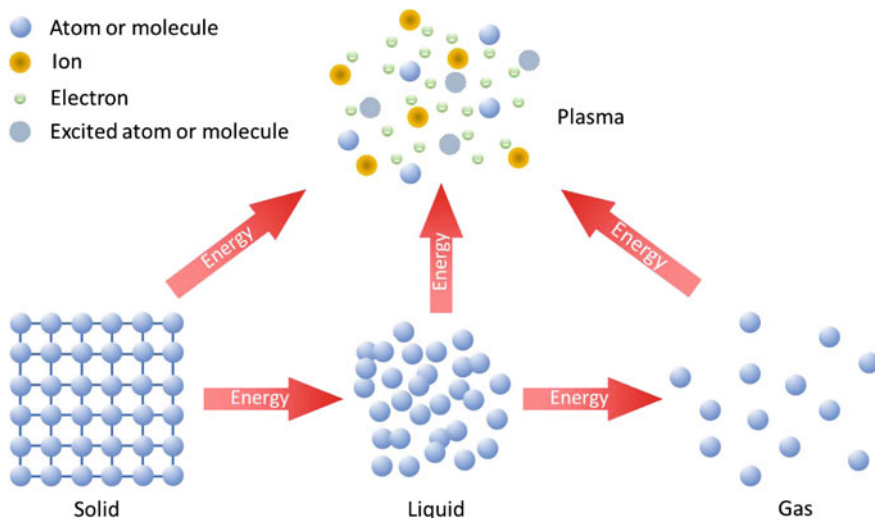


Fig. 2.4 Plasma formation from solid, liquid and gases upon delivery of energy

The easiest way to generate plasma is by applying the electric field across the gas. Normally, gases are electrical insulators but there is a negligibly small fraction of gas that is ionized due to bombardment by energetic cosmic radiations. The charges, specifically light electrons, can be accelerated by the applied electric field, which then collide with neutral particles producing an avalanche of electrons and ions breaking down the neutral gas into plasma. The electric field needed for gas breakdown can be setup simply using a pair of electrodes, or with an “electrodeless” radio frequency induction coil, or with a laser, or with charged or neutral particle beam. Heating of solids, usually alkali metals, in the evacuated chamber can not only evaporate them but also ionize them to form plasmas. Similarly, many chemical processes can also cause ionization forming plasmas. The ionization fraction of a plasma is given by $f_{iz} = n_i / (n_i + n_g)$, where n_i and n_g are ion and neutral gas density respectively. The f_{iz} is near unity for fully ionized plasmas and is $\ll 1$ for weakly ionized plasmas.

More precisely, plasma is a quasineutral gas which exhibits collective behavior [14]. The quasineutrality simply means that plasma is neutral enough so that one can take the number of densities of ions, electrons, and neutrals almost equal to each other but not so neutral that all interesting electromagnetic forces vanish. The collective behavior means that the motion of plasma species depends not only on local conditions, such as collisions among the species but also on the state of plasma in the remote region. The plasmas can occur naturally or are man-made. They exist over a very wide range of temperature and density, as shown in Fig. 2.5.

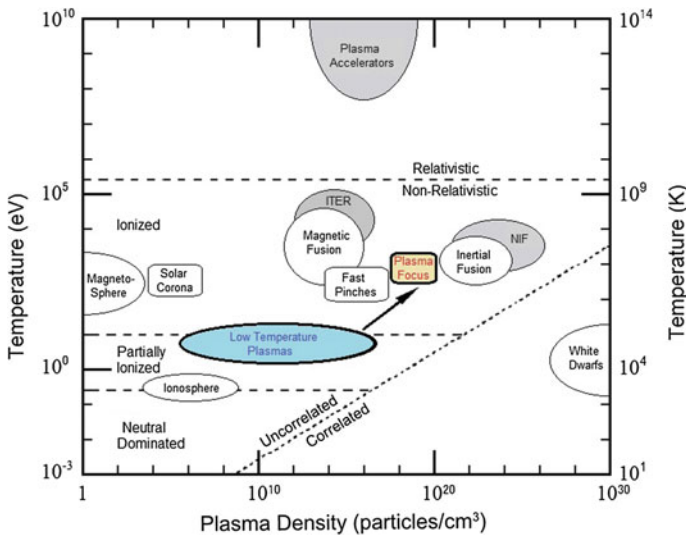


Fig. 2.5 Natural and man-made plasmas existing over a very wide range of temperature and density. Note the difference in temperature and density of low-temperature plasmas, conventionally used for material synthesis and processing, and the plasmas of dense plasma focus (DPF) devices used and discussed in this chapter

The **density**, **temperature**, and **composition** of plasma are its key parameters. The **density**, number of particular species per unit volume, is described by the electron density n_e , the ion density n_i , and the neutral or the gas density n_g . For multiple ion species in complex plasma one may describe the ion and neutral/gas density of species x as n_{ix} , and n_{gx} . Additionally, many plasmas contain positive (after neutrals loose an electron) and negative (after an electron is attached to neutral particle) ions. The density is usually a function of time, position, applied field/power, etc. Another important quantity that is needed to characterize a plasma, as evident in Fig. 2.5, is the **temperature** of the individual component of the plasma; and can be designated as the electron temperature T_e , the ion temperature T_{ix} of species x , and the neutral/gas temperature T_{gx} of species x . The multiple temperatures for different components of plasma can exist in a situation where plasma components are not able to equilibrate with each other. Like density, the plasma temperature is also not usually constant in space or time. The **composition** of plasma is one of the most important parameter, particularly for material synthesis. Knowing composition, particularly the mass numbers of all ions and neutral species as the function of space, time and feeding gas stock is handy for better control over the material synthesis and processing. Based on these three key parameters the plasmas can be classified in many different categories. However, for the sake easy classification we will simply classify the plasmas into two broad categories from the point of view of their applications for material synthesis and processing: (i) the low and (ii) the high-temperature plasmas. The dense plasma focus (DPF) device, which is the focus of this chapter, falls into the category of high-temperature plasma which also has high density (refer Fig. 2.5) while most of the plasmas commonly used for material synthesis and processing are low-temperature plasmas with density varying over a very wide range but still at least about two to three orders of magnitude lower than DPF pinch plasmas.

2.3.1 *Low-Temperature Plasmas (LTPs) for Material Synthesis and Processing*

The low-temperature plasmas (LTPs) are characterized by low electron kinetic temperatures ranging from fractions to tens of eV with low ionization fraction. A large fraction of the gas in LTPs actually remains in the neutral state. The LTPs are mainly produced by low-current AC or DC electric gas discharge or by gas discharges initiated by RF or microwave electromagnetic fields or by concentrating intense laser/ion/electron beams on the solid targets etc. The low-temperature plasmas are the backbone of material synthesis and processing industry. The LTPs are grouped in the blue box in Fig. 2.5. Low-temperature plasmas can be further classified into non-equilibrium and equilibrium (thermal) plasmas. The equilibrium (thermal) plasmas are formed in high-pressure gas discharges where due to higher densities and sufficiently long durations of plasma existence, the electron and ions

and neutrals have frequent and sufficient collisions among them resulting in equilibration of temperatures among the charged and neutral species, i.e., $T_e \sim T_i \sim T_g$; where T_e , T_i , and T_g are temperatures of electrons, ions, and background gas (neutrals) species, respectively, and represent their mean kinetic energies. The non-equilibrium plasmas, on the other hand, are formed when (i) either the low operating pressures with lower electrons/ions/neutrals densities result in insufficient collisions between electrons and ions and neutrals disallowing the thermal equilibrium to be achieved; or (ii) even for high operating pressure plasmas which have higher collision rates among different species but the plasmas are short-lived (e.g., in pulsed electric discharge) interrupting the equilibration process as the plasma existence duration is less than temperature equilibration time. They are described by relation $T_e \gg T_i = T_g$.

The low temperature, equilibrium and non-equilibrium type, cold plasmas have been used extensively in synthesis and processing of materials due to their interesting combination of electrical, thermal, and chemical properties making them indispensable and versatile tool in many industries. In plasma, the neutral species or radicals are unpaired electron gas particles that are chemically reactive and electrically neutral. The result of ionization of a gaseous species leads to a plethora of active species and is the basis for plasma chemistry. This mixture of reactive gas species offers enhanced reactions and creates new chemical pathways not found in room temperature chemistry. The ease of forming a plasma discharge is an added incentive since active species can commence and be sustained at a wide range of electron temperature values ranging from 1 eV to several tens to hundreds of eV while maintaining vacuum at a wide range of pressure values. Various gas mixtures and plasma intensity deepen the processing technique further allowing a wide array of conditions or chemical pathways to be made available. In addition, the presence of highly concentrated energetic and chemically active species leads to higher processing efficiencies at low bulk plasma temperature. Thus, processes exceeding thermodynamic equilibrium can exist which intensifies traditional chemical processes [15].

The wide range of density, temperature, and composition of LTPs has largely contributed to the long and expanding list of applications for material synthesis and processing as a result of both scientific and economic drivers. The temperature, energy, and density range of the neutral and/or ionized species allow heat and particle control to sputter, etch, clean, melt, cut, functionalize, coat, and grow materials at macro-, micro- and nanoscale via the so-called “plasma processing and synthesis”. This allows thousands of applications of LTPs in different industries

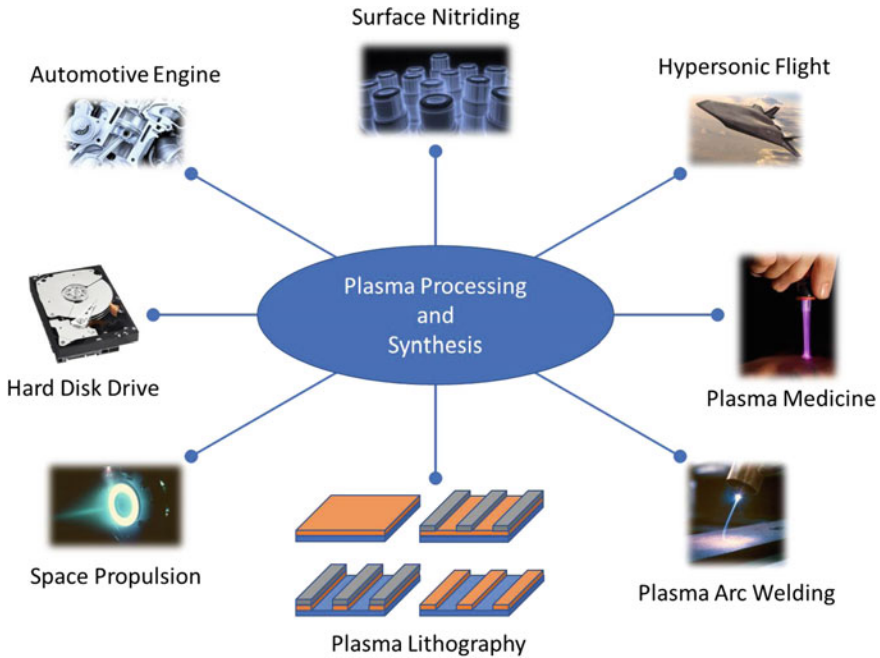


Fig. 2.6 Plasma material processing and synthesis in the industry

[16], refer Fig. 2.6. Some of the most prominent industrial applications are listed below.

- Plasma etching in fabrication of microelectronic chips;
- Plasma light sources such as discharge lamps, low-pressure lamps, field emitter arrays, lasers and plasma displays;
- Plasma deposition of (i) silicon nitride for surface passivation and insulation, (ii) amorphous silicon films for solar cells, (iii) diamond thin films, (iv) ceramic or metal alloy coatings used for protection against wear or corrosion in aircraft and automotive engines, (v) high-temperature superconductors and refractory materials, (vi) biocompatible coatings for body implants, (vii) magnetic films and carbon overcoats for hard disk drive for data storage etc.;
- Surface oxidation used in fabrication of silicon-based microelectronic circuits;
- Plasma switches such as electric power switches, pulsed power, etc.;
- Plasma nitriding, which is used to harden the surface of steel;
- Plasma melting and refining of alloys;
- Plasma-assisted manufacture of optical fibers used in communications;
- Plasma welding and cutting;
- Plasma volume processing such as flue gas flue gas treatment, metal recovery, waste treatment, water purification, etc.;
- Plasma sterilization in medical industry;

- Plasma thruster for space propulsion;
- etc.

It would not be wrong to say that low-temperature plasma-based processing and synthesis technologies are ruling the industrial applications of plasmas. Science and technology of low-temperature plasmas are quite well understood and developed, though there is still an enormous scope and potential to master it further particularly for manipulation and synthesis of materials at the nanoscale. However, since the focus of this chapter is hot and dense high-energy-density plasma in dense plasma focus device, we will next introduce the high-temperature plasmas.

2.3.2 High-Temperature Plasmas for Material Synthesis and Processing

High-temperature plasmas are synonymous with fusion plasmas. They have temperatures ranging from few hundred eV to several keV making the plasma to be in the almost fully ionized state. As can be seen from Fig. 2.5, these plasmas are obtained in magnetic and inertial fusion devices as well as in high-current powerful pinch discharge devices. They not only have high temperatures but also have high densities. Historically, these high-temperature fusion plasmas were not used for any practical application in material synthesis and processing. The thermonuclear fusion facilities such as ITER and NIF, in near future, will be performing D-T fusion experiments to demonstrate ignition and energy gain. These experiments will result in enormous plasma, radiation, and heat load on reactor chamber wall. One of the key issues still to be resolved in the quest for fusion energy production is the characterization, qualification (testing), and development of advanced plasma facing materials capable of withstanding the extreme radiation and heat loads expected in fusion reactors. Fundamental understanding of plasma-material surface interaction (PSI) processes in magnetic and inertial confinement fusion devices is one of the key areas of research in fusion material science and engineering. There are many gaps in the knowledge related to the PSI area which must be addressed in order to build up a validated predictive capability in support of the design of plasma facing components for ITER and a fusion demonstration power plant (DEMO). While a number of unresolved issues in plasma edge physics in magnetic confinement devices (e.g., scrape-off layer plasma widths, flows and turbulent transport) can only be addressed using tokamaks and stellarators, issues related to the impact of transient heat loads on materials, erosion, and re-deposition mechanisms, fuel retention, dust formation, as well as new material concepts can be explored using dedicated testbed devices such as plasma focus, plasma guns, plasma and particle accelerators, etc.

The focus of this chapter is however not about the fusion plasmas or the similar testbed facilities to investigate the plasma-material interaction processes on candidate materials for fusion reactor wall chamber but on relatively less-explored area of application of high-temperature high-energy-density dense plasma focus (DPF) device for material processing and synthesis. The dense plasma focus device,

in Fig. 2.5, is seen to have plasma temperature similar to that magnetic and inertial fusion plasmas but the density is in between the two of them. The high-energy-density plasmas, by definition, refers to the plasmas which are heated and compressed to extreme energy densities, exceeding 10^{11} J/m^3 (the energy density of a hydrogen molecule) [17]. The magnitude of physical parameters associated with high-energy-density physics is enormous: shock waves at hundreds of km/s (approaching a million km per hour), temperatures of millions of degrees, and pressures that exceeds 100 million atmospheres. The plasmas with energy densities in the range of $(1\text{--}10) \times 10^{10} \text{ J/m}^3$ are also now classified as high-energy-density plasmas. There are many facilities which fall in the category and they include high-energy long-pulsed (nanosecond range) lasers and high-power very short pulse (femtosecond range) TW or PW laser-based laser-plasma systems [2, 18], and fast high-current pulsed power Z-pinch [19]. The energy density of DPF devices, estimated by dividing the energy stored in the DPF capacitor bank by the volume of the final pinch column, is reported to be in the range of $(1.2\text{--}9.5) \times 10^{10} \text{ J/m}^3$ making it a high-energy-density plasma facility [20].

In addition to DPF devices, the other two high-temperature high-energy-density devices that have been extensively used for material synthesis and processing include plasma accelerator (such as QSPA Kh-50 in Kharkov, Ukraine) and PHEDP plasma gun in Ukraine and China, respectively. The QSPA Kh-50 (Quasi-Stationary Plasma Accelerator, Kh-50) [22, 23] consists of two stages, refer Fig. 2.7 [21]. The first one is used for plasma production and pre-acceleration. The second stage (main accelerating channel) is a coaxial system of shaped active electrodes-transformers with magnetically screened elements. The total energy stored in capacitor bank is about 2.2 MJ at the charging voltage of 25 kV. The amplitude and time duration of discharge current is up to 700 kA and 300 ms, respectively. The main characteristics of plasma streams depending on operations regime and distance from accelerator output can be varied in a wide range: density of plasma $10^{15} - 8 \times 10^{16} \text{ cm}^{-3}$, velocity up to $4.2 \times 10^7 \text{ cm/s}$, energy density of

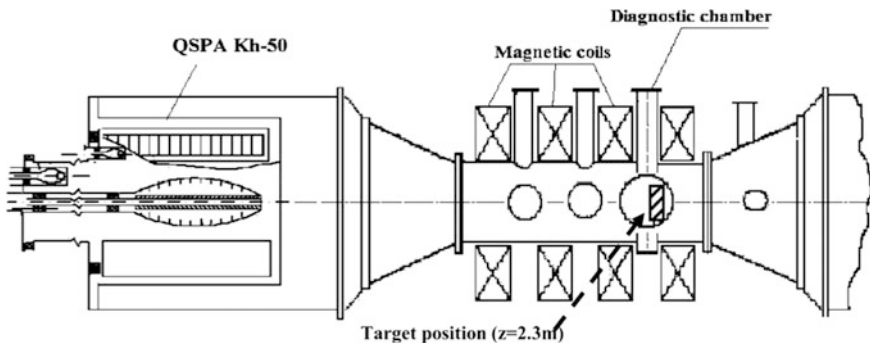


Fig. 2.7 Schematic of quasi-stationary plasma accelerator (QSPA Kh-50) which has been extensively used for material research for plasma facing components of fusion reactors. Reprinted from Garkusha et al. [21], Copyright (2009), with permission from Elsevier Ltd

plasma stream 5 J/cm^2 – 2 kJ/cm^2 , and total energy in plasma stream up to 600 kJ. The high-energy-density plasma stream generated by QSPA can be injected into the vacuum chamber of 10 m in length and 1.5 m in diameter. Average plasma stream diameter is about 0.5 m at the distance of 1 m and it is up to 1 m at the distance $>3 \text{ m}$ from accelerator output. This enormous device, therefore, has the capability to test full-scale prototypes of tokamak divertor cassette. Most of the studies done on QSPA are limited to processing of fusion relevant material at high-temperature and high-energy-density which is not the focus of this chapter and hence is not discussed in detail.

Another high-temperature plasma device which has been used occasionally by the group led by Prof Si-Ze Yang at Beijing National Laboratory for Condense Matter Physics, Chinese Academy of Sciences is a plasma gun which has been referred in their reported work as Pulsed High-Energy-Density Plasma (PHEDP) facility [24–32]. This device has been used for film deposition and surface modification. The typical setup of PHEDP is shown in Fig. 2.8 [30]. As shown in Fig. 2.8, it consists of three sections: (i) the fast pulse electromagnetic valve driven by the discharge of a stored capacitance C_p (2 kV, 180 mF) through a driving coil to introduce the working gas into the vacuum chamber; (ii) the coaxial PHEDP gun which is powered by a capacitor bank C_g (5 kV, 1.11 mF) connected between the outer and inner electrodes; and (iii) the vacuum chamber, where films are deposited. Other parameters like the distance between substrate and gun, the number of pulses and base pressure, etc., all influence the properties of the film. Other most important features of PHEDP [33] are high electron temperature (about 10–100 eV), high plasma density (about 10^{14} – 10^{16} cm^{-3}), very high axial velocity (about 10–50 km s^{-1}), and the energy density of 1–10 J cm^{-2} . Yang and his coworkers have used the PHEDP facility for a variety of applications which include deposition of (Ti,Ta)N [25] and Ta(c)N [26] thin films, titanium carbonitride [27, 29] and titanium nitride [30] films on cemented carbide cutting tools, surface metallization of alumina ceramics [31], titanium coatings on Si_3N_4 [32], etc.

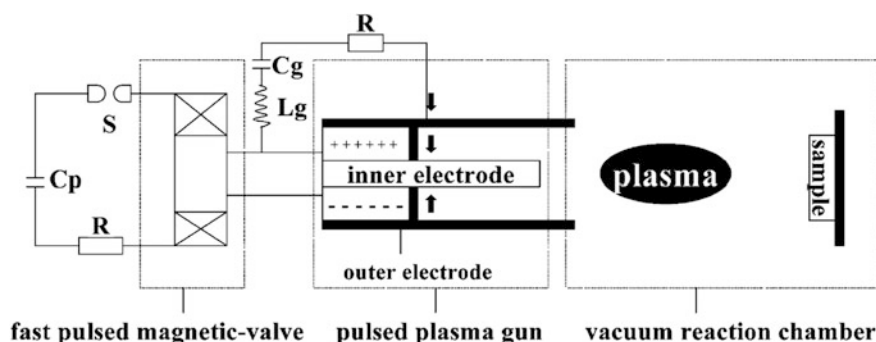


Fig. 2.8 Schematic of PHEDP facility at Chinese Academy of Sciences used for thin film deposition and surface modification. Reprinted from [30], Copyright (2003), with permission from Elsevier Ltd

The PHEDP facility, used by Yang and his coworkers, is quite similar to DPF device except that it does not have compression/pinch phase and hence the plasma is relatively not as hot and dense as one can obtain in DPF device due to efficient pinch. This book has several chapters that deal with various aspects of DPF devices ranging from simulation and modeling of DPF devices, X-ray, and neutron emissions studies from DPF devices and application of DPF devices for hard coatings. In this chapter, we will discuss the application for DPF device for material processing and synthesis under Sect. 2.5. The next section is devoted to the detailed introduction to DPF devices providing device details, the principle of operation and its key characteristics.

2.4 Dense Plasma Focus (DPF) Device: Introduction, Principle, and Characteristics

The dense plasma focus (DPF) device, refer Fig. 2.9, is a coaxial electrode gun in which plasma discharge is initiated at the closed end of the electrode assembly as the electrical energy stored in a high-voltage fast discharging capacitor bank is transferred across the electrodes. The discharge soon evolves into an axially accelerated plasma sheath which finally compresses into a hot and dense pinch plasma column at the top of the central electrode (anode). The coaxial gun primarily consists of a central conducting electrode typically a metal rod surrounded by a solid cage or an array of conducting electrodes in a squirrel cage configuration. Typically, the central electrode acts as the anode and the outer electrode (connected to chamber wall) acts as the ground electrode. One end of the coaxial electrode

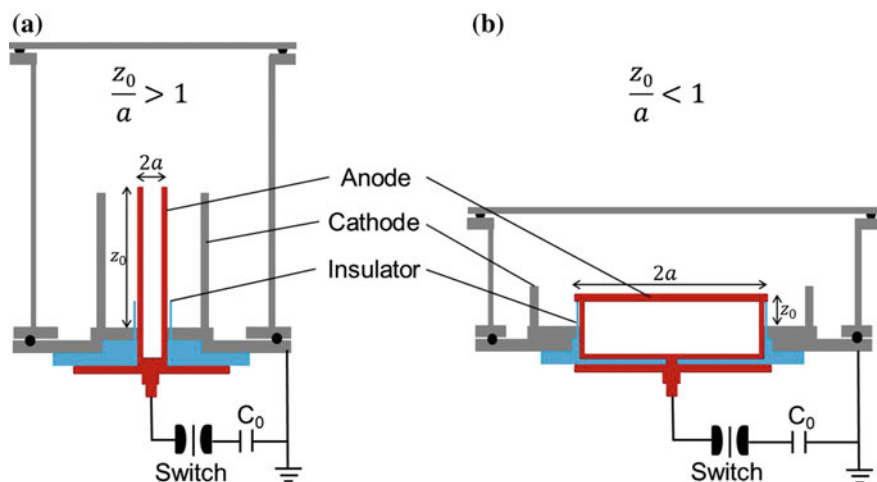


Fig. 2.9 Schematic of dense plasma focus (DPF) device. **a** Mather-type and **b** Filipov-type configuration

assembly is open, whereas the other end where the discharge is initiated is closed. The volume of DPF chamber where the coaxial electrode assembly is placed is comprised of desired operating gas at a suitable pressure. This configuration is one of the simplest and efficient methods in producing pinch plasma capable of providing avenues to conduct fusion relevant research in a relatively small and simple device [34, 35].

In the 60s, the design of this device was derived from a predecessor with similar purpose called a z-pinch device which generated a column of plasma that self-compresses when a high current flows through the plasma resulting in a high-temperature and dense plasma at the axis of the electrode. Two different electrode assembly geometries of DPF devices were developed independently with different anode aspect ratio (anode length upon its diameter). The Mather-type [36] DPF devices, developed by J.W. Mather, are the one with an anode aspect ratio typically in a range from 5 to 10 (i.e., anode aspect ratio >1) and the Filipov-type [37] devices, developed by N.V. Filipov, have the anode aspect ratio <1 . In Filipov-type DPF devices the anode radius is much larger compared to its axial dimension and hence the plasma current sheath is accelerated in the radial direction towards the axis of the anode whereas in Mather geometry the sheath is accelerated mostly along the axial direction. The two geometries are shown in Fig. 2.9.

2.4.1 DPF Device Details

The coaxial electrode assembly of a DPF device resides inside a vacuum chamber and the whole system is operated at the pressure of about 10 mbar and less or at optimal pressure ranges which satisfy the focusing or pinching of the plasma sheath at the final stage. The vacuum condition allows for reliable sheath formation in the initial stage as the minimum breakdown voltage depends on the pressure according to the Paschen's law. Another important factor in the reliable operation of the DPF device is the insulator sleeve placed around the base of the anode and the presence of which allows proper formation of the plasma sheath in the initial breakdown phase and leads to efficient pinching [38]. To operate the plasma focus, high-voltage (typically greater than ten kV) and high-current (>10 kA) electrical pulses of few hundred ns to few μ s duration are required. The most economic and simple way to generate these pulses is to charge a capacitor to a suitable voltage and discharge it through load viz. the plasma focus. However, to get high current pulses, the capacitors, and the connections from the capacitors to the load are specially designed. The typical working gases used in most DPF devices are hydrogen, deuterium, inert gases, and reactive gases such as oxygen, nitrogen, methane, acetylene, etc. Most studies that require the production of radiation (X-rays or neutrons) sources using the DPF device will utilize inert or deuterium gas while there is no restriction on gases used for material synthesis or treatment unless a specific material outcome is required. Gases used in material synthesis involving reactive gases such as oxygen and nitrogen will yield ceramic materials such as zinc

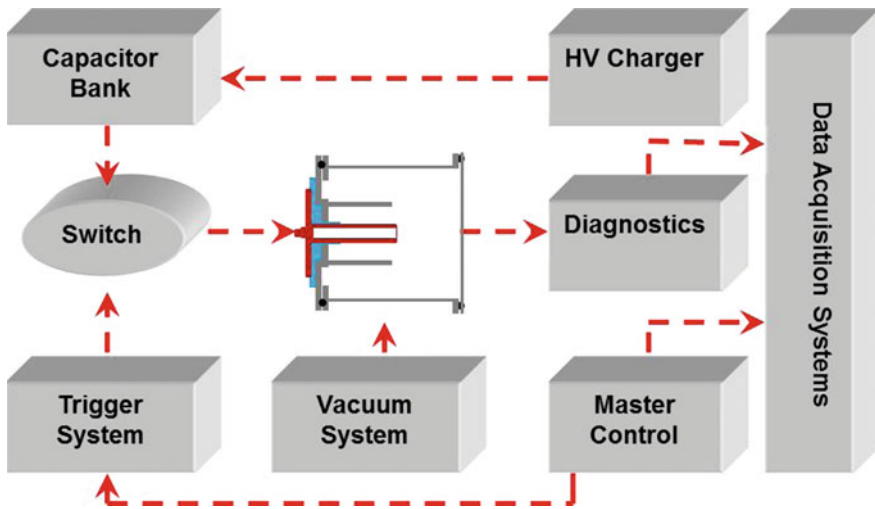


Fig. 2.10 Block diagram representation of the DPF device

oxide, titanium nitride, etc. The inert gases, such as neon, argon, etc. will yield deposited material derived from the anode tip material. The overall layout of DPF device with its various subsystems is shown in block diagram in Fig. 2.10.

Capacitor Bank: A single capacitor or a bank of capacitors, based on desired energy storage capacity, is used to store the electrical energy needed for the operation of the DPF device. The capacitors used for DPF devices are high-energy-density fast-discharging capacitors which are capable of delivering high currents needed for efficient acceleration and compression of the current sheath. The capacitor bank value, for the DPF devices available in author's Plasma Radiation Sources Lab, NTU, Singapore, is decided based on the typical operating voltage range of 12–15 kV for ease of transmission line designing. We use commercially available energy storage class of capacitors which are rated typically up to 30 kV with shot life of $>10^5$ charge/discharge cycles withstanding 80% voltage reversal. By operating the capacitors at 40–50% of their maximum charging voltage, life expectancy improves significantly and can be used for $>10^6$ charge/discharge cycles. The selection of capacitors for DPF device also depends on the intended repetition rate of the device. The single 30 μF /15 kV capacitor used in UNU-ICTP DPF device is not designed for repetitive operation, therefore for 10 Hz FMPF-3 device we used a total of eight low inductance 0.3 μF /30 kV plastic case capacitors (Model No. #37323), procured from General Atomics, USA. These capacitors specifically feature repetitive mode of operation.

Triggerable High Current Switch: A triggerable high-current switch(es) in a capacitor bank is/are incorporated to transfer energy from the bank to the load (electrode assembly in DPF chamber) at a preset voltage and time. For a fast discharge in low inductance system, the switch should have (i) low inductance, (ii) low erosion at high current levels, (iii) minimum breakdown time delay (also

referred as jitter), and (iv) reliable operation. The simplest and the most economical switch is the sparkgap switch. The sparkgaps are available in various configurations such as trigatron, direct over-volted gaps, field distortion gaps, railgaps, etc.; though some configuration like railgaps can be quite expensive. The DPF devices operated in author's lab use swinging cascade spark gap switch [34] for UNU-ICTP DPF devices while other devices such as NX2 [39], NX3 [40], and FMPF-series [41] DPF devices use pseudo-sparkgap switches.

Trigger System: Switches used in DPF devices need to endure high-voltage and high-current operation along with precise timing but its switching performance is mainly decided by applied trigger pulse characteristics produced by the trigger system/module. A major factor that affects the performance of the switch is trigger pulse rise time applied to the switch. The simple swinging cascade spark gap switches used in UNU-ICTP DPF device uses relative simple low-voltage and high-voltage silicon-controlled rectifier circuits generating a negative pulse of about 600 V which is amplified by commercially available HV TV transformer by about 60–70 times to about 35–42 kV [34]. The trigger system used for pseudospark switches [42] are slightly more complex but can be easily assembled and used for reliable switching of capacitor bank energy to the DPF tube.

The DPF Chamber: The capacitor bank, high-current low jitter switch(es), and a trigger system form the pulse power driver while the DPF chamber with coaxial electrode assembly is the load where the plasma is formed and compressed to high temperature and density. The DPF chamber normally is fabricated from stainless steel of wall thickness of 3–5 mm with several vacuum parts, gas inlets, and diagnostics ports. The electrode assembly comprises of an anode as central electrode surrounded by cathode which can either be the chamber wall [43] or several rods in squirrel cage fashion mounted on backwall plate [44, 45], shown in Fig. 2.11. The anode and cathode, at the closed end, are separated by an insulator sleeve. Low erosion characteristic is one of the most important factors in the selection of anode material. In conventional DPF device experiments selection of anode material is based on low spark erosion characteristics, good mechanical and thermal properties, availability and low cost. Spark erosion rates of various materials that are used as anode have been shown in Table 2.1. The erosion results are presented in terms of the volume of eroded material per coulomb of charge transferred ($\mu \text{ cm}^3 \text{ C}^{-1}$) [46]. The “Elkonite”, the Cu–W alloy, has the lowest erosion rate but it is very costly and not easy to machine. “Aluminum” is the cheapest option but it has the highest erosion rate of all the materials along with poor mechanical strength. So many DPF devices normally use stainless steel, because of its relatively lower cost, good mechanical, and thermal properties though copper is also another good choice which has been routinely used in our UNU-ICTP and NX2 DPF devices. Similarly, the selection of insulator sleeve material is primarily done on the basis of the dielectric constant of the material as a study done by Beg et al. [47] indicated a significant enhancement in neutron yield with use of high dielectric constant sleeve material. Dielectric constants of various sleeve materials have been compared in Table 2.2. Although ceramic has highest

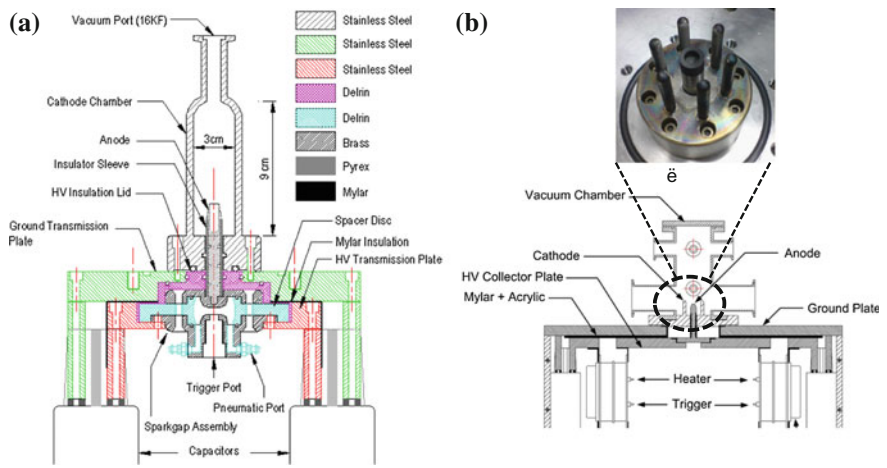


Fig. 2.11 Schematics of **a** FMPF-1 device with chamber wall as cathode, and **b** FMPF-3 device with cathode rods in squirrel cage fashion. Reprinted from **a** Verma et al. [43], Copyright (2008), with permission from IOP Publishing; **b** Reprinted from Verma et al. [44], Copyright (2010), with permission from Elsevier Ltd and Verma et al. [45], Copyright (2013), with permission from Springer

Table 2.1 Spark erosion rate of various anode materials

Material	Erosion rate ($\mu\text{m}^3 \text{C}^{-1}$)
Elkonite (Cu–W)	5.44
Brass	7.59
Stainless steel (SS)	9.14
Aluminum	17.37

Table 2.2 Dielectric constants and densities of various insulator sleeve materials

Material	Dielectric constant	Density (g cm^{-3})
Alumina/ceramic	4.5–8.4	4.14
Pyrex	4.5–6.0	2.05
Nylon	3.55	1.09
Perspex	2.76–3.12	1.08
Teflon	2.04	2.04
Quartz	3.7–4.1	2.17

dielectric constant, but as a compromise between electric characteristics, easy availability and low cost; in all our DPF devices, “Pyrex” has been used.

The choice of anode material and anode type (solid v/s hollow anode) for application of DPF devices for material processing and synthesis are very critical. For applications in material processing where the intended target material, placed down the anode stream, is required to be processed by high-energy ions of filling gas species or hot dense decaying plasma, the hollow anode with thin wall and

made up of material which erodes less is highly desirable. Otherwise, in addition to processing of bulk material, the undesirable deposition of impurity material from the ablation of anode material will also take place. The application requiring the use of DPF device as deposition facility may need to use the solid anode of suitable material with suitable background gas.

High Voltage Charger: A high-voltage power supply with suitable voltage and current rating is required to charge the capacitor bank. The electrical characteristics of the high-voltage power supply will depend on the repetition rate of DPF device. For single shot operations, with the significantly large time interval between the shots, a simple home-made power supply utilizing a step-up transformer with diode chain for rectification would suffice. This was the kind of HV charger that was assembled and given to the trainees participating in UNU-ITCP training program mentioned in Chap. 1. They worked pretty well for all kind of DPF operation. The repetitive operation of DPF devices, however, requires HV chargers with much large charge transfer rate to achieve fast charging of the capacitors. The repetitive NX2 and FMPF-series DPF devices in our lab use constant power charger “EMI HVPS 802L” (procured from M/s a.l.e. Systems, USA) for fast charging of the modular capacitor bank. The HVPS 802 is especially designed for fast charging of energy storage capacitors used in various pulsed power applications, with an average power exceeding 8000 W. The HVPS 802 power supply incorporates a high-frequency IGBT series-resonant inverter for efficient generation of the output power. A high-performance control module precisely regulates the output voltage, automatically compensating for line, load, temperature, repetition rate, and program voltage variations along with inbuilt overload and short-circuit protection. The output voltage of the HVPS 802 is fully adjustable over the whole range 1–40 kV.

Vacuum System: The typical pressure range in which DPF devices operate with best focusing efficiency is from about 1–10 mbar with heavier gases requiring lower pressure and lighter gases requiring higher operating pressures. The pressure range can also be manipulated with a change in anode dimensions and designs, e.g., longer anode will require smaller filling gas pressures while the tapered anode with reducing radius at the top can operate at higher filling gas pressures. Since the operating pressure is of the order of few mbar, typically a rotary vane pump capable of producing a base pressure of about 10^{-2} mbar is good enough for most operations. However, for application of DPF device in materials-related work it is advisable to use turbo molecular or any other high capacity pump which can produce a much lower base pressure of about 10^{-5} – 10^{-6} mbar to reduce the gaseous impurities in the chamber. Adequate vacuum gauges should be used to reliably read the filling gas pressure of the chamber. It is important to note that the DPF devices generate strong EM noise and shock waves during their operation, so for the safety of electronic pressure gauges (i) mechanical isolation using valves, and (ii) electronic isolation by switching off the gauge and detaching its cable to gauge controller are important safety procedures.

Diagnostic System: The DPF device is a rich source of many fundamental plasma phenomena and radiations. The fundamental plasma phenomena of interest include breakdown across electrodes at the closed end of the electrode assembly;

formation of plasma sheath; lift-off, axial acceleration and radial compression of plasma sheath; shock formation; plasma instabilities and turbulences; ionization wavefront formations; magnetic field structures; plasma decays, etc. The radiation of interest include soft and hard X-rays, relativistic electrons, instability-accelerated high-energy ions, and neutrons (for deuterium operated DPF). The availability of a large range of fundamental plasma physics phenomena and radiation yields which can be used for applications allows DPF to be a test-bed facility for many diagnostics making it an outstanding playground for fundamental research. Over the years a large number of electrical, magnetic, optical, spectroscopic, radiation, charge particles, and neutron diagnostics have been developed, tested, and explored on DPF device. For the material synthesis and processing application of DPF device, most of these diagnostics are actually not required but they create the knowledge and database and understanding of the device operation and characteristic features which help its operator to master its material-related application. Even though most diagnostics are not required for materials-related application of DPF device, basic electrical diagnostics comprising of a Rogowski coil and a resistive divider voltage probes to monitor the pinching efficiency and a Faraday cup (biased ion collector) to deduce the ion emission characteristics of the DPF device are normally employed.

Data Acquisition System: Most DPF devices operate with capacitor banks that produce electrical discharges with a quarter period ($T/4$) in the range of 500 ns to 4 μ s. Hence, a fast data acquisition system is required to record the signals from applied diagnostics. The digital storage oscilloscopes have sampling speed of about 1GS/s and bandwidth of 1 GHz with multiple channels (four channels) is more than sufficient for most works. The synchronization of signals is very important because the data processing requires comparison on the same time base.

2.4.2 Principle of Operation: Plasma Dynamics in DPF Device

The DPF chamber is first evacuated to base pressure using rotary vane pump or with the combination of turbo molecular and rotary vane pump. The working gas is then filled in right operating pressure range which is different for different gases (typically about few mbar). The capacitor bank is first charged to high voltages (typically in 10–30 kV range) using a high-voltage power supply. The electrical energy stored in the capacitor bank is then transferred to the electrode assembly by activating low-inductance high-current fast switches resulting in gas breakdown in DPF device chamber which undergoes through several phases shown in Fig. 2.12. If the operating pressure is within right working range then gas breakdown, phase ① in Fig. 2.12, is initiated across the insulator sleeve at the closed end of the electrode assembly. In the breakdown phase, the ionization of the background gas grows exponentially as predicted by the Townsend law which states that an electron

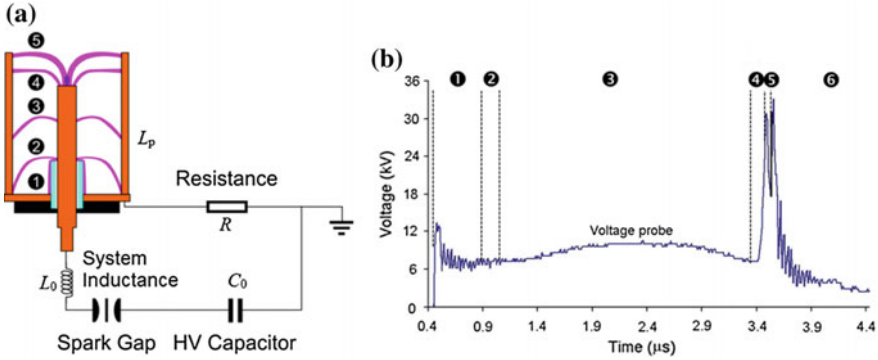


Fig. 2.12 **a** Different phases of plasma dynamics from (i) breakdown and current sheath formation ①, (ii) lift off or inverse pinch ②, (iii) axial acceleration ③, (iv) radial compression ④, and (v) pinch ⑤ phase. The post pinch phase ⑥ is not shown here. **b** The oscilloscope trace of the typical voltage probe signal with approximate timing duration marked on it

avalanche is produced when a free electron under the influence of an electric field ionizes a neutral particle and releases bound electron which become free electron for subsequent ionization. The formation of the initial discharge is heavily influenced by the gas pressure, type of filling gas used in the DPF chamber where the behavior resembles Paschen's law, and the inter-electrode distance. This discharge then evolves into a well-defined sheath of plasma. The time duration required for the formation of the well-defined axisymmetric plasma current sheath is about 100–500 ns for DPF devices having the quarter time period of about 500 ns and 3 μ s, respectively [48, 49]. This is followed by lift-off phase in which current sheath is lifted away from the insulator sleeve in an inverse pinch manner, phase ② in Fig. 2.12, to the outer electrode, the cathode, due to a radially outward component of $\mathbf{J} \times \mathbf{B}$ force. The magnetic field \mathbf{B} generated by discharge current I flowing through the anode and then through the current sheath to the ground electrode is responsible for this $\mathbf{J} \times \mathbf{B}$ Lorentz force (where \mathbf{J} is the current density). This phase is relatively short, probably about several tens of ns to hundreds of ns, and is easily recognized when the plasma sheath widens on backwall from the base away from the insulator surface and takes on a shape of a curve or parabola, caused by the radial magnetic pressure that drifts along the anode axis while maintaining electrical contact with both electrodes [50]. Zhang et al. [49], using laser shadowgraphy, showed that the curvature steepness or angle of the plasma sheath is influenced by the length of the insulator sleeve mounted at the closed end of the anode. An increase in the insulator sleeve length was found to increase the steepness angle which affected the focusing efficiency. The optimized focusing of the DPF device was found to be closely related to the current sheath steepness angle which can be adjusted through the length of the insulator sleeve, thus highlighting another important aspect of the insulator sleeve.

Driven by the axial component of $\mathbf{J} \times \mathbf{B}$ force, the current sheath then accelerates along the electrode assembly in what is commonly referred as axial acceleration phase, phase ③ in Fig. 2.12. The radial component of $\mathbf{J} \times \mathbf{B}$ force pushes the sheath outwards, leading to the mass loss through the open squirrel cage cathode. Both components of $\mathbf{J} \times \mathbf{B}$ force cause the plasma sheath to be canted as it moves axially forming an axis-symmetric parabolic shape. In this stage, the magnetic field strength is described as a smooth sinusoidal curve with field strength reaching the maximum value, owing to a maximum value of discharge current, as the current sheath reaches the open end of the assembly before entering the radial collapse phase [51]. The typical current sheath speed in axial acceleration phase is reported to be about 4–6 cm/ μ s though it can range from 2 to 10 cm/ μ s.

As the current sheath reaches the open end of the anode and starts to roll over anode, it is said to enter into radial acceleration phase ④ where it collapses on the anode axis. This fast collapse causes a sudden increase in the circuit inductance and produces anomalous electrical resistance [51]. The radial speed of current sheath in radial compression phase is about 2–2.5 time the speed in axial phase which results in extremely fast moving shock. The abrupt change in plasma characteristics in this stage is due to plasma heating mechanism and several other major contributors include shock heating, magnetic compression, and viscous heating [52]. The magnetic compression and Joule heating of the imploding current sheath also cause the heating of the plasma sheath due to the intense current flowing through it. Another major effect is the viscous heating where collisional ion–ion interaction in a dense plasma volume results in self-heating.

The fast-moving shock front ahead of the collapsing current sheath can result in plasma temperature of about several hundred electron volts; while the reflected shock at the axis, together with the magnetic compression, can finally raise this temperature to around 1–2 keV. The outgoing reflected shock from the electrode axis hits the incoming plasma current sheath slowing it down and resulting in formation elongated stable pinch plasma column. This is referred as pinch phase, depicted as ⑤ in Fig. 2.12. During the pinch phase, ion density increases from $10^{20-22} \text{ m}^{-3}$ to the order of $10^{24-26} \text{ m}^{-3}$ in pinch plasma column, increasing by a factor of 10^{4-6} , due to the densification and further ionization of a wide plasma sheath converging into a narrow column driven by the magnetic compression and secondary ionization [53]. Soon after the formation of pinched plasma columns, it breaks up due to $m = 0$ and $m = 1$ instabilities. The $m = 0$ mode instabilities (also referred as plasma diode formation in literature) accelerate the ions of the filling gas species to very high energies, up to MeV range, towards the top of the chamber and accelerate electrons to relativistic energies (100 keV and above) towards the positively charged anode.

The pinched plasma column finally breaks up and disintegrates leading to the decay of hot and dense plasma. The plasma dynamics in DPF device now can be labeled as being entering into post pinch phase; not shown in Fig. 2.12a but is

labeled as ⑨ in Fig. 2.12b. A fast-moving axial ionization wavefront, produced by the ionization caused by energetic ions, later develops into a bubble-like structure [54]. The ionizing front coincides with the beginning of the hard X-ray emission due to the interaction of energetic electrons with anode tip material and also the neutron pulses for deuterium-filled DPF device. It may be noted that the number of studies performed for post pinch phase is rather limited and almost all of those studies are limited to the time scale of the order of few tens to hundreds of ns only, though the phase may last several tens of microseconds. Martínez-Fuentes et al. [55] used a triple Langmuir probe to measure the velocity, electron density, and temperature of the plasma in the expansion discharge phase (after pinch formation) at distances between 16 and 24 cm in 4.8 kJ FN-II DPF device filled with 2.5 Torr pure deuterium gas. The values of velocity, electron density, and temperature of the plasma were reported to be 5.5×10^5 m/s, 10^{20-21} m⁻³, and 30–60 eV, respectively. Another study on 481 kJ DPF device (PF-1000) at 3.5 kPa pure deuterium showed that the free-propagating plasma stream (plasma after pinch phase) has an electron density of about 10^{23} m⁻³ and 10^{22} m⁻³ at 15 cm and 30 cm, respectively, from the electrode outlet [56]. For more details about DPF devices, readers are advised to refer to excellent reviews written by Tendys [57], Bernard et al. [58], Gribov et al. [59], and Krishnan [60]. A detailed review highlighting several applications of DPF device in plasma nanotechnology can also be found in reference [61].

2.4.3 Key Characteristics of DPF Device

The optimized DPF devices operating across entire energy range from few J to MJ exhibit many typical parameters and characteristic features of pinch plasmas, current sheath dynamics, various radiations, and energetic charged particles that are very similar and are not affected by the dimensions of coaxial electrode assembly, capacitor bank energy, peak discharge current, and the operating gas type. This has been referred as “the unique universality of plasma focus devices” by Rawat [61]. The typical values of various key parameters of interest for **optimized** DPF devices are given below.

- (i) The typical time required for the breakdown and formation of the well-defined current sheath at the start of the discharge pulse is approximately one-fifth to one-sixth of the quarter time period of discharge.
- (ii) The current sheath speed in axial acceleration phase is typically in the range of 2–10 cm/μs [62, 63] which shock-heats the plasmas to electron and ion temperatures of about 100 and 300 eV, respectively, at the end of the axial acceleration phase [64].
- (iii) The current sheath speed in radial compression phase is typically about 2–2.5 times that of the axial speed [62] and hence it can reach as high as 25 cm/μs (i.e., 250 km/s).

- (iv) The radius of the pinch plasma column, formed in the pinch phase, is approximately about 1/10th of the anode radius [65].
- (v) For DPF devices using solid anodes, the length of pinch plasma column is approximately the same as anode radius [65]. However, for the DPF device with hollow anode, the length of pinch plasma column is approximately double of the anode radius as half of the pinch plasma column is inside the anode and another half above the anode.
- (vi) The energy parameter, defined as E/V_p , where E is the energy of the charged capacitor bank and V_p the volume of the pinched plasma column, is $(1-10) \times 10^{10} \text{ J/m}^3$ for the DPF devices operating at energies between 50 J and 1 MJ [20].
- (vii) The drive parameter, also referred as speed factor, $I_0/(ap^{1/2})$ has an average value of $89 \pm 8 \text{ kA cm}^{-1} \text{ torr}^{-1/2}$ for neutron-optimized DPF device, I_0 where is peak discharge current, a is the anode radius and p is ambient gas density of deuterium [66].
- (viii) The electron/ion densities in pinch plasmas are in the range of $5 \times 10^{24} - 10^{26} \text{ m}^{-3}$ [53, 67].
- (ix) The electron and ion temperatures of pinch plasmas are in the range of 200 eV–2 keV [54] and 300 eV–1.5 keV [67], respectively.
- (x) The energies of instability-accelerated electrons, which moves towards the anode, are in the range of few tens of keV to few hundreds of keV [68, 69].
- (xi) The energies of instability-accelerated ions, which mostly move axially along the anode axis towards the top of the DPF chamber, are in the range of tens of keV to few MeV [70, 71]. The ions are mostly forward directed with most of the ions being emitted in the narrow angle of 20° with respect to the anode axis.
- (xii) The UV, soft, and hard X-rays with photon energies ranging from hundreds to several hundred thousands of eV have been measured in DPF device [49, 72–75].

The DPF devices are essentially LCR circuits, refer Fig. 2.12a, involving the transient discharge of a capacitive driver, C_0 , into an inductive-resistive load with the inductance L comprising of fixed system inductance L_0 and dynamic plasma inductance L_p and the resistance due to circuit connections. The characteristic transient discharge duration, given by $\sqrt{LC_0}$, typically ranges from few hundred ns for low energy sub-kJ DPF devices to over 10 μs for high-energy hundreds of kJ or MJ large DPF devices. Hence the durations of pinch plasma, radiation and energetic particles in DPF devices, which are typically some fraction of characteristic discharge duration, are of the order of tens of ns to about hundred or several hundred ns. This makes most phenomena of interest in DPF device being highly transient in nature. Hence, “in DPF devices the very high densities and temperatures of pinch plasmas, very high number and energy densities of high energy instability accelerated ions and electrons, intense energetic radiations such as soft x-rays and neutrons (for deuterium operated devices), fast moving shock and hot-dense decaying plasma combined with their transient nature offers a kind of plasma and

radiation environment that is drastically different from the ambience of low temperature plasmas conventionally used for material synthesis and processing”.

2.4.4 Plasma Lifetime in DPF Device and Some Features of Post Pinch Phase

It may be highlighted that Sect. 2.4.3 concentrates on or refers to the intense plasma and radiation phenomena associated with DPF device during pinch phase, phase ⑤ in Fig. 2.12, and only first few hundreds of ns of post pinch phase, the phase ⑥ in Fig. 2.12b. However, as the DPF operation is an LCR discharge, the discharge current or DPF tube voltage has damped sinusoid profile lasting over several discharge cycles as shown in Fig. 2.13a. This allows the DPF plasma to last much longer than what has been explored by almost all DPF researchers as there is sufficient electromagnetic energy available during subsequent half cycles of damped sinusoidal LCR discharge circuit of DPF.

The plasma lifetime and other features of post pinch phase in DPF device can be deduced from the optical emission spectroscopy results discussed by T. Zhang in his Ph.D. thesis [76], carried under author's supervision. An Acton 750 spectrometer was used for end-on optical emission spectroscopy to study temporal absorption/emission characteristics of primary gas (hydrogen) plasma of the filling gas species and secondary Fe/Co plasma ablated from FeCo anode top in the NX2 DPF device. One of the exit ports of the spectrometer was coupled to an intensified CCD camera which could be gated down to durations of 10 ns using Programmable Pulse Generator PG200 from Princeton Instrument. The other exit port was coupled to PMT. The spectroscopic setup on plasma focus device is shown in Fig. 2.13b. The spectra were obtained at central wavelengths of 656.1 and 526 nm, corresponding to H and Fe emission/absorption lines at different time instants with respect to the peak of the voltage probe signal and are shown in Fig. 2.13c,d, respectively.

The hydrogen spectra, with central wavelength 656.1 nm, obtained at different delays with respect to the first voltage probe peak (corresponding to first compression phase), shown in Fig. 2.13c, were obtained at 12 mbar hydrogen at 12 kV NX2 DPF operation. It is needed to point out that relatively stronger intensities at a later time are due to the use of wider gate width for the spectrometer. The spectra recorded up to 0.7 μ s show that the whole 13 nm spectral window is covered with the strong continuum, almost saturating the CCD camera. It may be important to mention here that the spectra that appear to be like that of the continuum are actually a Stark-broadened hydrogen line at 656.1 nm because of high plasma density in pinch plasma column at the anode top. It is a well-known fact that the plasma density in focused plasma column can be of the order of 10^{24} – 10^{26} m^{-3} [53, 67]. Such high plasma density results in FWHM of the Stark-broadened line to be more than 15 nm, resulting in complete coverage of the observing window of the

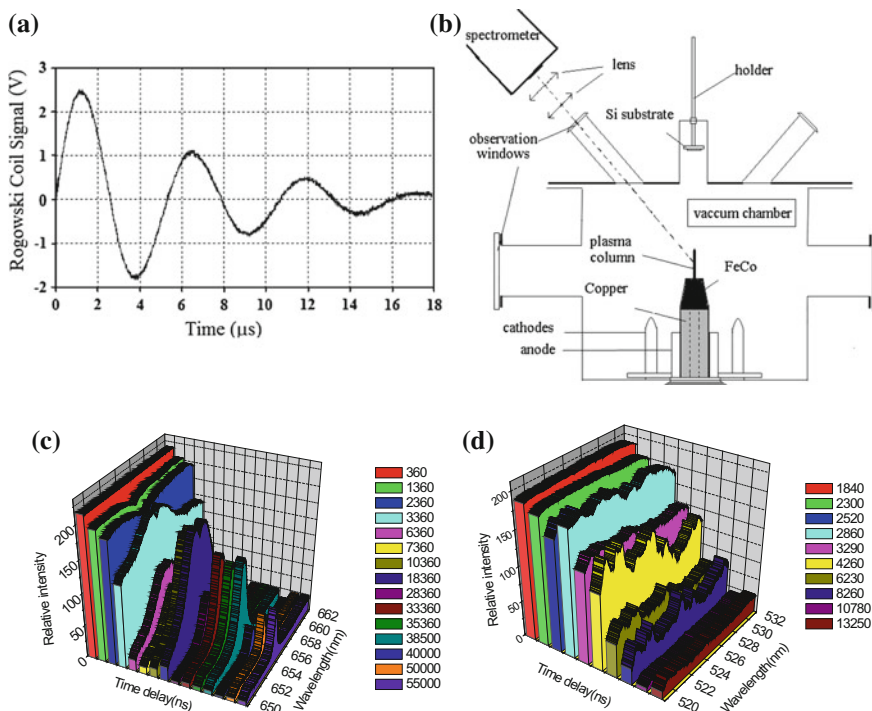


Fig. 2.13 **a** Discharge current signal taken using Rogowski coil at a high operating pressure of 25 mbar argon in NX2 DPF device showing multiple half-cycles. **b** Optical emission spectroscopy setup on NX2 DPF device with anode fitted with FeCo top and device operated with hydrogen as the filling gas [76]. **c** H emission spectra when NX2 is operated at 12 kV and 12 mbar hydrogen [76]. **d** Fe emission spectra from NX2 DPF device [76]. The delay time in colored bars in (c) and (d) are in ns. Reprinted from Zhang [76]. Permission not needed

spectrometer. The decay of focused plasma column will result in a reduction in plasma density and correspondingly the FWHM of Stark-broadened spectral line will decrease as can be seen in Fig. 2.13c with a clear emergence of the emission peak from 3.3 μs spectrum and with its continuous sharpening as time evolves. Another noticeable feature in hydrogen spectra recorded from 1.3 μs onward is the emergence of H absorption line (seen as a depression in the center of spectral peak). This absorption line is caused by the resonance absorption of hydrogen emission line emitted from hot-focused hydrogen plasma column by the bulk of the background neutral hydrogen gas (at 12 mbar) between the focused plasma column and the chamber wall. The absorption line must be there from the beginning of focused plasma column formation, but it is not observable because of the saturation of the ICCD camera. It becomes prominent when the focused plasma column starts to decay/expand decreasing the plasma density and temperature and hence reducing

the emission line intensity. The absorption line seems to disappear at about $3.9\ \mu\text{s}$ which can be attributed to the continuous reduction of neutral hydrogen zone between the focused plasma column and the exit window of the chamber because of fast expansion of the ionization wavefront [77] which while expanding pushes away the neutral gas in front of it. A reasonably strong hydrogen emission peak can still be observed as late as $55\ \mu\text{s}$; and it can probably last tens of microsecond more.

In addition to the plasma of the filling (hydrogen) gas species there will be ablated plasma of anode top material which in this case is that of Fe and Co, refer Fig. 2.13b. The time evolution of the Fe emission/absorption spectra is shown in Fig. 2.13d. Please note that Co optical emission/absorption spectra are not shown and the discussion from Fe spectra should suffice. The spectra are shown from $1.8\ \mu\text{s}$ onwards as spectra captured before that show a continuum in the $13\ \text{nm}$ spectral window of the spectrometer indicating the very high density of ablated Fe plasma. The observation of continuum, followed by absorption and finally conversion to emission line spectra of Fe can be explained as follows. The hot dense pinch plasma coupled with the instability-accelerated intense and energetic electron beam ablates the anode top resulting in the formation of hot and dense Fe/Co plasma. The ablation of FeCo anode top probably lasts several microseconds because the electron emission duration in plasma focus has been found to be longer than $1\ \mu\text{s}$ and in some cases even a second electron emission period was observed [78]. The initial ablated plasma is formed from the ablation of the solid target material and hence its density is expected to be very high. This was also observed in laser shadowgraphy results obtained by Soh et al. [77], shown in Fig. 2.14, for graphite anode top where the density of the carbon plasma ablated from graphite top is so high that it was opaque to nitrogen laser light. The hot and high-density ablated Fe/Co plasma produces emission spectra, which due to very high plasma density initially is Stark-broadened resulting in completing coverage of $13\ \text{nm}$ spectral window for spectra captured up to $1.8\ \mu\text{s}$ (not included in Fig. 2.13d). The ablated Fe/Co plasma continues to expand with time and so the plasma density and hence the corresponding Stark broadening reduces and hence the emission spectral lines are expected in the spectra. However, Fe/Co absorption lines were observed which is due to absorption of emission line (generated from plasma that is still being generated at the anode top because of long electron beam pulse duration and also due to prolonged thermal ablation time of the anode) by the relatively less hot expanding part of the Fe/Co plasma envelope. The spectra from $4\ \mu\text{s}$ onwards show only the emission lines which are attributed to the fact that the electron beam hitting and ablation of the anode ceases by this time and therefore there is no background emission source to generate absorption spectra. It can be noticed that the Fe emission lines were observed even at $13\ \mu\text{s}$ after the pinch plasma phase indicating that even the plasma ablated from the anode top, which is much lower temperature plasma as compared to compressed pinch plasma of filling gas species, lasts significantly longer to the time scale of greater than $10\ \mu\text{s}$.

The lifetime of the plasma ablated from the anode top or the plasma of the filling gas species also depends on the operating gas pressure of DPF device. It was found

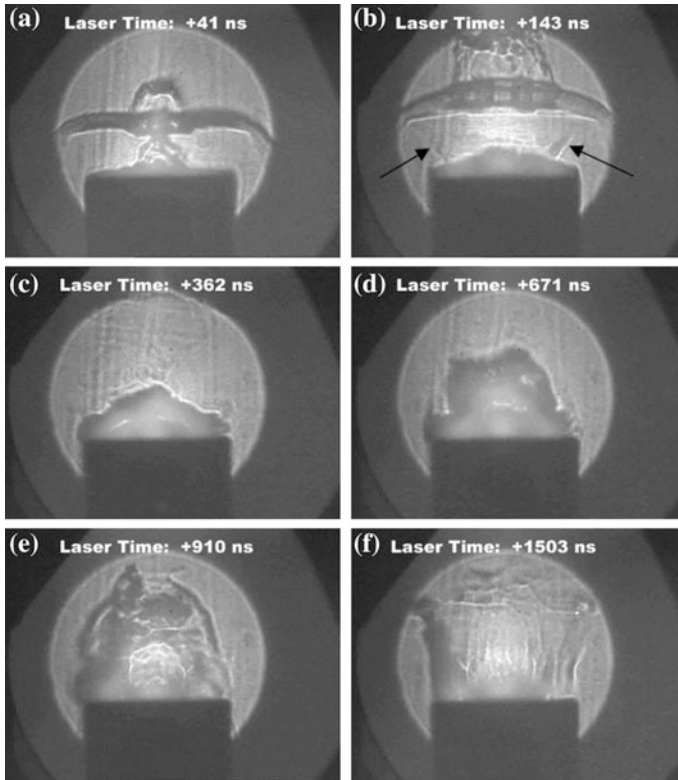


Fig. 2.14 Laser shadowgraphic images graphite anode ablation. Initially, ablated plasma is so dense that laser cannot pass through it. Ionization wavefront resulting in bubble formation can be seen in (a) and (b). Reprinted with permission from Soh et al. [77], Copyright (2004), with permission from IEEE

that the lifetime of the plasma of the filling gas species increases with the increasing gas pressure (with the pressure increase limited to the range where strong focusing or pinching efficiency can still be maintained) while that of plasma ablated from anode top decreases. The increase in the lifetime of the plasma of the filling gas species with an increase in pressure can be attributed to the increase in pinch (or hot dense plasma) volume and pinch being delayed. The increase in pressure, however, is known to adversely affect the formation and efficiency of $m = 0$ instabilities resulting a reduction in instability-accelerated electron and hence the anode ablation. Another reason could be enhanced collision between the ablated plasma and background neutral gas resulting in relatively faster collisional cooling of the ablated plasma reducing its lifetime.

2.5 Material Processing and Synthesis Using DPF Device—Timeline of Milestones

The evolutionary progress on the application of the DPF device for material processing and synthesis is shown in Fig. 2.15. The timeline of the important milestones for different materials-related application in different possible ways is shown in Fig. 2.15.

Processing of bulk target surface—the first report (1988): The first ever materials-related work using DPF was reported by Feugeas et al. [79]. in 1988 on the processing of bulk AISI 304 stainless steel substrate by the implantation of energetic nitrogen ions produced by BD-1 DPF device at the Instituto de Fisica Rosario, Argentina for surface nitriding. They used nitrogen as the working gas for the implantation of nitrogen ions into the stainless steel substrate. The DPF-nitrided stainless steel sample showed a wear reduction by a factor of 42 times compared to virgin stainless steel. It was found through XPS that the implantation of nitrogen ions by 30 exposures generated Fe₂N thin film as deep as 300 nm from the surface. Based on the nitrogen concentration in the irradiated sample, the depth of nitrogen implantation in the sample they estimated that total ion flux was about $1.3 \times 10^{17} \text{ cm}^{-2}$ over 30 DPF discharge with ion energy range up to 500 keV. This initial work showed promising application for DPF as a material processing device as the

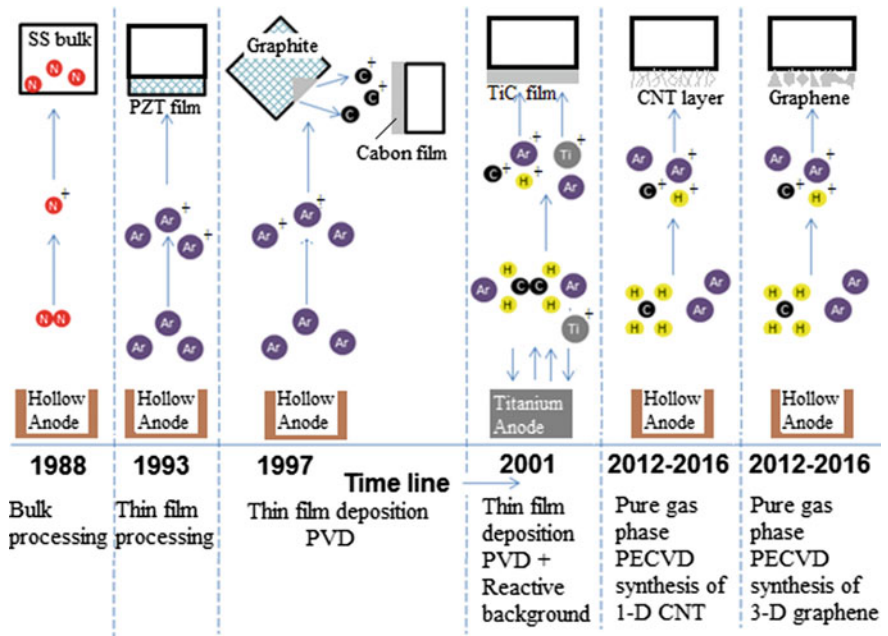


Fig. 2.15 The evolutionary progress of material process and synthesis using DPF device. Feugeas et al. [79], Rawat et al. [80, 82], Kant et al. [81], Tan et al. [83, 84]

surface of a particular material can be modified to have ceramic behavior such as Fe_2N , a wear-resistant ceramic material. The artistic impression the setup is shown in Fig. 2.16a.

Processing of thin film—the first report (1993): The first ever application in the processing of thin film, deposited by another deposition scheme, was reported by Rawat et al. [80] in 1993 using 3.3 kJ DPF device at University of Delhi, India. A material science research group at the University of Delhi was working on ferroelectric thin films of lead zirconate titanate (PZT). The group had an interest in depositing thick PZT thin film using rf magnetron sputtering. As-deposited PZT thin films were amorphous in nature and had to be annealed for transformation to the crystalline phase. However, it was found by the group that about 1 μm thick films of PZT were not crystallized even after 10 h of annealing. Many different strategies were adopted to achieve the crystallization of micron thick PZT film including the irradiation using very high-energy ion beam at the nuclear accelerator, but they all failed. Finally, 3.3 kJ UNU-ICTP DPF device was used to irradiate 0.9 μm thick PZT films by Rawat et al. [80]. The crystalline PZT was achieved by a single exposure of DPF-operated argon as the working gas although the device required minor optimization in operating parameters such as the exposure distance and operating gas pressure to prevent removal of the thin film and to achieve significant crystallization. The 0.9 μm PZT sample was successfully crystallized at an optimized distance of 4.0–4.4 cm from the anode. The setup of irradiation or processing experiment is shown in Fig. 2.16a which is similar to the processing of bulk target material discussed earlier. The crystallization of PZT was deduced to be caused by the intense and rapid heating of the amorphous material surface by pulsed

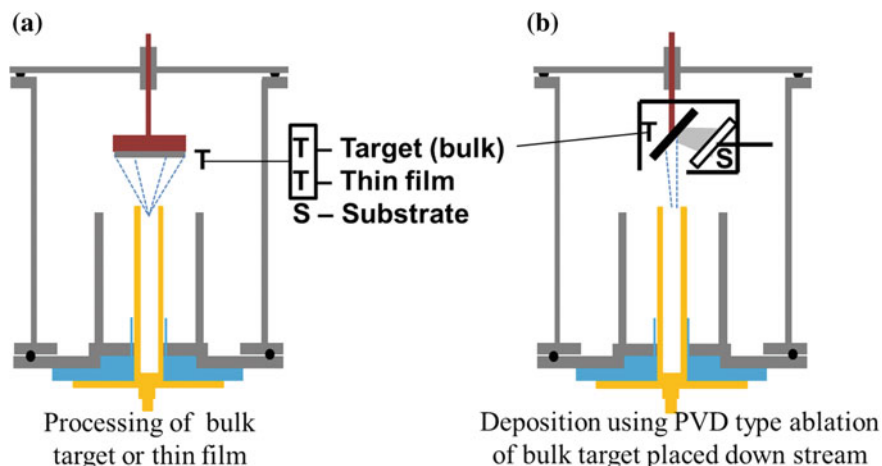


Fig. 2.16 The DPF device configurations for **a** processing of bulk target or thin film and **b** deposition or synthesis of a thin film by ablation/sputtering of a bulk target placed down the anode stream; by instability accelerated energetic ions and hot dense decaying plasma. *Note* Hollow anodes were used to minimize impurity ablation from the anode

energetic ion beam leading to a melted state. The heat from the melted surface propagates through the entire film until it reaches the film–substrate interface. Upon cooling, the entire film crystallizes. In other words, unlike both the post-processing techniques which require high temperature and prolonged processing duration, the DPF was able to produce the same effect of PZT crystallization at room temperature as well as in a short span of time.

The first synthesis of thin film—target ablation in pure PVD mode (1997):

The applications stated in two previous illustrations were related to the first ever reported use of DPF device as a materials processing device for bulk and thin film material. On the deposition front, the first ever application of DPF for deposition of materials was reported by Kant et al. [81] in 1997. They were able to deposit carbon thin films by ablating the graphite target placed down the anode stream using energetic argon ions produced by the DPF device. The schematic of the experimental setup is shown in Fig. 2.16b. A substrate, S, was placed in shielded enclosure to avoid its direct exposure to energetic ions and hot dense decaying plasma. They established that the DPF was able to produce 100–150 nm thick crystalline graphitic thin films on silicon and quartz substrates with a number of DPF shots ranging from 10 to 30 shots. The mechanism used in their approach is identical to physical vapor deposition (PVD) in RF sputtering device where ions, typically argon ions, from capacitively coupled plasma are accelerated towards target due to the electric field of the sheath region on the target surface resulting in sputtering of the target material which is then deposited on the substrate surface. In the case of a DPF device, the instability-accelerated energetic argon ions and hot dense argon plasma from pinch plasma column is accelerated towards the top of the chamber and ablated the graphite target placed downstream to deposit the ablated carbon on the substrate surface. The difference is that the DPF acts like pulsed PVD facility with a sputtering process much more intense than in conventional RF sputtering system thus allowing more efficient ablation of material.

The first synthesis of thin film by the anode ablation in PVD mode with reactive background gas (2001): Rawat et al. [82] in 2001 reported the first ever use of background reactive gas, containing the carbon precursor, along with the PVD type ablation of solid anode of titanium to synthesize nano-structured TiC thin film using 3.3 kJ UNU-ICTP DPF device. No external heating arrangement was used and the substrates were kept at room temperature and the anode top or anode inert was ablated by instability-accelerated electrons and hot dense pinch plasma much like in a PVD system. The suitable background gas was made reactive by intense DPF discharge. We still refer it as DPF in PVD mode with reactive background gas. For deposition of TiC films, the conventionally used central hollow copper anode was changed to a solid titanium one whereas the outer cathode rods were kept the same as shown in Fig. 2.17a. The argon-acetylene admixture was used as the working gas. Throughout the experiment, the filling gas pressure of argon-acetylene admixture, in the ratio 7:3, was kept at 1.5 mbar. This work opened a new era of DPF device application whereby many kinds of ceramic materials such as metal nitrides, metal carbides, metal oxides, etc., were deposited using anode of

suitable material and with desired working gases such as nitrogen, methane or acetylene, and oxygen.

In many of the works reported later instead of replacing the entire anode by solid anode, many of the researchers either replaced only the anode top by machining and attaching the desired material piece, shown in Fig. 2.17b, or by using a relatively small anode insert as shown in Fig. 2.17c. The strategy of replacing the anode top by desired material piece [77], Fig. 2.17b, has the advantages of using a smaller amount of material in comparison to the full solid anode and avoiding any impurity from anode material as the ablation occurs only at the anode top. This configuration, however, can be used only for metallic or graphite as anode top which are conductive in nature and does not affect the plasma dynamics of DPF device as seen in shadowgraphic images in Fig. 2.14 where graphite anode top was used. The strategy of using the material to be ablated as anode insert [85], totally inside conventional hollow anode as shown in Fig. 2.17c, has advantages of (i) using very small amount of material, (ii) no machining requirement, and (iii) even non-conducting materials can be used. However, this strategy suffers from a major drawback that the anode rim, which is a different material, also ablates and contributes to impurities in deposited layer. The impurity ablation from anode rim, however, can be minimized by making anode wall very thin.

The first synthesis of pure gaseous precursor based process—pure PECVD mode (2012–2016): Carbon nano-structures such as nanotubes, nanowalls, and graphenes have been regarded as an advance material due to their vast and unique properties with great potential in many commercial applications. Many apparatus and techniques have been employed in producing and commercializing carbon nano-structures. Currently, the preferred method of preparing them is chemical

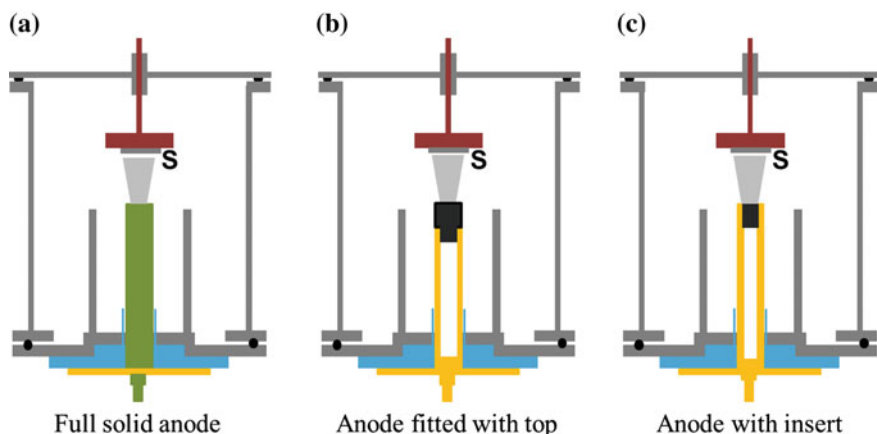


Fig. 2.17 Different type of anode configuration used for deposition of thin film synthesis which relies on ablation of anode material by backward moving energetic electrons and hot dense plasma of DPF pinch

vapor deposition (CVD) where a carbon feedstock, process gas, and catalyst are fed into a furnace at high temperature which decomposes the carbon feedstock while allowing for the catalyst to initiate the CNTs growth. The Plasma-Enhanced CVD (PECVD) systems where a CVD system is improved by using a microwave discharge, or a capacitive discharge, or an inductive discharge are becoming popular as they allow the chemical reaction to take place at a lower temperature. Our group at PRSL, NIE/NTU, Singapore, has successfully synthesized vertically aligned carbon nanotube at very high instantaneous growth rates at low substrate temperatures through the use of DPF with the assistance of a catalyst coated substrate and a substrate heater. It is demonstrated that 2 μm long vertically aligned carbon nanotube can be successfully grown using pulsed plasma that lasts for a maximum of about 100 μs in a single DPF shot giving rise to the enormous instantaneous growth rate of about 2 cm/s. The same device with different operating conditions can be tailored to produce graphene nanoflower structures. This pioneering was done by K.S. Tan during his Ph.D. program at Nanyang Technological University, Singapore [83, 84]. This work highlights the first ever use of DPF device in pure PECVD (plasma-enhanced CVD) mode with the use of hollow copper anode, heated substrate surface and pure gas based (using carbon-containing gaseous precursor) synthesis of one-dimensional CNT and three-dimensional graphene nanoflowers. More details are provided later.

Other strategies for material synthesis and processing using DPF devices: It may be important to mention that there may be other processing and deposition strategies that might have been developed or used but are not included in timeline and milestone developmental work listed in Fig. 2.15. This can be purely incidental or may be due to very limited use of those methods. For example, Zhang et al. [68] reported the optimization and application of NX2 DPF device as pulsed electron beam source for deposition of thin film FeCo. The arrangement of their experimental setup is shown in Fig. 2.18a where the electron beam was extracted through the hole in the anode in the lower deposition chamber attached to the anode and high voltage flange. The pulsed electron beam was used to ablate the FeCo target and the nano-structured FeCo thin films were deposited on the substrate placed across. They used CCD based magnetic electron energy spectrometer to deduce that hydrogen should be the first choice as filling gas for DPF operation for electron-based target ablation for thin film deposition as it produces highest electron beam charge and higher energy (from 50 to 200 keV) electrons. They claim the first ever thin film deposition using PFPED (Plasma Focus assisted Pulsed Electron Deposition) using hydrogen operated NX2 DPF device. Similarly, Mohanty et al. fabricated the network of polyaniline nanowires at room temperature in microsecond timescale by using the pulsed electron beam of a plasma focus device [86]. The experimental setup used by them is shown in Fig. 2.18b.

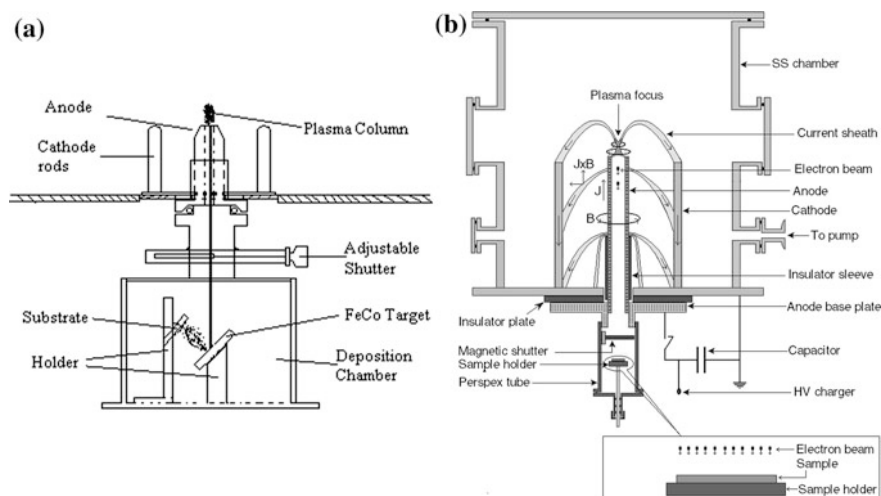


Fig. 2.18 **a** Pulsed electron beam based deposition of thin films in deposition chamber attached to the lower end of the NX2 DPF device. **b** Schematic of experimental setup for electron beam processing of polyaniline thick films; with magnified view of electron beam interaction process with film. Reprinted from **a** Zhang et al. [68], Copyright (2007), with permission from IOP Publishing; and **b** Mohanty et al. [86], Copyright (2009), with permission from Elsevier Ltd

2.6 Material Processing Using DPF Device

The typical DPF setup for the processing of bulk or thin film samples used is the UNU-ICTP facility in our lab in NTU, Singapore is shown in Fig. 2.19a. For efficient processing of samples in DPF device, one should take note of following characteristics of DPF device and use the appropriate strategies according to the requirement or proceedings of the experiment

- (i) The DPF devices, like any other plasma device, lacks the exact reproducibility, i.e., there is variation in device performance (and hence the radiation and charged particle yield) from one shot to another. To minimize the shot-to-shot variation in performance of the DPF device it should be conditioned to achieve efficient pinching. Unwarranted exposure of the sample to the less-efficient conditioning shots is avoided using a mechanical shutter between the anode top and the sample, as shown in Fig. 2.19a. The conditioning of DPF ensures reliable shot-to-shot operation of DPF device. Once the good focusing efficiency, monitored by current and/or voltage probe, is achieved then the shutter is removed and the sample is exposed or deposited in subsequent DPF shots. The conditioning process needs to be repeated for each fresh loading of a new sample.
- (ii) As mentioned earlier, in each DPF shot the irradiated sample is processed by a complex mix of instability-accelerated energetic ions, high-energy

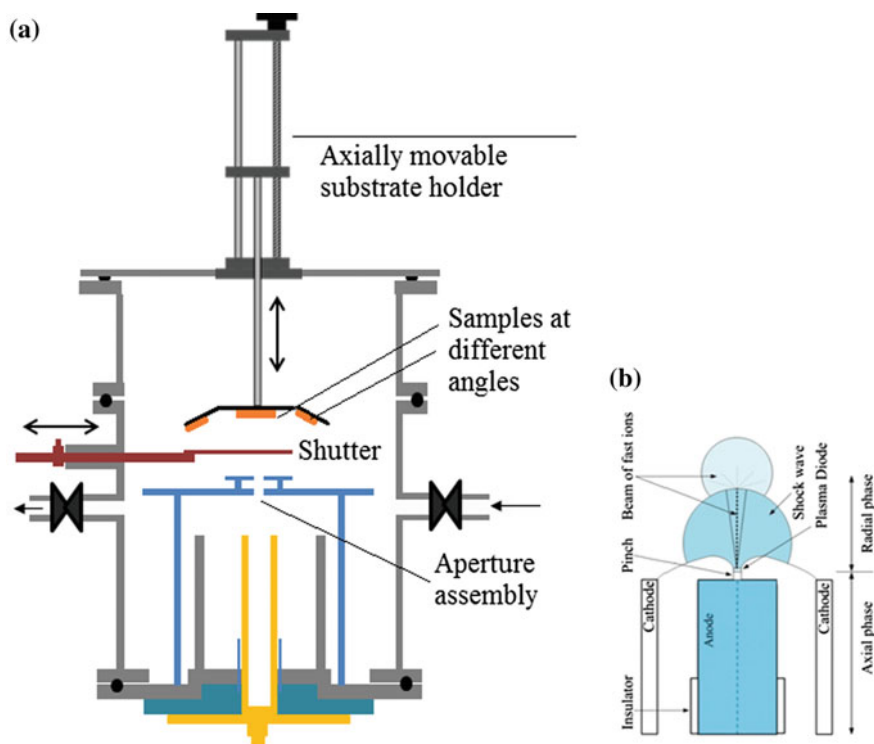


Fig. 2.19 **a** Schematic of DPF as a bulk and thin film processing facility. **b** The pinch column above anode acts like a point source of the fast ion beam and hot-dense decaying plasma. The schematic in (b) is reprinted from Nawi et al. [88] (Open access no permission needed)

high-flux photons, fast moving ionization wavefront, strong shock wave, and hot and dense decaying plasma. The source of above-mentioned energetic plasma, ions and radiation source is the pinch plasma column which from the end-on direction behaves like a point source [87]. Energetic ions and plasma emitted from a point source (tip of pinched plasma column) spread out and expand as shown in Fig. 2.19b. Moreover, this flux of energetic ions and hot dense decaying plasma is forward directed with the highest number and energy densities along the anode axis. The number and energy density of ions and decaying plasma decrease in radial direction with increasing angle from the anode axis. This angular dependence of number and energy density of energetic ions and plasma species plays the key role in controlling the processing conditions of the irradiated target surface and deposition features on the substrate surface. The angular variation is much more evident at a smaller distance of material processing or deposition. This leads to greater inhomogeneity in processing or deposition at smaller distances. However, as the distance is increased, the area within the same solid angle increases

leading to greater homogeneity in processing or deposition over a larger area at a larger distance from anode top. Hence, with the increasing distance of exposure, the ions/radiation/plasma flux will decrease or in other words the energy flux delivered at different distances of exposure is different. This gives the possibility of a different degree of processing of the sample by simply changing its exposure distance from the anode top and also by using a different number of DPF exposure shots. The exposure distance and angular position of the sample can simply be changed using an axially moveable sample holder with mounting positions along the axis as well as at different radial position from the anode axis as shown in Fig. 2.19a.

- (iii) Depending on the application, one should carefully choose the gas to be used as the operating media. Inert gases such as neon and argon have been used in many studies where the aim was to simply process the material to change its physical characteristics without affecting its composition. For the fusion relevant studies, where the aim is to test the performance of the first wall candidate material, one needs to use deuterium as the filling gas. This provides 2.45 meV D-D fusion neutrons along with other intense radiations. To simulate more realistic fusion reactor type irradiation conditions it will be desired to have 14 meV fusion neutrons by operating the DPF device with 1:1 D-T gas mixture. The handling and procurement of tritium, however, is not trivial and only certain selected groups only can probably do these experiments. The processing of bulk or thin films for the purpose of doping or the nitride, oxide, and carbide formation will require the use of reactive gas environment such as nitrogen, oxygen, acetylene, methane, etc., in DPF chamber.

2.6.1 Mechanism and Physical Processes for Material Processing in DPF Device

The processing of bulk or thin/thick film material in DPF device is a very complex process due to a complex mix of energetic ions, hot decaying plasma, radiation, and shock, shown in Fig. 2.19b. The mechanism of material processing in DPF device **is not unique** as it strongly depends on the exposure position and distance of the material from the anode top. Five different material processing positions and distances from the anode top are possible which are marked in Fig. 2.20a as position “1” to position “5”. These five positions are: (1) within the pinch region, (2) very close to the exit point of the pinch, (3) at moderate distance from the anode top (surface melting possible), (4) large distance from the anode top (no surface melting), and (5) below the anode top inside the hollow anode or in the chamber attached to the anode.

The sample placed within pinch region: The sample placed at the position marked as “1”, in Fig. 2.20a, can be placed in two different orientations: horizontal

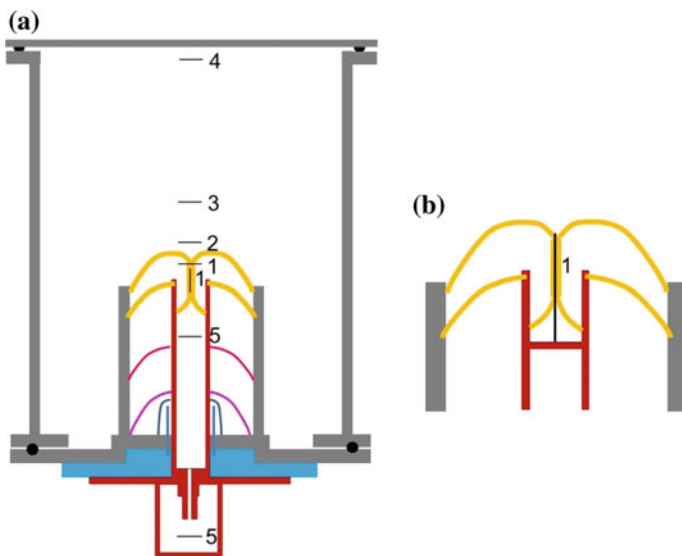


Fig. 2.20 **a** Five different material processing positions in DPF device. Note two different orientations for position marked as “1” inside the pinch region. **b** Wire type sample mounted along the anode axis using support

or vertical. For the planar sample, both these orientations at position “1” obstruct and interfere with pinching plasma. The shadowgraphic study of plasma dynamics showed that any target/sample placed at a distance less than the anode radius, i.e., within the pinch region, will severely affect the plasma dynamics [89] and will not allow the pinch to take place and hence all subsequent phases of plasma focus are disrupted. Sample exposure at this position does not allow the sample to be exposed to the fast ion beam, hot dense plasma, and strong shock. Hence it is not advisable to expose planar samples at this position. However, thin cylindrical wire type sample can be exposed at this position by mounting them using a support as shown in Fig. 2.20b. In an unpublished work done at the University of Delhi, India, the group conducted experiments of Langmuir probe measurements in dense plasma focus device by mounting tungsten wire probe tip at many positions including the position 1 shown in Fig. 2.20b. The pinching efficiency of DPF device was not affected by tungsten wire along the anode axis, but the plasma was so intense that the tip did not last for more than three–five shots.

The sample placed very close to the exit point of the pinch: The exposure of target sample placed very close the exit point of the pinch, marked as position “2” in Fig. 2.20a and also shown in Fig. 2.21d, is discussed in great detail by Gribkov et al. [90]. With the help of extensive fast gated imaging and time-resolved interferometry, they demonstrated the generation of cumulative plasma stream (referred as a jet) at the conical compression of the imploding pinch plasma current sheath shown in Fig. 2.21b. The plasma jet is guided by the axial magnetic field (B_z)

formed by the compression of Earth's magnetic field and residual field of construction material of DPF chamber by the imploding current sheath by the azimuthal (B_ϕ) magnetic field, refer Fig. 2.21a. The fast-moving plasma jet produces a shock wave (SW) in the residual gas above the pinch shown in Fig. 2.21c. They estimated the speed of deuterium hot plasma stream (plasma jet + SW) to be about $\sim 3 \times 10^7 \text{ cm s}^{-1}$ with the energy of about 1 keV. If the target sample is placed very close to the pinch exit point, Fig. 2.21d, then this hot plasma stream (plasma jet + SW) hits the target surface with the power density of about $P_{\text{pl}} \approx 10^{10} \text{ W cm}^{-2}$ for PF-1000 DPF device over the sample surface of about few cm^2 . This results in intense head load on target surface leading to surface melting and generation of secondary plasma (SP) which starts moving in the direction opposite to the incoming primary plasma. They estimated the temperature of this secondary plasma, produced by hot plasma stream, of the order of 10 eV. It may be noted over here that the above-mentioned physical processes are taking place before the pinch disruption, i.e., when the pinch is stable and the instability-accelerated fast ions have not been generated yet. This shows the strong ablative/sputtering effect of hot plasma stream at very close distance of exposure. This secondary plasma which is moving toward the anode/pinch may or may not interfere with the pinching plasma

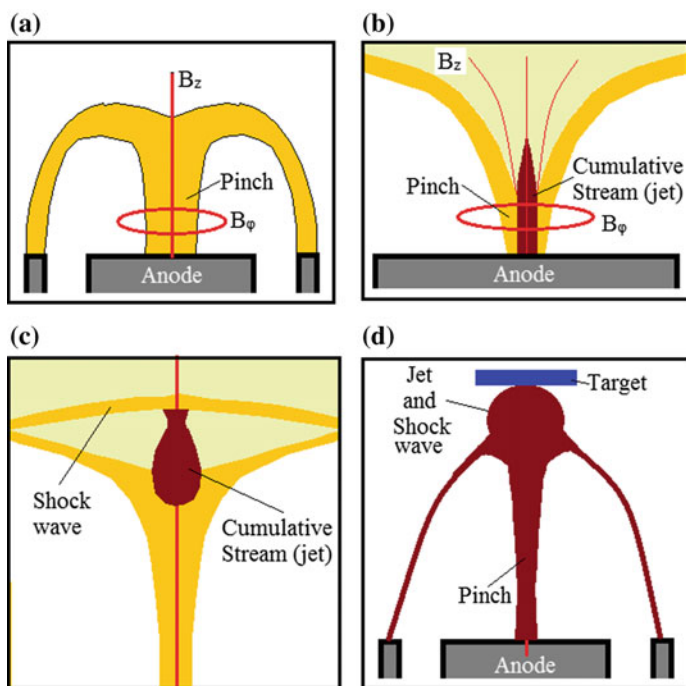


Fig. 2.21 **a** Implosion phase of the DPF plasma and magnetic field dynamics, **b** generation of plasma jet/stream, **c** plasma jet and shock wave produced by jet, and **d** target sample placed very close to the exit point of the pinch

dynamics depending on target distance from pinch exit point. Assuming that the pinch dynamics is not affected then the kinetic stage of DPF dynamics follows.

The kinetic stage of DPF device consists of “current abrupton”, plasma diode formation (a term normally used by Gribkov et al. [90] which is referred as $m = 0$ instability formation in this chapter earlier and by others as well) and generation of fast energetic beam of ions and electrons. The plasma diode (or $m = 0$ instability), shown in Fig. 2.22, results in a very strong local electric field of the order of 10 MV cm^{-1} resulting in acceleration of ions and electrons in opposite directions. The ions have been observed to have energies from several tens of keV to several MeV [70, 71]; while the electrons have energies from several ten to several hundred keV [68, 69]. According to Gribkov et al. [90], the fast ion beam has two components; the first component is magnetized in the combined B_ϕ/B_z magnetic field and escapes from the pinch within cone of angle of about $25\text{--}30^\circ$ (shown by cone in Fig. 2.19b) and the second component, the main part, propagates in a relatively narrow cone of 5° along the line of singularity of B_ϕ field, i.e., the anode axis where $B_\phi = 0$. The narrow main part of the fast ion beam, comprising of ions of average energy of the order of 100 keV, results in small spot size of the order of few mm^2 on the irradiated target surface with very high-power density [90] of about $10^{12} - 10^{13} \text{ W cm}^{-2}$. Such high-power density of fast ions results in the generation of another set of secondary plasma from the targets placed at closer distances to the pinch. This secondary plasma was observed to be moving at a speed of $\sim 10^7 \text{ cm s}^{-1}$ with the

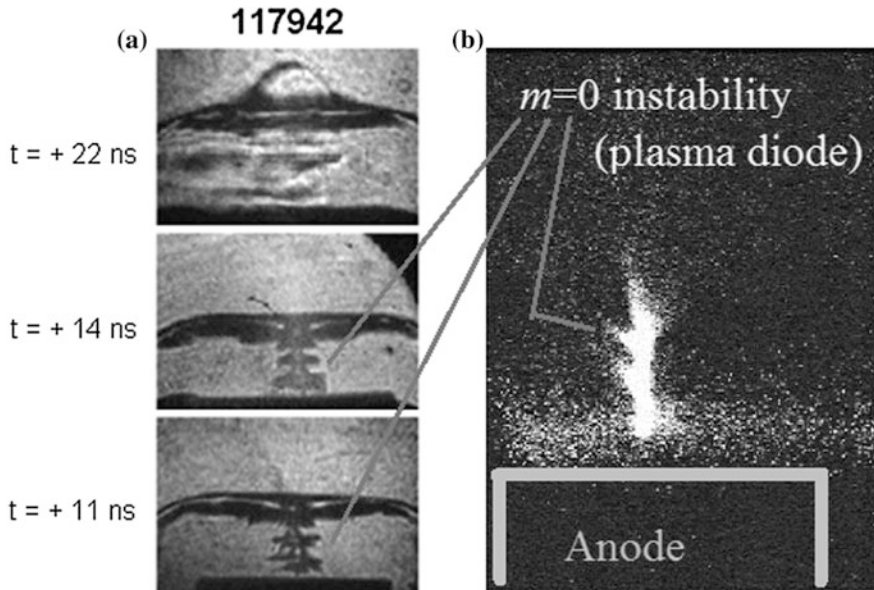


Fig. 2.22 **a** 1-ns three laser sequenced shadowgrams, and **b** time integrated soft X-ray image; all showing plasma diode ($m = 0$ instability) formation in DPF device. **a** Reprinted from Rafique et al. [93], Copyright (2010), with permission from Springer

energy of about hundreds of eV. Recently, ion beam fluences and flux for various gases, at the exit point of the pinch, in a DPF device have been numerically estimated and reported by Lee and Saw [91, 92]. Hence the target/substrate sample placed nearer to the pinch exit point suffers greater ablative/sputtering damage as both the hot plasma stream (comprising of keV plasma jet and SW during stable pinch phase) and instability generated fast energetic ions (comprising of ions of tens of keV to MeV energy during the pinch abruption phase) result in secondary plasmas from irradiated surface. It may, however, be noted that the power densities of hot plasma stream and fast ions beam mentioned above are specific to the large PF-1000 device. For smaller DPF devices the pinch volume, and hence energy content in pinch, is much smaller as they scale on anode radius. Hence the effects on sample surface will be different.

The ablative/sputtering generation of secondary plasma will have two different effects on the irradiated surface: (i) the surface reconstruction and (ii) thin film formation if a reactive background gas is used. This will be explained with the help of suitable examples in later sections. In addition to material melting and ablation in the form of secondary plasma, the high-energy fast ions (>100 keV ions) are capable of moving deep inside the bulk target surface, from several hundred nm to micrometer distance, with the ability to dislodge bulk atoms from their lattice positions creating vacancy defects in crystalline structure. The penetration depth of ions and vacancy defects in bulk or thin film targets of various materials can be estimated using SRIM© [94].

Sample at a moderate distance from the anode top (surface melting possible): This exposure position is marked as “3” in Fig. 2.20a. The instability generated beam of fast ions initially propagates behind the shock wave as it is generated later in time and does not spread much, as seen in Fig. 2.19b. However, as it pierces through the shock wavefront, the ions find themselves in neutral gas with density same as that of the ion beam. The fast ions escaping the shock front, supported/guided by diverging B_z field due to increased distance from pinch regions, turn in the direction of grounded chamber walls resulting in the greater spread of fast ions as shown in Fig. 2.19b. The increasing spread of fast ions will reduce the fluence on the target surface with increasing distance of exposure. The mean free path of very high-energy ions, say hydrogen ions of >100 keV, will be greater than 60 cm in hydrogen at 6 mbar. The very high-energy ions, hence, will not be able to ionize the working gas before they hit the target or the chamber wall.

At moderate distances of exposures, the delivery of high flux and high-energy instability-accelerated ions, energetic radiations, shock exposure and hot dense decay plasmas in a very short time (with different events lasting from few tens of ns to several μ s) results in the processing of material in DPF device which is equivalent to ultra-fast annealing. Sanchez and Feugeas [95] estimated the generation of intense transient heating slopes and heating speeds as high as ~ 3600 K μm^{-1} and ~ 40 K ns^{-1} respectively, on various metal sample surface confirming the ultra-fast annealing rate in DPF device. The rapid surface temperature rise, beyond evaporation point, followed by the rapid cooling results in a strong thermal effect on the material exposed at a moderate distance which brings out the changes in their

several physical properties and compositional characteristics. In addition, the high-energy ions can also induce defect in crystalline structure of irradiated materials.

Sample at large distance from the anode top (no surface melting possible):

At large distances from the pinch region, marked as position “4” in Fig. 2.20a, due to the conical geometry of ion beam, the number and energy density of ions are greatly reduced on the sample surface. This leads to insignificant processing of the irradiated sample surface.

The sample placed inside the hollow anode or in the chamber attached to the anode: These positions are marked as “5” in Fig. 2.20a and also shown in Fig. 2.18b. In this case, the sample is essentially processed by instability-accelerated energetic electrons which move in a downward direction through the annular hollow space of the anode. Roshan et al. [96], though, demonstrated the existence of backward moving high-energy ions in NX2 DPF device using the direct and unambiguous technique of nuclear activation. They conducted a 30 shot sequence at 1 Hz repetition rate in NX2 DPF device at 8 mbar deuterium and showed significant activation of graphite mounted as an insert inside the anode top by high-energy deuterons moving in the backward direction. Their estimates showed 1.3×10^{11} backward deuterons per shot per steradian with energies higher than 500 keV. They estimated that the number of backward deuterons was about one order of magnitude less than the forward ones. Hence, for the samples placed at position “5” mainly electrons and to some extent ions will be responsible for processing. At smaller distances of exposure below the anode top, in the negative direction, the charge particle number and energy flux will be strong enough to cause rapid thermal melting and re-solidification of the sample surface. The effect obviously will decrease with the increasing negative distance. Based on self-luminescence and laser interferometric images of plasma diode formation, it was deduced that after that an acceleration of electrons in plasma diode by the vortex electric field takes place followed by the self-focusing of the electron beam inside the pinch during its propagation to the anode [90]. Moreover, it was inferred from Rogowski coil and magnetic spectrometry measurements that electrons from pinch region are accelerated towards the anode over a relatively long period of microseconds and that too in several bunches [78, 97]. Hence, the sample irradiated by electrons in downward direction depending on the distance of exposure will have nonuniform irradiation with electrons bunch focusing at a different place on the irradiated sample. This was observed on polyaniline thick films irradiated by electron beams in DPF device where polyaniline nanowires were observed to form at scattered locations and not uniformly on the entire irradiated surface [86].

Next, we will illustrate the application of DPF device for material processing by a transient complex mix of radiation, shock, plasma, and charged particle using selected examples.

2.6.2 Selective Examples of Material Processing

This section is divided into two subheadings (i) processing of bulk substrates and (ii) processing of thin films.

2.6.2.1 Processing of Bulk Substrate Surface

The first experiment on processing of bulk substrate of AISI 304 stainless steel using DPF device was reported in 1988 [79] and after that several experiments have been conducted on processing of many different bulk substrate materials, such as titanium [95, 98–103], different types of stainless steel [95, 104–106], silicon [107–113], aluminum [114–116], zirconium [117–123], zirconia [124], tungsten [125], tantalum [126], boron nitride [127], alumina [127], PET [128], etc. This shows that wide range of materials such as metals, semiconductors, ceramics, and polymers have been processed using DPF devices. Some of the key features of DPF-based processing are discussed under following subheadings.

Surface Reconstruction: Fig. 2.23 shows typical SEM (scanning electron microscopy) images of the Ti and W samples before and after being processed by DPF. The bulk samples were processed at smaller distances from the anode top using different DPF devices (UNU-ICTP and PF-6 devices, respectively, in this case). The processed samples show the surface reconstruction with nano-structures being formed on them. The surfaces of the unexposed Ti and “Eurofer” ferritic steel substrates are shown in Fig. 2.23a, d, respectively. The low-magnification image in Fig. 2.23a shows linear scratch marks on unexposed Ti sample surface formed during mechanical polishing by abrasive silicon carbide paper. As discussed in the previous section, the exposure of bulk substrate samples to an efficiently pinching DPF shot at lower distances of exposure causes an extreme transient temperature rise of the top few micron thick layer of the sample surface which results in sputtering, melting, and re-solidification of the top layer. This melting and re-solidification result in surface reconstruction, as seen in Fig. 2.23b, with the removal of initial mechanical polishing marks along with substantial smoothening of the Ti sample surface which was irradiated at an axial distance of 5 cm using nitrogen operated 30 shots in UNU-ICTP type device. In addition to the surface smoothening, one can also observe the crack formation in Fig. 2.23b. The crack formation can be attributed to the stress formed between the bulk cold solid substrate and transiently melted and re-solidified top surface layer upon DPF exposure [129]. Similar surface reconstruction has been observed in several other processing experiments using DPF devices, such as the one reported recently by Chernyshova et al. [130] and is shown in Fig. 2.23e, f. The ferritic steel “Eurofer” sample showed surface reconstruction within one shot in PF-6 DPF device, refer Fig. 2.23e, with the wavelike structure on the surface with initial traces microcrack nucleation. The wavelike structures, cracks, and craters were strongly developed on the sample surface after five shots, as seen in Fig. 2.23f.

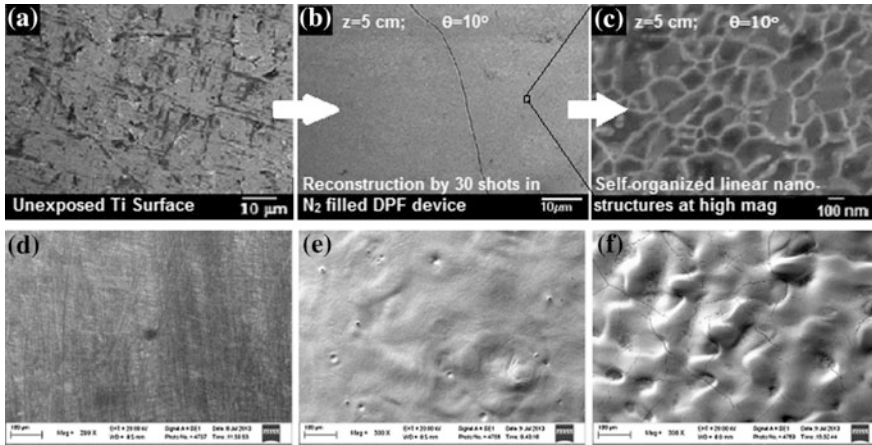


Fig. 2.23 **a** Virgin Ti sample surface, **b** Ti sample surface after exposure to 30 DPF shots in at axial distance of 5 cm at angular position of 10° with respect to anode axis, **c** magnified image of part of image in **(b)**, **d** virgin ferritic steel “Eurofer” sample, **(e, f)** exposed to 1 and 5 shots in PF-6 device. Reprinted from **a–c** Rawat [129], IOP Publishing (Open Access paper no permission needed); and **d–f** Chernyshova et al. [130], Copyright (2016), with permission from Elsevier Ltd

Surface Nano-structurization: Fig. 2.23c, the SEM image at higher magnification on DPF processed Ti sample surface, shows the formation of self-organized linear nano-structures. It may be mentioned that the dark gray islands observed in Fig. 2.23c are not large grains but itself composed of very small nanoparticles (not visible at this magnification) within the boundaries of these linear nano-structures.

Figure 2.24a–c shows the SEM images of bulk Ti substrate processed by two different methane-operated DPF devices; 190 kA, 3.2 kJ single shot UNU/ICTP and 430 kA, 3.1 kJ NX2 devices. The comparison of SEM images in Fig. 2.24a, c shows the formation of titanium oxycarbide nanoparticles on the substrate surface exhibiting the reproducibility of the results from two independent devices. The size of nanoparticles is about 35–50 and 20 nm in Fig. 2.24a, c respectively. The bigger size of nanoparticles in Fig. 2.24a is attributed to the higher energy and material flux due to exposure at a lower distance as well as the being conducted along the anode axis. The off-axis irradiation at an angular position of 10° with respect to anode axis as well as at a higher distance of 9 cm results in lower ion number and energy flux at the irradiated substrate surface leading to smaller nanoparticle size for SEM image shown in Fig. 2.24c. The SEM image of the Ti substrate exposed along anode axis in the NX2 device, shown in Fig. 2.24b, exhibits features similar to the one observed in Fig. 2.23c with linear nano-structures. The greater details about the structure, composition and hardness of the nano-structured nanocomposite titanium oxycarbide layer formed on DPF irradiated Ti substrate surface can be found in our paper [100]. The Fig. 2.24d–f shows SEM images of the unexposed and irradiated tungsten samples. The high magnification image of unexposed W samples, Fig. 2.24d, shows variable sized and shaped grains and pits on the rough surface but it does not

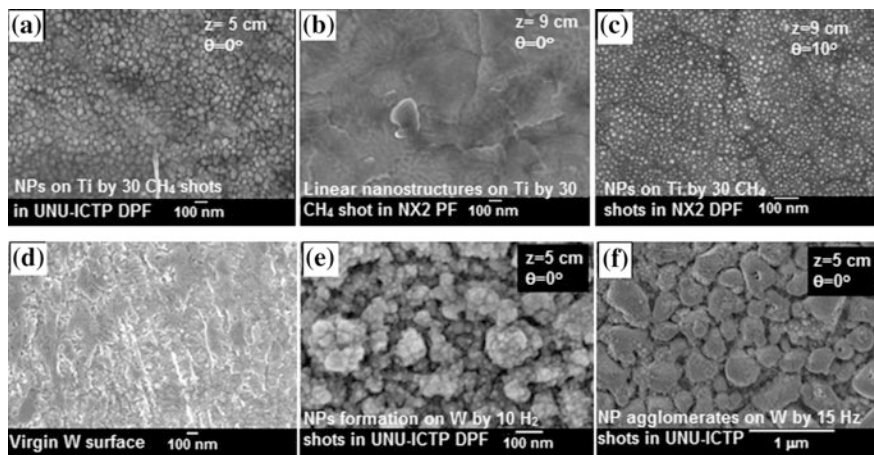


Fig. 2.24 a–c SEM images of Ti samples processed in methane operated UNU-ICTP and NX2 DPF devices at different distance and angular positions. d–f Virgin and irradiated W samples. The distance (z) and angular position (θ) of the samples, the number of DPF irradiation shots and DPF operating gas for each of the exposure experiment are mentioned in SEM images. Reprinted from Rawat [129], Copyright (2015), IOP Publishing (Open Access paper no permission needed)

show any nano-structures. The SEM images of 10 and 15 shot irradiations in hydrogen operated UNU/ICTP DPF device, shown in Fig. 2.24e–f respectively, exhibit the formation of nanoparticles and nanoparticle agglomerates on the irradiated tungsten surface. The size of nanoparticles is about 15–20 nm for 10 shot irradiation and they also agglomerate resulting in particle agglomerates with size varying from 100 to 300 nm. The tungsten sample irradiated with 15 shots shows mostly particle agglomerates of about 200–800 nm in size. These big size particle agglomerates are made up of 40–60 nm sized nanoparticles. The increase in nanoparticle and particle agglomerate size with the greater number of irradiation shots can be attributed to enhanced transient thermal treatment of the sample surface.

Changes in properties of processed materials: In addition to morphological changes, several other properties of the processed sample may change which includes (i) surface layer composition, (ii) lattice structure, (iii) hardness, etc. The changes in crystal structure, hardness, and other physical properties are discussed in detail in Chap. 7 on hard coating synthesis using DPF device so we will not touch on those aspects over here. However, the processes or the reasons for the change in surface properties are discussed over here. For the examples cited in the previous paragraph, the use of background reactive gases such as nitrogen and methane results in TiN [101] and nanocomposite titanium oxycarbide (TiC_xO_y) [100] layer formation, respectively, on the Ti substrate surface. For the sake of illustration, we will discuss the formation of a TiN layer on Ti substrate processed in nitrogen operated DPF device on the basis of physical processes discussed in Sect. 2.6.1. The DPF discharge results in fast primary nitrogen plasma stream, shock wave, and fast energetic nitrogen ion beam based sputtering of Ti substrate surface resulting in

the formation of a secondary plasma of Ti in front of the irradiated substrate surface. This secondary titanium plasma interacts with background nitrogen plasma to form TiN in the gas phase or on Ti substrate to fabricate a nitride layer. Thus the gas phase nucleation may be the first step towards TiN layer growth, assisted by the direct ion-assisted compound layer formation due to implantation of energetic nitrogen ions interstitially. In a dynamic process like plasma focus based nitriding, ion implantation and ion sputtering take place simultaneously which results in surface modification and grain formation. The dimension of grains/crystallites depends on the lattice structure of the resultant TiN compound, reaction kinetics, diffusion rate of nitrogen, and mass loss due to ion sputtering. The thickness of the TiN coating is dependent (i) on the depth of ion implantation in the substrate which depends on the highest energy nitrogen ions in fast ion beam and (ii) on TiN compound layer formation by re-deposition of gas phase nucleated titanium and nitrogen plasma mix. As the processing was done using multiple DPF shots, the successive ion pulses will process the pre-deposited TiN layer to improve the quality of TiN layer with possible re-sputtering as well. The temperature evolution during irradiation also enhances the reactivity of the nitrogen already introduced during the preceding shots. This provides the additional energy required for surface diffusion and migration of nitrogen, and thus enhances the crystallinity of the TiN layer. The TiN layer formed on top of the Ti substrate surface results in different crystalline structure and hardness properties as shown in Fig. 2.25 [101]. Similar changes in surface stoichiometry, crystalline structure, and other physical properties (hardness, electrical conductivity, surface energy, water contact angle, etc.) are observed for other processed materials.

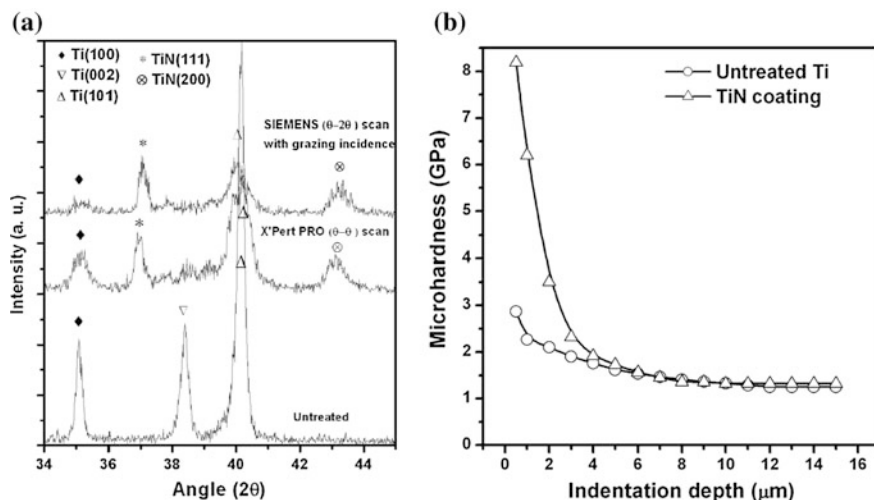


Fig. 2.25 Change in crystalline structure (a) and hardness (b) of titanium substrate upon being processed by nitrogen operated DPF device due to TiN layer formation. Reprinted from Hassan [101], Copyright (2009), with permission from Elsevier Ltd

2.6.2.2 Processing of Thin/Thick Films

A good number of thin/thick films have been processed using DPF devices though the amount of work done in this field is rather limited compared to processing of bulk material. Thin films processed by DPF include PZT [80], CdS [131], hematite [132], Sb_2Te_3 [133], CdI_2 [134], ZnO [135] and FePt [136–138], and thick films of polyaniline [86, 139]. The processing of thin film is much more interesting as changes in many different types of properties such as crystallinity, grain size, stoichiometric, optical, electrical, and magnetic properties have been reported. While Rawat et al. [80] reported the crystallization of amorphous PZT thin films, the amorphization of crystalline thin films of CdS was reported by Sagar and Srivastava [131]. The non-magnetic $\alpha\text{-Fe}_2\text{O}_3$ (hematite) thin films were exposed to argon ion beam at different distances from the anode top by Agarwala et al. [132]. At a particular distance, at 10 cm in Fig. 2.26a, hematite film was converted completely to magnetite (Fe_3O_4) form which is ferromagnetic in nature. The transformation was attributed to the loss of oxygen from the irradiated iron oxide film resulting in decreased amount of oxygen relative to iron leading to Fe_3O_4 (with 1.33 oxygen atom per iron atom) formation from $\alpha\text{-Fe}_2\text{O}_3$ (with 1.5 oxygen atom per iron atom). The change in magnetic property was thus due to stoichiometric variation in the irradiated sample. A substantial reduction in film thickness was observed for DPF processing performed at smaller distance indicating the significant sputtering of material, in line with changes observed for bulk material. Another demonstration of stoichiometric variation in DPF irradiated thin films was demonstrated by Rawat et al. [133] for antimony telluride. Vacuum evaporation based as-deposited films of antimony telluride contained mixed phase comprising of both stoichiometric (Sb_2Te_3) and antimony-rich non-stoichiometric (Sb_3Te_2) phases. The processing of mixed-phase antimony telluride film at lower distances by high-energy ion flux broke chemical bonds resulting in further enhancement of Sb-rich non-stoichiometric phase and oxidation in the film. A higher distance of exposure with a right dose of lower ion energy flux led the conversion of mixed-phase antimony telluride thin film to single stoichiometric (Sb_2Te_3) phase.

Rawat et al. investigated the processing of CdI_2 thin films by argon ions in UNU-ICTP DPF device [134]. The as-grown film, deposited by a thermal evaporation method, were essentially 4H polytype (002) oriented CdI_2 stoichiometric films. The argon ion irradiation changed the orientation to (110) at certain moderate irradiation distances as shown in Fig. 2.26b. The diffraction peaks shifted towards higher 2θ values from their corresponding powder data indicating uniform compressive stress. The estimation of grain size from SEM and residual stress from diffractograms showed a linear increase in grain size (shown in Fig. 2.26c) and residual stress with increasing irradiation distance (or decreasing ion energy). The morphology of the films with (002) preferred orientation was found to be similar to each other but with different grain sizes. The films with (110) orientation, however, was found to have different morphology. The direct optical energy gap, E_g , of the ion-irradiated films was found in the range of 3–3.3 eV. The E_g was found to increase linearly at the rate of 15 $\mu\text{eV/atm}$ with the compressive stress.

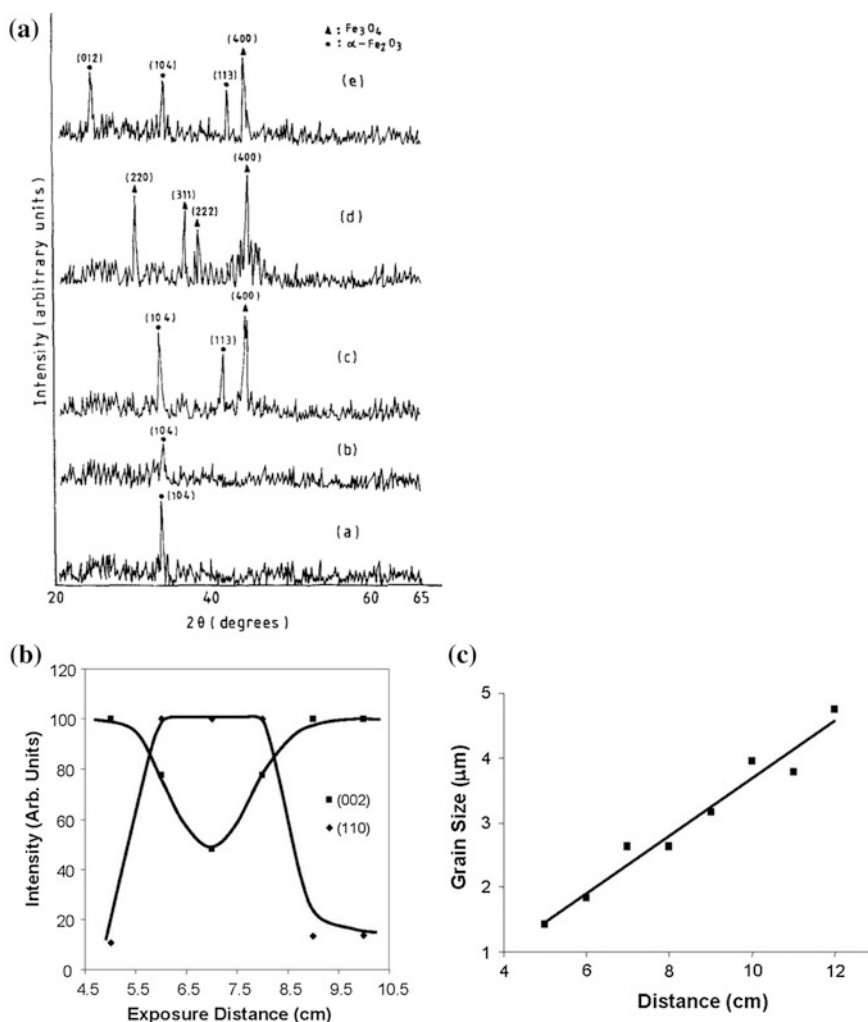


Fig. 2.26 a XRD patterns of virgin iron oxide (a) thin film and ion irradiated samples at 8, 9, 20 and 11 cm from (b–e). Variation in crystalline orientation from (002) to (110) plane (b) and grain size (c) of CdI_2 thin films at certain distances of exposures. Reprinted from a Agarwala et al. [132], Copyright (1997), permission from Elsevier Ltd and b, c Rawat et al. [134], Copyright (2004), with permission from AIP Publishing

One of the most interesting applications of DPF device in thin film processing is the nano-structurization of thin/thick films. The nano-structuring of FePt thin films in hydrogen operated DPF device [136–138] and polyaniline thick film in nitrogen operated DPF device [86] has been demonstrated. The FePt thin films were processed in conventional forward direction by hydrogen ions whereas the polyaniline (PA) thick films were processed by backward moving relativistic electron beam

after being extracted through the hollow anode in a separate chamber attached to the bottom exit point of the anode as shown in Fig. 2.18b. The 67 nm thick FePt thin films samples were grown using pulsed laser deposition method and processed in 3 kJ hydrogen operated UNU-ICTP DPF device by Jiayi et al. [136] at a distance of the 5 cm from the anode top, while the few tens of micrometer thick PA films prepared by chemical oxidation method were exposed in 2.2 kJ Mather-type nitrogen operated DPF device [70] by Mohanty et al. [86]. The SEM images in Fig. 2.27a show the change in surface morphology from the smooth uniform film for the as-deposited sample to the film with uniform and isolated nanoparticles after a single DPF shot exposure with an average size of about 9.1 ± 2.3 nm. The DPF irradiation using two shots resulted in agglomeration of FePt nanoparticles to about 51.3 ± 7.4 nm sized agglomerates. Z.Y. Pan et al. repeated the experiments with 100 nm thick PLD grown FePt thin films and were able to reproduce nano-structuring of FePt thin films, refer Fig. 2.27(d), in hydrogen operated UNU-ICTP DPF device using different number of focus shots [137] as well as different exposure distances (5, 6, and 7 cm) [138]. The mechanism of nano-structuring of the DPF exposed thin film can be understood from the characteristics of instability-accelerated ions of the filling gas species. Though the ion energy is found to vary over a very big range from few tens of keV to few MeV, the mean energy of the bulk of the H^+ ions in UNU-ICTP DPF has been estimated to be 124 keV [136]. The projected range of the H^+ ions of this mean energy is about half-micrometer in FePt, as estimated from SRIM[®]. Therefore, most of the H^+ ions stop and deposit the bulk of their energy in the silicon substrate at the Bragg peak position as the thickness of FePt thin films was only about 67 or 100 nm. This would result in heating of silicon substrate to a very high temperature in a very short span of time. The thermal energy is then conducted to the FePt thin films and causes the diffusion of metal atoms either through the lattice or along grain boundaries. The diffusion releases the thermal expansion mismatch stresses between the silicon oxide layer of the silicon substrate surface and the PLD coated FePt thin film, leading to the formation of nanoparticles at the surface layer of FePt thin films. One of the biggest advantages of nano-structuring using a DPF device is that it can achieve nano-structuring of the thin film in single shot exposure with ion pulse duration of the order of a few hundred ns compared with hours of irradiation time required for other reported continuous ion sources [140].

Figure 2.27d shows the TEM bright-field image for the single shot ion irradiation sample after 400 °C annealing. The image shows relatively uniform size distribution for nanoparticles with average particle size of about 11.6 ± 3.4 nm. The selected area electron diffraction (SAED) pattern, in the inset of Fig. 2.27d, shows that FePt nanoparticles are in polycrystalline fct phase. It may be important to mention over here that ion irradiation has assisted not only in the FePt nanoparticles formation (from FePt thin films) but also in lowering the phase transition temperature to 400 °C. The phase transition at lower temperature, for single focus shot irradiation, has restricted nanoparticles grain size growth and agglomeration resulting in relatively small and well separated magnetically hard fct phase FePt nanoparticles; much needed for higher magnetic data storage density. Figure 2.27e

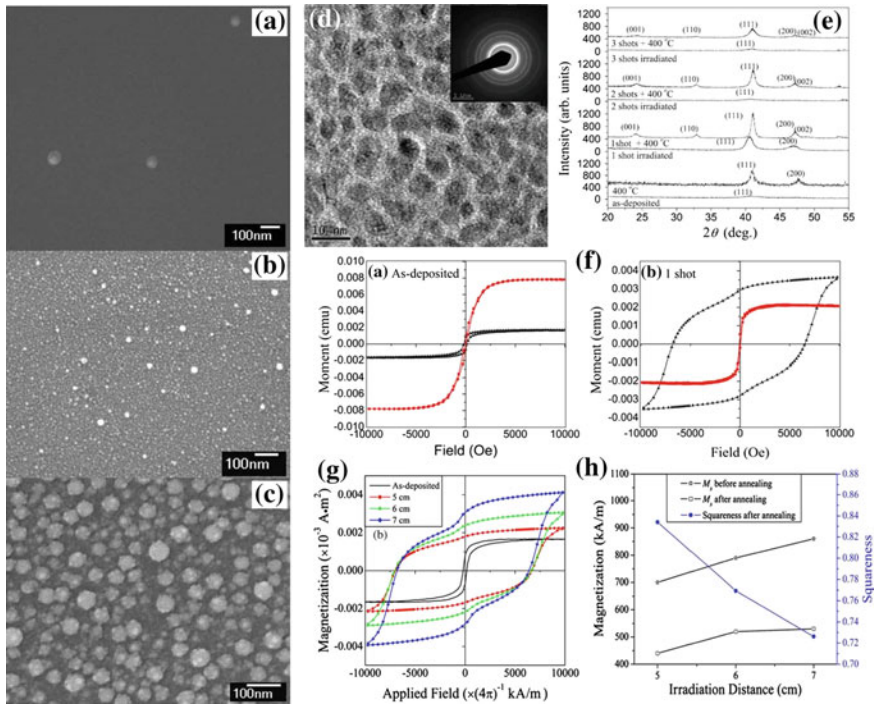


Fig. 2.27 SEM images of **a** as-deposited and DPF irradiated FePt thin films at 5 cm from anode top using one **(b)** and two **(c)** DPF shots; the nanoparticle formation was observed on irradiated films. **d** TEM image of FePt nanoparticles formed in single DPF irradiation at 4 cm distance. **e** XRD patterns of as-deposited and DPF processed FePt film samples before and after 400 °C annealing. **f** An enormous increase in magnetic hardness (higher coercivity) of DPF processed and annealed sample. **g, h** Variation in magnetic properties such as coercivity, magnetization and squareness of FePt samples irradiated at different distances. Reprinted from **(a–c)** Lin et al. [136], Copyright (2007), permission from IOP publishing; **d–f** Pan et al. [137], Copyright (2009), with Springer; and **g, h** Pan et al. [138], Copyright (2009), with permission from Elsevier Ltd

shows the XRD patterns of (i) as-deposited, (ii) annealed at 400 °C (without ion irradiation), (iii) ion irradiated (without annealing) and (iv) ion-irradiated samples after annealing at 400 °C. The as-deposited FePt sample exhibits fcc phase with a broad and weak peak of (111) which after annealing at 400 °C remains in fcc phase but with significantly improved (111) peak intensity and emergence of (200) peak. The sample after single plasma focus irradiation shot, without annealing, shows almost similar XRD patterns as the FePt sample after 400 °C annealing with (111) and (002) fundamental peaks of fcc phase. This implies that single shot of pulsed plasma focus ion irradiation provides almost equal amount energy that is offered by conventional thermal annealing for 1 h at 400 °C. The average crystallite size for single shot ion-irradiated sample, as estimated from the (111) peak using Scherrer formula, is smaller than that of average crystallite size of sample annealed at 400 °C. The smaller average crystallite size can be attributed to transient

annealing by pulsed ion irradiation. With the increase in the number of plasma focus irradiation shots to two and three, the crystallinity of the irradiated alone samples decreases and reverses to that of as-deposited sample. Increased number of irradiation shots provided more than required energy inducing more defects (both the vacancy and interstitial) and lattice distortion leading to lattice disordering. The annealing of all ion-irradiated samples at 400 °C led to the phase transition in the FePt film from disordered fcc structure to chemically ordered fct structured $L1_0$ phase, confirmed by the appearance of the superlattice tetragonal (001), (110) and (002) peaks. However, with the increase in the number of ion irradiation shots the intensity of the superlattice peaks of fct phase become weaker, suggesting that the ordering of the fct crystallite lattice is reduced. The sample irradiated by one shot and annealed at 400 °C exhibited an enormous increase in its magnetic hardness (coercivity) as seen in Fig. 2.27f as compared to as-deposited sample. A similar increase in magnetic hardness (coercivity) was also observed for FePt thin films samples processed at different distances from the anode top, Fig. 2.27g, indicating very high reliability in reproducing results. Figure 2.27h shows that other magnetic properties of the FePt thin film samples also change with the change in processing distance from the anode top due to change in number and energy flux of the ions.

2.7 Material Synthesis/Deposition Using DPF Device

The material syntheses or depositions using DPF devices are mainly in the form of thin films of many different types [44, 68, 77, 82, 120, 123, 141–156]. The large variation in the type of thin films deposited using DPF devices is due to various possible configurations that have been used and were discussed in detail in Sect. 2.5 and summarized in Fig. 2.15. In this section, we will highlight advantages and criticism of DPF devices based syntheses and depositions.

2.7.1 Advantages of DPF-Based Depositions

The main advantages of DPF device as deposition facilities are as follows:

1. High deposition rates.
2. Ability to grow crystalline thin films at room temperature substrates.
3. Superior physical properties.
4. Versatile deposition facility with variety of deposition options.

2.7.1.1 High Deposition Rates

The deposition rates in DPF devices can be extremely high, much higher than other deposition methods. We will illustrate this with the help of selected examples. Figure 2.28 shows the cross-sectional SEM images and thickness of CoPt thin films deposited using a different number of shots in NX2 DPF device at a low operating voltage of 8 kV with a stored energy of the capacitor bank in sub-kJ range (~ 88 J) [146]. It clearly shows that the thickness of the as-deposited samples increases continuously with increasing number of plasma focus deposition shots with the thicknesses of the as-deposited samples about 44.0 ± 2.0 , 72.5 ± 4.0 , 208.1 ± 8.0 , 294.5 ± 14.0 and 331.7 ± 12.0 nm for the 25, 50, 100, 150, and 200 shots deposition samples, respectively. The curve of the variation of the thickness of the deposited sample with varying number of plasma focus shots is plotted in Fig. 2.28f, which is linearly fitted to estimate the deposition rate of the nano-structured CoPt thin films at a fixed distance of 25 cm and the filling hydrogen gas pressure fixed at 6 mbar. The slope of the linear fitted curve reveals the average growth rate of CoPt nanoparticle deposition when the other operation parameters were fixed. It is estimated to be about 1.78 nm/shot. This deposition rate is more than 30 times higher as compared with that of conventional PLD which is found to be about 0.50 Å/shot by Lin et al. [157]. It may also be mentioned over here that the target to substrate distance in case of PLD deposition by PLD was only 3 cm [157], much less compared to that of 25 cm for DPF deposition. This clearly indicated that deposition rates in DPF are actually may be more than two orders of magnitude higher than that of PLD device.

The extremely high deposition rate of ZnO thin film has been demonstrated by Tan et al. [158] using zinc top fitted anode in UNU-ICTP device with pure oxygen being used as the operating gas. Figure 2.28g shows the cross-sectional SEM image of ZnO film deposited using 30 focus shots at 15 cm from anode top with a film thickness of about 2.82 ± 0.32 μm . They estimated the ZnO deposition rate to be about 100 nm per shot at the deposition distance of 15 cm. In 3 kJ UNU/ICTP device, the ablation plume of graphite anode top was found to last for about 2 μs for DLC thin film deposition experiments [77]. Even if we assume the anode top ablation duration to be about 10 μs , the estimated transient ZnO thin film deposition rate would be a staggering 10 mm/s. However, the transient deposition rate is not as important as the average growth rate, which depends on the repetition rate (operating frequency) of the DPF device, and will be lower as DPF devices have limited repetition rates. Tan et al. performed ZnO synthesis in single shot mode with one shot per minute, which is the standard practice for UNU/ICTP device to avoid overheating of the electrical system and anode target which may change the DPF operational characteristics. This accounts for an average growth rate of about 0.1 $\mu\text{m}/\text{min}$ in their study, similar to the reported growth rate found in RF magnetron sputtering devices [159, 160]. On the other hand, when the DPF system operates in repetitive mode, multiple exposures can be made within a second and this leads to the assumption of increased deposition rate. One such DPF device that can perform such operation is the high-performance high repetition rate NX2

plasma focus facility. The NX2 is a 3 kJ, 27.6 μF Mather-type DPF device with a repetition rate of up to 16 Hz and has routinely been operated between 1 to 10 Hz operation for X-ray lithography related work [161]. As for material synthesis, the device in repetitive mode has been demonstrated to work for the synthesis of bimetallic FeCo nanoparticles at 1 Hz repetition rate [68]. The deposition of ZnO thin film in NX2 plasma focus device at 1 Hz repetition rate operation will lead to a time averaged deposition rate of 6 $\mu\text{m}/\text{min}$, which could further be enhanced to 60 $\mu\text{m}/\text{min}$ at 10 Hz operation. Operating beyond the 10 Hz operations would surpass the highest known deposition rate of an inductively coupled microplasma system [162]. These deposition rates are expected to surpass any existing device, along with material synthesis at room temperature substrates. Additionally, in DPF device even the room temperature deposition provides a polycrystalline ZnO thin film without any need for post-deposition annealing which is invariably needed for ZnO thin film depositions in other devices. Further improvements of the DPF device in terms of growth rate can be expected since a 50 Hz repetitive DPF device has been developed [163]. However, high repetition rate operation creates several design considerations as the plasma focus anode will require a cooling arrangement for thermal load management due to high heat dissipation to the anode by pinch

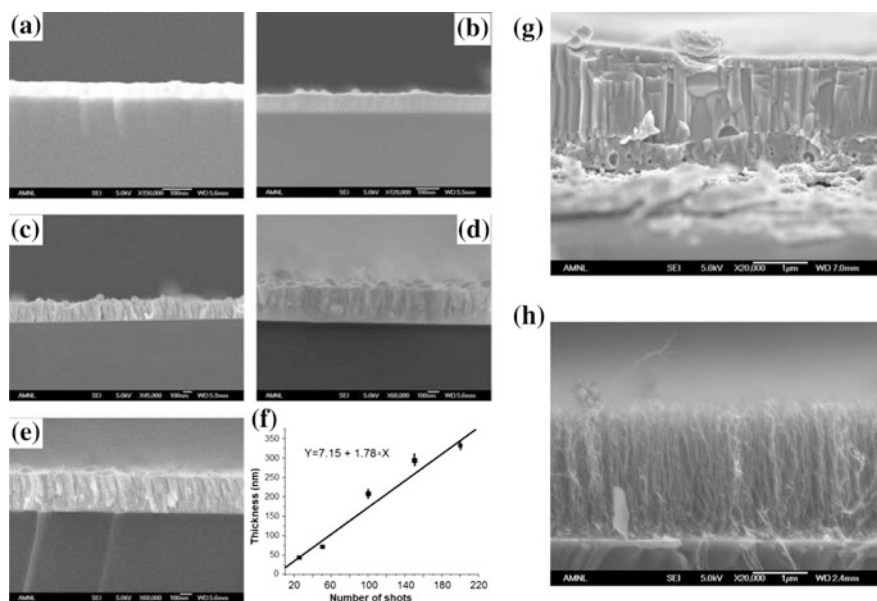


Fig. 2.28 a–e Cross-sectional SEM images of CoPt thin films deposited using 25, 50, 100, 150 and 200 NX2 DPF shots, respectively, at 25 cm from anode top. **f** Film thickness variation with the number of deposition shots. **g** Cross-sectional SEM of ZnO thin film deposited using 30 shots in UNT-ICTP DPF at 15 cm from anode top. **h** Single shot synthesis of carbon nanotube in UNU-ICTP DPF device. Reprinted from a–f Pan et al. [146], Copyright (2009) with permission from IOP publishing; and g, h Tan [83, 84] (Permission not needed)

plasma. This would require significant modification to the anode design with water cooling arrangement before the high repetition rate experiments can actually be performed.

It may be noted that while CoPt thin film synthesis (Fig. 2.28a–e) was purely PVD-type deposition by the ablation of CoPt anode top, the ZnO synthesis was PVD synthesis with reactive background gas of oxygen. Figure 2.28h shows the pure gas phase PECVD synthesis of carbon nanotube (CNT) in single UNU-ICTP DPF shot [83, 84]. The length of CNT is about 2 μm in single shot synthesis in Fig. 2.28h. So if assume the discharge plasma duration to be of the order of 100 μs (refer to the discussion of plasma lifetime in Sect. 2.4.4 where the H plasma emission peak is observed even at 55 μs in Fig. 2.13c) then the CNT transient growth rate is staggering 20 mm/s, double that of ZnO transient growth mentioned above, and far more greater than CNT growth rate in any other device.

2.7.1.2 Ability to Grow Crystalline Thin Films at Room Temperature

In almost all the experiments conducted using DPF devices, it has been demonstrated that thin films can be deposited directly into crystalline phase at room temperature substrate. No in situ annealing was required to achieve the crystalline phase. Figure 2.29 shows XRD patterns of TiN [141], ZnO [158] and TiO₂ [145] thin films deposited using DPF device on room temperature substrates. The ability to deposit thin films directly in crystalline phase at room temperature substrate highlights the critical role played by high-energy-density plasma and energetic ion processing during the deposition process

Figure 2.29a shows the XRD patterns of TiN thin film samples deposited at fixed distance of 7 cm using different numbers (10, 20, and 30) of DPF shots at different angular positions. Not only the films deposited along the anode axis (labeled as “Centre”) but also the one deposited at off-axis positions at different angular positions (labeled as “Off-centre” and “outermost”) were all crystalline in nature. The crystallinity, however, was highest for the samples deposited along the anode axis and it decreased with increasing deposition angle. The crystallinity was also found to increase with the increasing number of shots.

The XRD of ZnO thin films, in Fig. 2.29b, also demonstrate the deposition of highly crystalline thin films with (002) preferred orientation at room temperature substrate. Author’s group at NTU has done a good amount of work on a dilute magnetic semiconductor for transition metal doped ZnO synthesis [135, 164–168]. The ZnO thin films for those studies were synthesized using PLD deposition method and were mostly amorphous or very weakly crystalline at room temperature deposition conditions; and either in situ or post-deposition annealing was required to get the a good crystalline film.

Figure 2.29c shows XRD spectra of the as-deposited TiO₂ (titania) thin films on Si substrate at room temperature for a different number of DPF deposition shots viz. 25, 50, 75, and 200. In the notation of Miller indices, “A” indicates anatase-type crystal, and “R” indicates rutile-type crystal. The XRD spectra reveal that the film

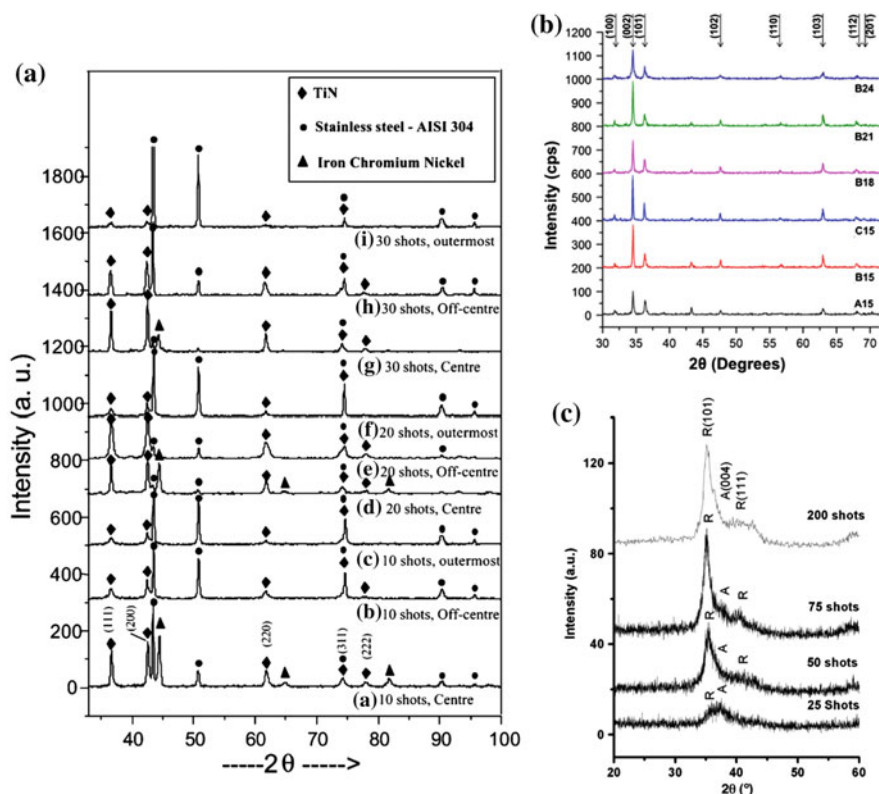


Fig. 2.29 Direct crystalline phase synthesis at room temperature substrates for various thin films, **a** TiN, **b** ZnO and **c** TiO_2 . Reprinted from **a** Rawat et al. [141], Copyright (2003) with permission from Elsevier Ltd; **b** Tan et al. [158], Copyright (2015), with permission from IEEE; and **c** Rawat et al. [145], Copyright (2008) with permission from Elsevier Ltd

deposited with 25 shots is anatase with a broad diffraction peak. The film deposited with 50 shots shows the presence of a weak (111) and a strong (101) rutile peaks along with the anatase (004) peak shoulder. For the films deposited with 75 and 100 shots, only rutile phase is evolved with (101) preferred orientation. The crystalline nature of the as-deposited titania thin films using multiple focus shots at room temperature substrate made DPF-based deposition different from most of the studies reporting amorphous titania thin films grown on substrates at room temperature [169, 170]. The crystallization from amorphous to anatase and from anatase to rutile usually occurs in the temperature ranges of 450–550 and 600–700 °C, respectively. But in DPF-based deposition, we achieved both anatase and rutile phase in as-deposited titania samples at room temperature deposition with multiple shots. This confirms the highly energetic deposition process or strong in situ transient thermal annealing in DPF device which allows room temperature crystalline phase formation. Hence DPF-based deposition can be used for direct crystalline phase thin

film depositions on soft substrate materials such acrylic, plastics, or other polymers which cannot be annealed at a higher temperature for phase transformation purposes.

2.7.1.3 Superior Physical Properties

There are numerous examples whereby superior physical properties are exhibited by DPF-deposited thin films compared to the films deposited by other methods. In order to illustrate this, we will use few selected examples. For example, one of the best depositions of oxygen-rich ZnO thin films by PLD method in author's lab is reported in a paper by Usman et al. [166] whose XRD and PL (photoluminescence) spectra are shown in Fig. 2.30a, b. Chemically synthesized oxygen-rich ZnO power (with Zn/O ratio of 0.71) was used for PLD pellet preparation. The ZnO target rotating at 33 revs/min was ablated by second harmonic Nd:YAG laser (532 nm, 26 mJ) at pulse repetition rate of 10 Hz. The ZnO thin films were deposited on Si (100) substrate for constant ablation duration of 90 min in the ultra high vacuum of 10^{-6} Torr. Post-deposition annealing was carried out at different temperatures ranging from 500 to 800 °C for 4 h in air. The XRD of all annealed samples exhibited polycrystalline wurtzite structure; as-grown films were weakly crystalline. A typical ZnO PL spectral is known to exhibit characteristic UV (centered about 3.37 eV or about 370 nm) and defects-related deep level green-yellow (1.8–2.8 eV range) emissions. The UV band emission, centered at about 3.37 eV originates from the exciton recombination corresponding to NBE exciton emission of the wide bandgap ZnO. The DLE in green and yellow emission spectra is related to the variation in intrinsic defects of ZnO thin films, such as zinc vacancy (V_{Zn}), oxygen vacancy (V_o), interstitial zinc (Zn_i), and interstitial oxygen (O_i) [171]. The room temperature PL spectrum of PLD grown ZnO thin films annealed at 700 °C, shown in Fig. 2.30b, exhibited small NBE UV emission peak at ~ 385 nm (3.23 eV) and relatively stronger and broad DLE defect (green) emission centered at ~ 520 nm (2.39 eV). The DLE spectrum, as seen in Fig. 2.30b, can be deconvoluted with four peaks centered which correspond to zinc vacancy (V_{Zn}), oxygen vacancy (V_o), interstitial zinc (Zn_i) and interstitial oxygen (O_i) defects. The presence of much stronger DLE peak indicates that intrinsic defects are quite high in PLD grown ZnO thin films. All other samples also exhibited similar PL spectra. In comparison, the PL spectra of DPF grown ZnO thin film samples, shown in Fig. 2.30d, exhibit quite contrasting nature with much stronger NBE emission compared to DLE emission indicating a low concentration of intrinsic defects [158]. The samples deposited at 15 cm with increasing number of deposition shots (A15, B15, and C15) show a gradual blue shift of NBE peak from 3.23 to 3.28 eV and gradual decrease in relative intensity of defects-related broad green-yellow DLE band. The sample C15, deposited with 30 focus shots at 15 cm, does not exhibit DLE emission band that indicates intrinsic defects-free ZnO thin film in this sample. The gradual decrease in

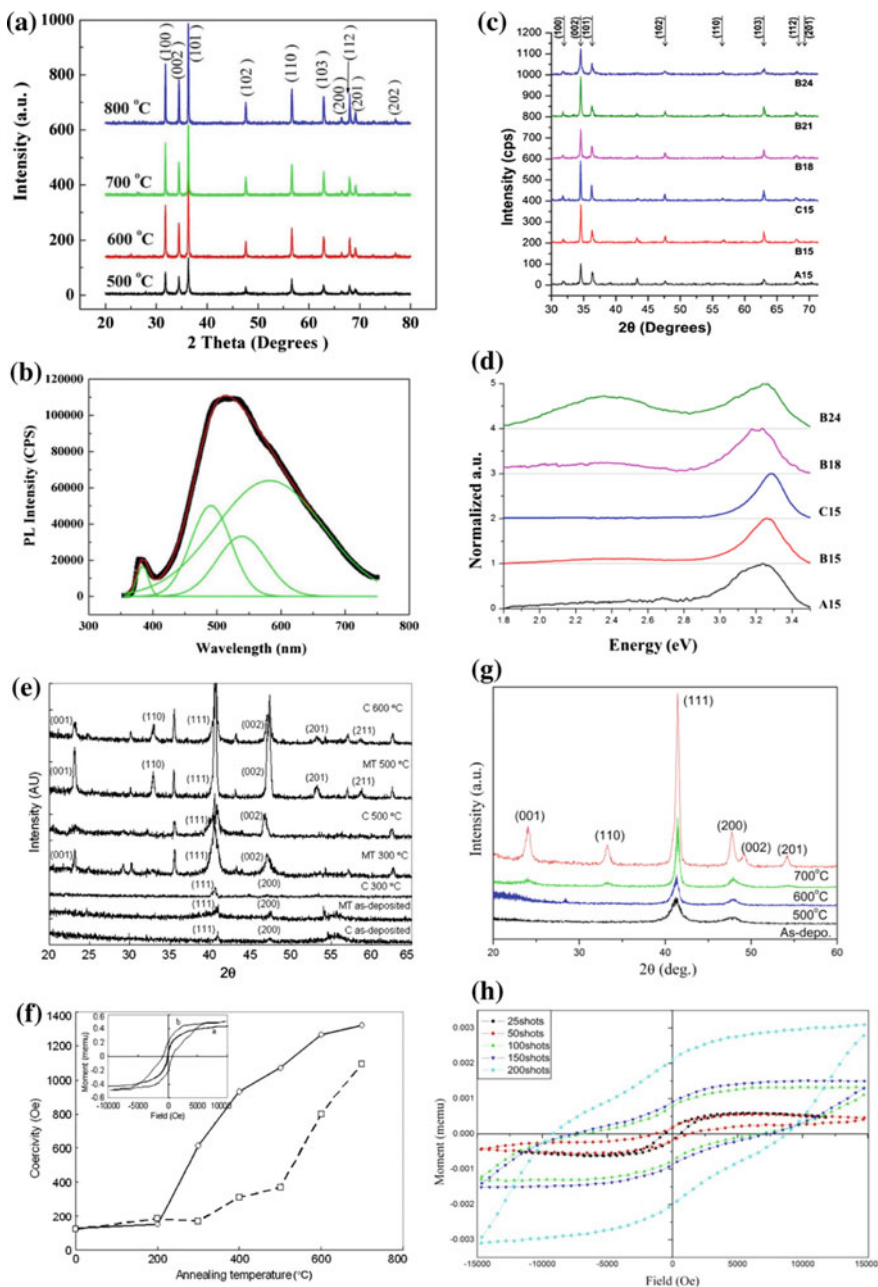


Fig. 2.30 XRD and PL spectra of PLD (a, b) and DPF (c, d) grown ZnO thin films. XRD and VSM results of PLD grown FePt:Al₂O₃ composite (e, f) and DPF grown CoPt thin films (g, h). Reprinted from a, b Ilyas et al. [166], Copyright (2011) with permission from AIP publishing; c, d Tan et al. [158], Copyright (2015), with permission from IEEE; e, f Lin et al. [172], Copyright (2008) with permission from IOP publishing; and g, h Pan et al. [146], Copyright (2009) with permission from IOP publishing

intrinsic defects with increasing number of focus deposition shots was caused by a greater amount of transient annealing of the deposited ZnO. This demonstrates superior structural properties (defect-free) exhibited by DPF grown ZnO films compared to PLD-grown films.

Another example that we would like to highlight is that of the magnetic thin film deposited by PLD [172] and DPF [146] and shown in Fig. 2.30e–h. The PLD grown, refer Fig. 2.30e, f, as-deposited FePt thin films were very weakly crystalline and soft magnetic in nature with a coercivity of about 100 Oe. With post-deposition annealing, the samples became hard magnetic with coercivity increasing gradually to a maximum of about 1300 Oe with increasing annealing temperature due to transition from face centered cubic (fcc) to face centered tetragonal (fct) phase. But one thing to notice in Fig. 2.30e is the presence of a large number of unidentified (non-labeled) XRD peaks which were associated with impurity phase formation which did not allow the formation of very hard magnetic phase [173]. It took lots of effort to eliminate the impurity phase formation in PLD grown thin films to be finally able to achieve very hard magnetic phase in FePt thin films with a coercivity of the order of 7.7 kOe. The CoPt thin films grown by DPF were having better crystallinity but still in chemically disordered fcc phase. The crystallinity improved significantly with annealing and converted to highly crystalline chemically ordered desired fct phase as seen in Fig. 2.30g. One of the most important facts to note is that no unidentified peaks were observed in XRD spectra of DPF grown CoPt thin films implying that no impurity phases were formed. This resulted in the very hard magnetic film for the sample deposited with 200 DPF shots with coercivity value approaching almost to 10 kOe, refer Fig. 2.30h [146]. Even the sample deposited with 100 and 150 shots were highly crystalline and depicted very hard magnetic phase with a coercivity of the order of 7–8 kOe. The reader may be questioning the comparison of DPF grown CoPt films with PLD grown FePt thin films, as they are different materials. Both materials have similar magnetic properties and phase transition temperature and that is the why the comparison is fair. Author's group has also deposited CoPt thin films using PLD and the results are discussed in paper by Pan et al. [174]. The PLD grown CoPt thin films were less crystalline compared to the DPF grown films, moreover the highest coercivity obtained was about 3.7 kOe, significantly lower than that of 10 kOe obtained for DPF grown CoPt films. This highlights the superior crystalline and magnetic properties obtained for DPF-grown films.

2.7.1.4 Versatile Deposition Facility with a Variety of Deposition Options

The versatility of DPF device as deposition facility is reflected through many types of depositions that have been achieved in many different investigations which include

- (i) use of DPF device as pure PVD or hybrid PVD-CVD or pure CVD type deposition facility as depicted in Fig. 2.15,
- (ii) the DPF device can be operated in different configurations, shown in Figs. 2.16, 2.17 and 2.18, to utilize its different components such as ions, electrons and hot dense plasma for material synthesis,
- (iii) ability to deposit a wide variety of materials that include metal, bi-metals, metal nitrides, metal oxides, metal carbide, metal oxy-nitrides, metal carbo-nitrides, and a large number of carbon-based materials, and
- (iv) ability to deposit nanoparticle (0-dim), nanowires (1-dim), flat thin films (2-dim) and vertical graphene (3-dim) materials.

2.7.2 *Understanding Mechanisms of Material Synthesis in DPF Device*

The mechanisms of material synthesis are different for different types of depositions that have been performed in DPF device. We have broadly classified these different mechanisms in three broad categories based on materials and morphology of the deposited materials.

Mechanism for deposition of metallic, bimetallic, and carbon thin films: The depositions of thin films of Fe, Cu, FeCo, CoPt, FePt, diamond-like carbon, etc., are primarily done in inert gases (neon or argon) or hydrogen as filling gas with central electrode replaced or fitted with relevant material (metal, bimetal, or graphite). The substrate on which deposition is done can be kept at different distances from solid anode top and/or angular positions with respect to anode axis to control the deposition rate and uniformity of the thin films. Most depositions are done using multiple DPF shots to achieve higher thickness and size of nanoparticles on the surface of the film. During each DPF deposition shot two different plasmas, one of filling gas species and the other one of plasma of anode top ablated material, are primarily created. The plasma of filling gas species (which in the present case is that of either inert or hydrogen gas) is created right from the initiation of discharge and its density and temperature reach the highest during the pinch phase. In addition to plasma of filling gas species, as mentioned earlier, energetic ions of filling gas species in the range of 10 keV to few MeV are also generated by instabilities and they are the one which would reach the substrate much before ablated plasma of anode top material. Actually, short ion pulses of high-energy-density can cause sputtering as well as very rapid heating of the substrate surface depending on the nature of the surface layer and the energy density (which depends on the distance and the angular position of the substrate) of the incident ions of filling gas species. This may cause the ablation/sputtering of the substrate forming the momentary substrate surface plasma at the substrate surface. This leads to the cleaning of the substrate surface before the deposition of desired thin film material, which may result in improved adhesion of the deposited films. At the same time, it may

introduce the undesirable impurities of substrate material in the deposited thin material. The problem of substrate material ablation can be avoided by increasing the distance of deposition to avoid its impurities in the film. This is followed by the arrival and deposition of anode top ablated material plasma over the much longer duration of several microseconds. Since all depositions performed in DPF devices are multiple shot deposition, during the next DPF shot the energetic ions of filling gas species will process the film deposited in previous shot leading to its densification and in situ intense transient annealing. This in situ transient annealing is the reason for most DPF depositions to directly go into a crystalline phase without the need of post-deposition annealing.

Mechanism for deposition of metal-nitride, -carbide, -oxide, etc., thin films: The mechanism of depositions of MX thin films (with M = metal and X = nitride/carbide/oxide) is slightly different as though the central electrode is fitted with relevant metal as before but the filling gas is reactive. The filling gas is either nitrogen or oxygen or carbon-containing gas such as methane or acetylene. For example, hard coating of TiN can be deposited using DPF fitted with Ti anode and by operating the DPF in nitrogen ambiance. High-pinch plasma temperature causes the complete ionization of the filling gas species (nitrogen) resulting formation of nitrogen ions, atoms, and molecules. The interaction of hot dense pinch plasma and instability generated backward moving relativistic electrons causes the ablation of Ti anode material forming the Ti plasma which then reacts with ambient nitrogen plasma resulting in TiN formation on the substrate placed down the anode axis. Once again, during the next shot, the material deposited in previous shot is transiently annealed by instability-accelerated energetic nitrogen ions leading to crystalline TiN phase. In addition to transient annealing, the energetic nitrogen ions exposure can also add on the TiN formation by implantation of nitrogen ions in the previously deposited TiN layer. Similarly, for TiC coating the Ti anode fitted DPF just needs to be operated with a gas containing carbon such as methane or acetylene. It has however been found that the DPF operation in these gases is non-reliable and inconsistent. It is for this reason these gas are normally used as an admixture with inert gases such as argon or neon. Thus, the deposition of thin films of carbides, nitrides or oxides of any metal can simply be achieved using suitable reactive background gases such nitrogen, acetylene, methane, and oxygen or their combinations.

Mechanism for deposition of carbon nanotube or graphene thin films: The mechanism presented here for the deposition of carbon nanotube (CNT) and graphene nanoflakes (GNF) in DPF device is based on the research findings presented by K.S. Tan in his Ph.D. thesis [84]. The successful growth of CNT required simultaneously the presence of three important parameters while GNF required only one important parameter for the successful synthesis in a DPF device. The first important parameter for CNT growth was the presence of heated substrate ($> 500^{\circ}\text{C}$) which provided the energy necessary for the enhancement of the dissolution of carbon into metal catalyst due to lowering of activation energy for CNT growth at the heated substrate. The assistance of the DPF discharge plasma is the second important parameter which enhances/substitutes the role of thermal decomposition.

Although it is well known that carbon dissolution into Fe results in formation of iron carbide above 500 °C, what explains the absence of carbon nanotube growth is due to the lack of iron carbide converting into a α -Fe phase which is an active graphite precipitation phase. This phase increases the production of CNT rapidly and begins to form between 500 and 750 °C while stabilizing at the temperature above 750 °C through exothermic precipitation. Even without the assistance of a heat source the carbon nano-structures such as graphene nanoflakes were formed without thermal decomposition of carbon feedstock as the presence of active carbon species was sufficiently made available via energetic DPF discharge plasma decomposition for the growth of this material. Thus, the results hint that GNF synthesis does not require catalytic decomposition but the presence of a catalyst improves the synthesis outcome towards graphene-like nano-structures. Additionally, the formation of highly dense carbonaceous plasma was more than sufficient for GNF synthesis. However, the CNT growth without the presence of a catalyst was not possible. In other words, the presence of catalyst plays as the third important factor/parameter which provided a low-activation energy pathway for the successful low-temperature plasma-assisted growth of CNT. The transient effect of the dense plasma focus forms the α -Fe phase nanoparticles on the irradiated Fe-coated silicon substrate, providing active catalytic carbon nucleation sites of a right size allowing the growth of CNT on the catalyst substrate.

2.8 Scalability of DPF Devices for Material Processing and Synthesis

One of the major issues that DPF device faces as processing and deposition facility is its suitability as reliable and possibly a potential research/industrial facility is the scalability of the device for large area and uniform processing/deposition. In order to understand how scalability of DPF device can be achieved we need to understand the basic characteristics/features of DPF device and its pinch plasma. Electrically, the DPF device is an inductive load connected to a capacitor bank C_0 . The total inductance of the DPF device during its operation is the sum of fixed system inductance L_0 (comprising of the inductances of the capacitor bank, fast switches, transmission line, and input flanges) and the variable plasma inductance L_p due to plasma dynamics in axial and radial phase. The bulk of the DPF inductance is due to L_0 and is used to define the quarter time period $T/4 = \pi\sqrt{L_0C_0}/2$ of the discharge current in DPF device, the time instant at which the discharge current reaches the maximum. For most efficient magnetic compression and resistive Joule heating of the pinch plasma column the radial compression phase is required to occur at or near maximum discharge current (at about $\sim T/4$). As mentioned in Sect. 2.4.3 the typical current sheath speed in axial phase for maximum compression efficiency is in a limited range of about few cm/ μ s which together with the requirement of achieving the radial compression near or at the quarter time period

of the discharge current for maximum current to flow through pinch plasma, controls the dimension of the central electrode (anode). Therefore most plasma focus devices are designed using anode with lengths, which is approximately equal to the multiplication of the typical average value of axial current sheath speed (say 5 cm/ μ s) by the quarter time period of the short-circuit discharge current.

The anode radius is another crucial parameter which is decided on the basis of speed parameter value defined by Lee and Serban [66]. Most of the neutron optimized plasma focus devices have been found to have the typical speed factor, $I_0/a\sqrt{P}$, value of about 90 kA cm⁻¹ Torr^{-1/2} where I_0 , a and P denote the short-circuit peak discharge current in kA, anode radius in cm and deuterium filling gas pressure in Torr, respectively. Using the short-circuit peak discharge current and approximate deuterium operating pressure of say 5 Torr, one can estimate the approximate anode radius. The peak short-circuit discharge current for a given charging voltage of V_0 depends on the capacitance of the capacitor bank as $I_0 = V_0/\sqrt{L_0/C_0}$. In other words, the dimensions (length and radius) of the anode of DPF devices are different for devices of difference capacitor bank (storage energy). The higher the capacitance of the capacitor bank the bigger is the dimension (length as well as the radius) of the anode. According to the established scaling laws [66] and performed optical investigations [175], the final pinch radius and the maximum pinch length are proportional to anode radius a ($\sim 0.12a$ and $\sim 0.8a$, respectively). Thus, the final plasma volume V_p is of the order of $\pi(0.12a^2) \times (0.8a) \approx 0.036a^3$. Another important parameter is the time duration of various transient phenomena in DPF devices. For example, the pulse duration of energetic ion beam, which is one of the main component that is responsible for energetic processing of material placed down the anode stream, depends on pinch phase duration of plasma focus device which in turn depends on the characteristic time ($\sim \sqrt{L_0C_0}$) of the device. In low- and mid-energy DPF devices, the duration of energetic ion beam is of the order of several tens to about hundreds of ns while in bigger plasma focus device it might be several hundred ns.

It can, therefore, be concluded that DPF devices with larger storage energy use larger capacitance and hence also have a larger quarter time period and the large dimensions of the coaxial electrode assembly leading to the larger volume of the dense hot plasma and that too for longer durations. Hence, the increase in anode radius a from about 1 cm in 3 kJ UNU-ICTP DPF device to about 11.5 cm in 1 MJ PF1000 device not only increases the final-pinch plasma volume by 1000 times but the hot dense plasma and other associated phenomena are also of significantly long durations. So even though increasing the storage energy and correspondingly the physical dimensions of electrode assembly do not increase the temperature and the density of the pinch plasmas, providing the unique universality in the basic nature of the DPF devices, but the increase in final pinch plasma volume and time durations of all associated transient phenomena leads to the increase in yields of energetic charged particles and radiations which points to the scalability of the DPF device. The large volume of pinch plasma will allow a large area of uniform deposition with even high deposition rate, which makes the DPF facility scalable.

However, making DPF devices with larger bank energy and electrode dimensions will come at increased cost and lower repetition rate operation. For example, the hugely expensive 1 MJ PF1000 device is operated on an average of 1 shot per 20 min, whereas low-cost kJ range UNU-ICTP device can be operated twice in 1 min.

Another solution to improve the scalability, large area uniform deposition/processing, of the DPF device is to increase the distance of deposition from the anode top. This normally results in significant reduction in deposition rate but the uniformity of films improves significantly. It may also be pointed out that now high repetition rate DPF devices are available, operating at 1–50 Hz. This in principle allows the repetitive DPF device to be used just like repetitive PLD (pulsed laser deposition) facility where the uniformity of deposited material can be achieved by rotating the substrate.

2.9 Conclusions

The major aim of this chapter was to establish that the DPF device based high-energy-density pulsed plasma facility has enormous potential for controlled material processing and synthesis for a wide range of material types in wide range nano-structural features ranging from zero-dimensional nanoparticles to three-dimensional graphene nanoflowers. The versatility of DPF-based deposition was established by demonstrating that how over the years the depositions have evolved from pure PVD type to hybrid PVD-CVD to purely CVD type depositions. The processing and synthesis of nanoscale materials in DPF have been successfully performed by many different research groups across the globe using both “top-down” and “bottom-up” approaches. In “top-down” approach, which relies on the successive fragmentations or processing of macro-scale materials to smaller nano-sized objects, the bulk and thin film samples were exposed to different numbers of DPF shots at different distances from the anode top. It was found that while the nano-structurization and property modification of the entire thickness of the thin film can be achieved by its exposure to DPF shots but for bulk material, only the top surface layer of the bulk sample is processed and nano-structurized by its exposure to DPF shots. In “bottom-up” approach, which relies on nanoscale materials being assembled atoms and molecules, several thin film deposition configurations, in term of target-substrate orientation and placement, use of different ablative components, and pure gas-based synthesis have been used in DPF devices for nano-structured material syntheses. The DPF device has the enormous flexibility of being operated in many different possible configurations whereby its different components such as ions, electrons, and hot dense plasma can be used for material synthesis or processing. Each of the DPF-based deposition configurations has its own limitations and disadvantages but based on our extensive experience and survey of results from different groups, we conclude that most versatile and efficient for thin film deposition setup is where the target material (to be ablated) is used

either as anode insert or as anode tip with background inert/reactive gas is used in the DPF chamber and the substrate (on which thin film is deposited) is placed downstream either along or at some angle with respect to the anode axis. This setup allows deposition of nano-structured metallic, bimetallic, carbide, nitride, oxide, and composite thin films. Using the hollow anode, a pure gas-based synthesis of carbon nanotube has also been successfully demonstrated which extends the application domain of DPF device to PECVD (plasma-enhanced CVD). This opens a very wide area of application of DPF facility for other pure gas-based depositions though limitations and issues need to be explored in greater details. The DPF device has also been used successfully for the synthesis of zero-, one-, two- and three-dimensional nano-structures proving its immense potential in plasma nanoscience and nanotechnology. In addition, the device has the added advantage of high deposition rates, the ability to grow crystalline thin films directly at room temperature without any need for post-deposition annealing (though through post-deposition annealing material properties can be tuned additionally), and other superior physical properties in deposited materials. The DPF device offers a complex mixture of high-energy ions of the filling gas species, immensely hot and dense decaying plasma, fast-moving ionization wavefront and a strong shockwave that provides a unique plasma and physical/chemical environment that is completely unheard of in any other conventional plasma-based deposition or processing facility making it a novel and versatile facility with immense potential for high-energy-density pulsed plasma-based material processing and depositions.

References

1. ITER. *Phases Ahead*. <https://www.iter.org/construction/timeline> (2017)
2. NIF. *Ignition Experiments at NIF*. <https://lasers.llnl.gov/science/ignition/ignition-experiments> (2017)
3. K.L. Choy, Chemical vapour deposition of coatings. *Prog. Mater. Sci.* **48**, 57–170 (2003). doi:[10.1016/s0079-6425\(01\)00009-3](https://doi.org/10.1016/s0079-6425(01)00009-3)
4. J.E. Mahan, *Phys. Vapor Deposition Thin Films*. (Wiley, USA, 2000)
5. S.S. Meysami, A.A. Koos, F. Dillon, M. Dutta, N. Grobert, Aerosol-assisted chemical vapour deposition synthesis of multi-wall carbon nanotubes: III. Towards upscaling. *Carbon* **88**, 148–156 (2015). doi:[10.1016/j.carbon.2015.02.045](https://doi.org/10.1016/j.carbon.2015.02.045)
6. G. Papadimitropoulos, D. Davazoglou, Copper films deposited by hot-wire CVD and direct liquid injection of CupraSelect. *Chem. Vap. Deposition* **13**, 656–662 (2007). doi:[10.1002/cvde.200706621](https://doi.org/10.1002/cvde.200706621)
7. S.G. Ansari et al., Effect of RF plasma power and deposition temperature on the surface properties of tin oxide deposited by modified plasma enhanced chemical vapor deposition. *Sci. Adv. Mat.* **1**, 254–261 (2009). doi:[10.1166/sam.2009.1052](https://doi.org/10.1166/sam.2009.1052)
8. G.L. Doll, B.A. Mensah, H. Mohseni, T.W. Scharf, Chemical vapor deposition and atomic layer deposition of coatings for mechanical applications. *J. Therm. Spray Technol.* **19**, 510–516 (2010). doi:[10.1007/s11666-009-9364-8](https://doi.org/10.1007/s11666-009-9364-8)
9. S.A. Amer, S. Magnaudeix, P. Duverneuil, On the behavior of rapid thermal cvd reactors. *J. Phys. IV* **3**, 35–42 (1993). doi:[10.1051/jp4:1993304](https://doi.org/10.1051/jp4:1993304)

10. I. Zunke et al., Conductive zinc oxide thin film coatings by combustion chemical vapour deposition at atmospheric pressure. *Thin Solid Films* **532**, 50–55 (2013). doi:[10.1016/j.tsf.2012.11.151](https://doi.org/10.1016/j.tsf.2012.11.151)
11. Y.Z. Wang, et al., MgB₂ superconducting whiskers synthesized by using the hybrid physical-chemical vapor deposition. *J. Am. Chem. Soc.* **131**, 2436–2437, doi:[10.1021/ja8087828](https://doi.org/10.1021/ja8087828) (2009)
12. A. Anders, *Cathodic Arcs: From Fractal Spots to Energetic Condensation*. (Springer, Berlin, 2008)
13. Harsha, K. S. S. *Principles of Physical Vapor Deposition of Thin Films*. (Elsevier, Netherlands, 2006)
14. F.F. Chen, *Introduction to Plasma Physics and Controlled Fusion*. (Springer, Berlin, 1984)
15. A. Fridman, *Plasma Chemistry*. (Cambridge University Press, UK, 2008)
16. Panel on Plasma Processing of Materials, National Research Council (US), *Plasma processing of materials: Scientific opportunities and technological challenges*. 88 (National Academy Press (US), 1991)
17. Committee on High Energy Density Plasma Physics, P. S. C., *National Research Council Frontiers in High Energy Density Physics: The X-Games of Contemporary Science*. (National Academies Press, USA, 2003)
18. Laboratory for Laser Energetics. http://www.lle.rochester.edu/omega_facility/omega/
19. Sandia National Laboratories. <http://www.sandia.gov/z-machine/>
20. L. Soto, New trends and future perspectives on plasma focus research. *Plasma Phys. Controlled Fusion* **47**, A361–A381 (2005). doi:[10.1088/0741-3335/47/5a/027](https://doi.org/10.1088/0741-3335/47/5a/027)
21. I.E. Garkusha et al., Experimental study of plasma energy transfer and material erosion under ELM-like heat loads. *J. Nucl. Mater.* **390–91**, 814–817 (2009). doi:[10.1016/j.jnucmat.2009.01.215](https://doi.org/10.1016/j.jnucmat.2009.01.215)
22. V.A. Makhraj, I.E. Garkusha, N.N. Aksenov, O.V. Byrka, I. Landman, S.I. Lebedev, P.B. Shevchuk, Plasma-surface interaction and mechanisms of dust production in ITER ELM simulation experiments with QSPA Kh-50. *Prob Atomic Sci Technol*, # 6, Ser “Plasma Phys” **18**, 55–57 (2012)
23. S.V. Bazdyreva, I.E. Garkusha, V.A. Makhraj, S.V. Malykhin, S.V., A.T. Pugachov, The influence of irradiation by hydrogen plasma on the structure and phase composition of Ti-Zr-Ni alloys containing quasicrystalline Phase. *Prob Atomic Sci Technol*, # 6, Ser “Plasma Phys” **18**, 226–228 (2012)
24. W.R. Feng, H. Zhou, S.Z. Yang, Gas pressure dependence of composition in Ta-Ti-N films prepared by pulsed high energy density plasma. *Mater. Chem. Phys.* **124**, 287–290 (2010). doi:[10.1016/j.matchemphys.2010.06.033](https://doi.org/10.1016/j.matchemphys.2010.06.033)
25. W.R. Feng et al., Characteristics of (Ti, Ta)N thin films prepared by using pulsed high energy density plasma. *J. Phys. D-Appl. Phys.* **40**, 4228–4233 (2007). doi:[10.1088/0022-3727/40/14/018](https://doi.org/10.1088/0022-3727/40/14/018)
26. W.R. Feng et al., Preparation of Ta(C)N films by pulsed high energy density plasma. *J. Phys. D-Appl. Phys.* **40**, 2132–2137 (2007). doi:[10.1088/0022-3727/40/7/041](https://doi.org/10.1088/0022-3727/40/7/041)
27. W.R. Feng et al., Titanium carbonitride films on cemented carbide cutting tool prepared by pulsed high energy density plasma. *Appl. Surf. Sci.* **253**, 4923–4927 (2007). doi:[10.1016/j.apsusc.2006.10.069](https://doi.org/10.1016/j.apsusc.2006.10.069)
28. D. Wu et al., Numerical study of dynamic effects and evaporation of target material under irradiation of intense pulsed ion beam. *Acta Physica Sinica* **55**, 3501–3505 (2006)
29. H.Z. Miao et al., Nanometer grain titanium carbonitride coatings with continuously graded interface onto silicon nitride cutting tools by pulsed high energy density plasma. *Mat Sci Eng A-Struct Mat Prop Microstruct Process* **384**, 202–208 (2004). doi:[10.1016/j.msea.2004.06.005](https://doi.org/10.1016/j.msea.2004.06.005)
30. Z.J. Peng, H.Z. Miao, L.H. Qi, S. Yang, C.Z. Liu, Hard and wear-resistant titanium nitride coatings for cemented carbide cutting tools by pulsed high energy density plasma. *Acta Mater.* **51**, 3085–3094 (2003). doi:[10.1016/s1359-6454\(03\)00119-8](https://doi.org/10.1016/s1359-6454(03)00119-8)

31. C. Rong, J.Z. Zhang, C.Z. Liu, S.Z. Yang, Surface metallization of alumina ceramics by pulsed high energy density plasma process. *Appl. Surf. Sci.* **200**, 104–110 (2002). doi:[10.1016/s0169-4332\(02\)00874-7](https://doi.org/10.1016/s0169-4332(02)00874-7)
32. B. Liu et al., Investigation of titanium coating on Si₃N₄ by using a pulsed high energy density plasma (PHEDP) gun. *Mater. Chem. Phys.* **57**, 219–223 (1999). doi:[10.1016/s0254-0584\(98\)00219-3](https://doi.org/10.1016/s0254-0584(98)00219-3)
33. B. Liu, C.Z. Liu, D.J. Cheng, R. He, S.Z. Yang, Pulsed high energy density plasma processing silicon surface. *Thin Solid Films* **390**, 149–153 (2001). doi:[10.1016/s0040-6090\(01\)00927-0](https://doi.org/10.1016/s0040-6090(01)00927-0)
34. S. Lee et al., A simple facility for the teaching of plasma dynamics and plasma nuclear fusion. *Am. J. Phys.* **56**, 62 (1988)
35. J.O. Pouzo, M.M. Milanese, Applications of the dense plasma focus to nuclear fusion and plasma astrophysics. *IEEE Trans. Plasma Sci.* **31**, 1237–1242 (2003). doi:[10.1109/tps.2003.821475](https://doi.org/10.1109/tps.2003.821475)
36. J.W. Mather, Formation of a high-density deuterium plasma focus. *Phys. Fluids* **8**, 366–377 (1965). doi:[10.1063/1.1761231](https://doi.org/10.1063/1.1761231)
37. N.V. Filipov, T.I. Filipova, V.P. Vinogradov, *Nuclear Fusion* **2**, 577 (1962)
38. J.N. Feugeas, The influence of the insulator surface in the plasma focus behavior. *J. Appl. Phys.* **66**, 3467–3471 (1989). doi:[10.1063/1.344102](https://doi.org/10.1063/1.344102)
39. V.A. Gribkov, A. Srivastava, P.L.C. Keat, V. Kudryashov, S. Lee, Operation of NX2 dense plasma focus device with argon filling as a possible radiation source for micro-machining. *IEEE Trans. Plasma Sci.* **30**, 1331–1338 (2002). doi:[10.1109/tps.2002.802156](https://doi.org/10.1109/tps.2002.802156)
40. R. Verma et al., Neutron emission characteristics of NX-3 plasma focus device: speed factor as the guiding rule for yield optimization. *IEEE Trans. Plasma Sci.* **40**, 3280–3289 (2012). doi:[10.1109/tps.2012.2220569](https://doi.org/10.1109/tps.2012.2220569)
41. A. Talebitaher et al., Laser Shadowgraphic study of the influence of krypton-seeding, switch synchronization and electrode geometry on plasma dynamic in plasma focus device. *J. Fusion Energy* **34**, 794–801 (2015). doi:[10.1007/s10894-015-9888-5](https://doi.org/10.1007/s10894-015-9888-5)
42. A. Gribkov et al., Pseudosparks in the nanosecond range of operation: firing, jitter, and current disruption. *J. Phys. D-Appl. Phys.* **37**, 2107–2111 (2004). doi:[10.1088/0022-3727/37/15/009](https://doi.org/10.1088/0022-3727/37/15/009)
43. R. Verma, et al., Compact sub-kilojoule range fast miniature plasma focus as portable neutron source. *Plasma Sources Sci. Technol.* **17**, 045020, doi:[10.1088/0963-0252/17/4/045020](https://doi.org/10.1088/0963-0252/17/4/045020) (2008)
44. E. Gharehabani, R.S. Rawat, R. Verma, S. Karamat, S. Sobhanian, Low energy repetitive miniature plasma focus device as high deposition rate facility for synthesis of DLC thin films. *Appl. Surf. Sci.* **256**, 4977–4983 (2010). doi:[10.1016/j.apsusc.2010.03.012](https://doi.org/10.1016/j.apsusc.2010.03.012)
45. R. Verma, R.S. Rawat, P. Lee, S.V. Springham, T.L. Tan, High performance high repetition rate miniature plasma focus device: record time averaged neutron yield at 200 J with enhanced reproducibility. *J. Fusion Energy* **32**, 2–10 (2013). doi:[10.1007/s10894-012-9517-5](https://doi.org/10.1007/s10894-012-9517-5)
46. J.M. Koutsoubis, S.J. MacGregor, Electrode erosion and lifetime performance of a high repetition rate, triggered, corona-stabilized switch in air. *J. Phys. D-Appl. Phys.* **33**, 1093–1103 (2000). doi:[10.1088/0022-3727/33/9/309](https://doi.org/10.1088/0022-3727/33/9/309)
47. F.N. Beg, M. Zakaullah, G. Murtaza, M.M. Beg, Effect of insulator sleeve material on neutron emission from a plasma-focus. *Phys. Sci.* **46**, 152–154 (1992). doi:[10.1088/0031-8949/46/2/008](https://doi.org/10.1088/0031-8949/46/2/008)
48. S.M. Hassan et al., Pinching evidences in a miniature plasma focus with fast pseudospark switch. *Plasma Sources Sci. Technol.* **15**, 614–619 (2006). doi:[10.1088/0963-0252/15/4/004](https://doi.org/10.1088/0963-0252/15/4/004)
49. T. Zhang et al., Current sheath curvature correlation with the neon soft x-ray emission from plasma focus device. *Plasma Sources Sci. Technol.* **14**, 368–374 (2005). doi:[10.1088/0963-0252/14/2/020](https://doi.org/10.1088/0963-0252/14/2/020)
50. J.W. Mather, P.J. Bottoms, Characteristics of the dense plasma focus discharge. *Phys. Fluids* **11**, 611–618 (1968)

51. S. Al-Hawat, Axial velocity measurement of current sheath in a plasma focus device using a magnetic probe. *IEEE Trans. Plasma Sci.* **32**, 764–769 (2004)
52. A.J. Toepfer, D.R. Smith, E.H. Beckner, Ion heating in the dense plasma focus. *Phys. Fluids* **14**, 52–61 (1971)
53. V.A. Gribkov et al., Plasma dynamics in the PF-1000 device under full-scale energy storage: II. Fast electron and ion characteristics versus neutron emission parameters and gun optimization perspectives. *J. Phys. D Appl. Phys.* **40**, 3592–3607 (2007). doi:[10.1088/0022-3727/40/12/008](https://doi.org/10.1088/0022-3727/40/12/008)
54. A. Bernard, A. Coudeville, A. Jolas, J. Launspach, J.D. Mascureau, Experimental studies of plasma focus and evidence for non-thermal processes. *Phys. Fluids* **18**, 180–194 (1975). doi:[10.1063/1.861101](https://doi.org/10.1063/1.861101)
55. M. Martínez-Fuentes, et al., Dynamics of the expansion discharge originated by a dense plasma focus. *J. Phys.: Conf. Ser.* **370**, doi:[10.1088/1742-6596/370/1/012059](https://doi.org/10.1088/1742-6596/370/1/012059) (2012)
56. E. Skladnik-Sadowska, et al., 365–368
57. J. Tendys (ed) (Lucas Heights Research Establishment, Sydney, Australia) (1976)
58. A. Bernard et al., Dense plasma focus—high intensity neutron source. *Nuclear Instrum. Methods* **145**, 191–218 (1977). doi:[10.1016/0029-554x\(77\)90569-9](https://doi.org/10.1016/0029-554x(77)90569-9)
59. V.A. Gribkov, in *Plasma and Fusion Science*, vol. 996, ed. by C. Varandas, C. Silva. Aip Conference Proceedings, pp. 51–64 (2008)
60. M. Krishnan, The dense plasma focus: a versatile dense pinch for diverse applications. *IEEE Trans. Plasma Sci.* **40**, 3189–3221 (2012). doi:[10.1109/tps.2012.2222676](https://doi.org/10.1109/tps.2012.2222676)
61. R.S. Rawat, High-energy-density pinch plasma: a unique nonconventional tool for plasma nanotechnology. *IEEE Trans. Plasma Sci.* **41**, 701–715 (2013). doi:[10.1109/tps.2012.2228009](https://doi.org/10.1109/tps.2012.2228009)
62. S. Lee, S.H. Saw, P. Lee, R.S. Rawat, Numerical experiments on plasma focus neon soft x-ray scaling. *Plasma Phys. Contrroll Fusion* **51**, 105013, doi:[10.1088/0741-3335/51/10/105013](https://doi.org/10.1088/0741-3335/51/10/105013) (2009)
63. H. Krompholz, F. Ruhl, W. Schneider, K. Schonbach, G. Herziger, A scaling law for plasma-focus devices. *Phys. Lett. A* **82**, 82–84 (1981). doi:[10.1016/0375-9601\(81\)90944-0](https://doi.org/10.1016/0375-9601(81)90944-0)
64. A.J. Toepfer, D.R. Smith, E.H. Beckner, Ion heating in dense plasma focus. *Bull. Am. Phys. Soc.* **14**, 1013 (1969)
65. R.S. Rawat et al., Effect of insulator sleeve length on soft x-ray emission from a neon-filled plasma focus device. *Plasma Sources Sci. Technol.* **13**, 569–575 (2004)
66. S. Lee, A. Serban, Dimensions and lifetime of the plasma focus pinch. *IEEE Trans. Plasma Sci.* **24**, 1101–1105 (1996)
67. N. Qi, S.F. Fulghum, R.R. Prasad, M. Krishnan, Space and time resolved electron density and current measurements in a dense plasma focus z-pinch. *IEEE Trans. Plasma Sci.* **26**, 1127–1137 (1998)
68. T. Zhang et al., Optimization of a plasma focus device as an electron beam source for thin film deposition. *Plasma Sources Sci. Technol.* **16**, 250–256 (2007). doi:[10.1088/0963-0252/16/2/006](https://doi.org/10.1088/0963-0252/16/2/006)
69. P. Choi, C. Deeney, H. Herold, C.S. Wong, Characterization of self-generated intense electron beams in a plasma focus. *Laser Part. Beams* **8**, 469–476 (1990)
70. H. Bhuyan, S.R. Mohanty, T.K. Borthakur, R.S. Rawat, Analysis of nitrogen ion beam produced in dense plasma focus device using Faraday Cup. *Indian J. Pure Appl. Phys.* **39**, 698–703 (2001)
71. M.V. Roshan, S. Springham, A. Talebitaher, R.S. Rawat, P. Lee, Magnetic spectrometry of high energy deuteron beams from pulsed plasma system. *Plasma Phys. Controlled Fusion* **52**, 085007, doi:[10.1088/0741-3335/52/8/085007](https://doi.org/10.1088/0741-3335/52/8/085007) (2010)
72. V. Raspa et al., Plasma focus as a powerful hard x-ray source for ultrafast imaging of moving metallic objects. *Braz. J. Phys.* **34**, 1696–1699 (2004)
73. M. Zakaullah et al., Characteristics of x-rays from a plasma focus operated with neon gas. *Plasma Sources Sci. Technol.* **11**, 377–382 (2002)

74. H. Bhuyan, S.R. Mohanty, N.K. Neog, S. Bujarbarua, R.K. Rout, Comparative study of soft x-ray emission characteristics in a low energy dense plasma focus device. *J. Appl. Phys.* **95**, 2975–2981 (2004). doi:[10.1063/1.1647269](https://doi.org/10.1063/1.1647269)
75. M. Barbaglia, H. Bruzzone, H. Acuna, L. Soto, A. Clausse, Experimental study of the hard x-ray emissions in a plasma focus of hundreds of Joules. *Plasma Phys. Controlled Fusion* **51**, 045001, doi:[10.1088/0741-3335/51/4/045001](https://doi.org/10.1088/0741-3335/51/4/045001) (2009)
76. T. Zhang, *Electron emission from plasma focus for nano phase FeCo thin film deposition*, PhD thesis, Nanyang Technological University, (2007)
77. L.Y. Soh, P. Lee, X. Shuyan, S. Lee, R.S. Rawat, Shadowgraphic studies of DLC film deposition process in dense plasma focus device. *IEEE Trans. Plasma Sci.* **32**, 448–455 (2004). doi:[10.1109/tps.2004.826031](https://doi.org/10.1109/tps.2004.826031)
78. A. Patran et al., Spectral study of the electron beam emitted from a 3 kJ plasma focus. *Plasma Sources Sci. Technol.* **14**, 549–560 (2005). doi:[10.1088/0963-0252/14/3/018](https://doi.org/10.1088/0963-0252/14/3/018)
79. J.N. Feugeas, E.C. Llonch, C.O. De González, G. Galambos, Nitrogen implantation of AISI 304 stainless steel with a coaxial plasma gun. *J. Appl. Phys.* **64**, 2648–2651 (1988). doi:[10.1063/1.341604](https://doi.org/10.1063/1.341604)
80. R.S. Rawat, M.P. Srivastava, S. Tandon, A. Mansingh, Crystallization of an amorphous lead zirconate titanate thin film with a dense-plasma-focus device. *Phys. Rev. B* **47**, 4858–4862 (1993). doi:[10.1103/PhysRevB.47.4858](https://doi.org/10.1103/PhysRevB.47.4858)
81. C.R. Kant, M.P. Srivastava, R.S. Rawat, Thin carbon film deposition using energetic ions of a dense plasma focus. *Phys. Lett. Sect A: General, At. Solid State Phys.* **226**, 212–216 (1997)
82. R.S. Rawat, P. Lee, T. White, L. Ying, S. Lee, Room temperature deposition of titanium carbide thin films using dense plasma focus device. *Surf. Coat. Technol.* **138**, 159–165 (2001)
83. K.S. Tan, *High Growth Rate Synthesis of Zinc Oxide and Carbon Based Nanostructured Materials Using Dense Plasma Focus Device* PhD thesis, Nanyang Technological University (2017)
84. K.S. Tan, B. Ouyang, R.S. Rawat, in *10th Asian-European International Conference on Plasma Surface Engineering (AEPSE2015)* (Jeju, Republic of Korea, 2015)
85. S. Zeb, M. Sadiq, A. Qayyum, G. Murtaza, M. Zakaullah, Deposition of diamond-like carbon film using dense plasma focus. *Mater. Chem. Phys.* **103**, 235–240 (2007)
86. S.R. Mohanty et al., Self-organized transformation to polyaniline nanowires by pulsed energetic electron irradiation in a plasma focus device. *Phys. Lett. A* **373**, 1962–1966 (2009). doi:[10.1016/j.physleta.2009.03.062](https://doi.org/10.1016/j.physleta.2009.03.062)
87. V.N. Pimenov et al., Damage and modification of materials produced by pulsed ion and plasma streams in dense plasma focus device. *Nukleonika* **53**, 111–121 (2008)
88. N.D. Nawi, R. Farma, S.T. Ong, K.T. Chaudhary, J. Ali, Saktioto, Numerical studies on pinching radius effects to current densities of NX2 Plasma Focus. *KnE Engineering* **2016**, 6, doi:[10.18502/keg.v1i1.515](https://doi.org/10.18502/keg.v1i1.515) (2016)
89. S. Lee et al., Effect of targets on plasma focus dynamics. *IEEE Trans. Plasma Sci.* **18**, 1028–1032 (1990)
90. V.A. Gribkov, Physical processes taking place in dense plasma focus devices at the interaction of hot plasma and fast ion streams with materials under test. *Plasma Physics and Controlled Fusion* **57**, doi:[10.1088/0741-3335/57/6/065010](https://doi.org/10.1088/0741-3335/57/6/065010) (2015)
91. S. Lee, S.H. Saw, Plasma focus ion beam fluence and flux-Scaling with stored energy. *Physics of Plasmas* **19**, doi:[10.1063/1.4766744](https://doi.org/10.1063/1.4766744) (2012)
92. S. Lee, S.H. Saw, Plasma focus ion beam fluence and flux-For various gases. *Physics of Plasmas* **20**, doi:[10.1063/1.4811650](https://doi.org/10.1063/1.4811650) (2013)
93. M.S. Rafique, P. Lee, A. Patran, R.S. Rawat, S. Lee, Radiation emission correlated with the evolution of current sheath from a deuterium plasma focus. *J. Fusion Energy* **29**, 295–304 (2010). doi:[10.1007/s10894-010-9276-0](https://doi.org/10.1007/s10894-010-9276-0)
94. J.F. Ziegler, *SRIM—The Stopping and Range of Ions in Matter*. <http://www.srim.org/>

95. G. Sanchez, J. Feugeas, The thermal evolution of targets under plasma focus pulsed ion implantation. *J. Phys. D-Appl. Phys.* **30**, 927–936 (1997)
96. M.V. Roshan, et al. Backward high energy ion beams from plasma focus. *Phys. Plasmas* **16**, 074506, doi:[10.1063/1.3183715](https://doi.org/10.1063/1.3183715) (2009)
97. A. Patran et al., A magnetic electron analyzer for plasma focus electron energy distribution studies. *J. Fusion Energy* **25**, 57–66 (2006). doi:[10.1007/s10894-006-9005-x](https://doi.org/10.1007/s10894-006-9005-x)
98. R. Gupta, M.P. Srivastava, Carbon ion implantation on titanium for TiC formation using a dense plasma focus device. *Plasma Sources Sci. Technol.* **13**, 371–374 (2004). doi:[10.1088/0963-0252/13/3/002](https://doi.org/10.1088/0963-0252/13/3/002)
99. M. Hassan, A. Qayyum, R. Ahmad, G. Murtaza, M. Zakaullah, Nitriding of titanium by using an ion beam delivered by a plasma focus. *J. Phys. D-Appl. Phys.* **40**, 769–777 (2007). doi:[10.1088/0022-3727/40/3/013](https://doi.org/10.1088/0022-3727/40/3/013)
100. M. Hassan et al., Synthesis of nanocrystalline multiphase titanium oxycarbide (TiC_xO_y) thin films by UNU/ICTP and NX2 plasma focus devices. *Appl. Phys. A-Mat. Sci. Process.* **90**, 669–677 (2008). doi:[10.1007/s00339-007-4335-8](https://doi.org/10.1007/s00339-007-4335-8)
101. M. Hassan et al., Dense plasma focus ion-based titanium nitride coating on titanium. *Nucl. Instrum. Methods Phys. Res. Sect. B-Beam Interact. Mat. Atoms* **267**, 1911–1917 (2009). doi:[10.1016/j.nimb.2009.03.102](https://doi.org/10.1016/j.nimb.2009.03.102)
102. H. Bhuyan, et al., High energy ion beam irradiation on titanium substrate in a pulsed plasma device operating with methane. *J. Phys. D-Appl. Phys.* **42**, 205207, doi:[10.1088/0022-3727/42/20/205207](https://doi.org/10.1088/0022-3727/42/20/205207) (2009)
103. M. Valipour, M.A. Mohammadi, S. Sobhanian, R.S. Rawat, Increasing of hardness of titanium using energetic nitrogen ions from sahand as a filippov type plasma focus facility. *J. Fusion Energy* **31**, 65–72 (2012). doi:[10.1007/s10894-011-9432-1](https://doi.org/10.1007/s10894-011-9432-1)
104. V.A. Gribkov et al., Interaction of high temperature deuterium plasma streams and fast ion beams with stainless steels in dense plasma focus device. *J. Phys. D-Appl. Phys.* **36**, 1817–1825 (2003)
105. M. Shafiq et al., Dense plasma focus-assisted nitriding of AISI-304. *Radiat. Eff. Defects Solids* **163**, 729–736 (2008). doi:[10.1080/10420150701365664](https://doi.org/10.1080/10420150701365664)
106. J. Feugeas et al., Austenite modification of AISI 316L SS by pulsed nitrogen ion beams generated in dense plasma focus discharges. *Surf. Coat. Technol.* **204**, 1193–1199 (2010). doi:[10.1016/j.surfcoat.2009.10.034](https://doi.org/10.1016/j.surfcoat.2009.10.034)
107. M. Sadiq, M. Shafiq, A. Waheed, R. Ahmad, M. Zakaullah, Amorphization of silicon by ion irradiation in dense plasma focus. *Phys. Lett. A* **352**, 150–154 (2006). doi:[10.1016/j.physleta.2005.11.058](https://doi.org/10.1016/j.physleta.2005.11.058)
108. M. Sadiq, S. Ahmad, M. Shafiq, M. Zakaullah, Nitrogen ion implantation of silicon in dense plasma focus. *Nuclear Instrum. Methods Phys. Res. Sect. B-Beam Interact. Mat. Atoms* **252**, 219–224 (2006). doi:[10.1016/j.nimb.2006.08.020](https://doi.org/10.1016/j.nimb.2006.08.020)
109. H. Bhuyan et al., Effect of high energy ion irradiation on silicon substrate in a pulsed plasma device. *Appl. Surf. Sci.* **254**, 197–200 (2007). doi:[10.1016/j.apsusc.2007.07.029](https://doi.org/10.1016/j.apsusc.2007.07.029)
110. H. Bhuyan et al., Formation of hexagonal silicon carbide by high energy ion beam irradiation on Si(100) substrate. *J. Phys. D-Appl. Phys.* **40**, 127–131 (2007). doi:[10.1088/0022-3727/40/1/003](https://doi.org/10.1088/0022-3727/40/1/003)
111. Z.R. Wang, H.R. Yousefi, Y. Nishino, H. Ito, K. Masugata, Preparation of silicon carbide film by a plasma focus device. *Phys. Lett. A* **372**, 7179–7182 (2008). doi:[10.1016/j.physleta.2008.10.062](https://doi.org/10.1016/j.physleta.2008.10.062)
112. S. Jabbar, I.A. Khan, R. Ahmad, M. Zakaullah, J.S. Pan, Carbonitriding of silicon using plasma focus device. *J. Vac. Sci. Technol., A* **27**, 381–387 (2009). doi:[10.1116/1.3085720](https://doi.org/10.1116/1.3085720)
113. M. Ahmad, S. Al-Hawat, M. Akel, Porous structure formation on silicon surface treated by plasma focus device. *J. Fusion Energy* **32**, 471–478 (2013). doi:[10.1007/s10894-013-9596-y](https://doi.org/10.1007/s10894-013-9596-y)
114. M.V. Roshan et al., High energy ions and energetic plasma irradiation effects on aluminum in a Filippov-type plasma focus. *Appl. Surf. Sci.* **255**, 2461–2465 (2008). doi:[10.1016/j.apsusc.2008.07.152](https://doi.org/10.1016/j.apsusc.2008.07.152)

115. Z.S. Rad, M. Shahriari, F.A. Davani, Investigation of spatial distribution of hydrogen and argon ions and effects of them on aluminum samples in a 2.5 kJ mater type plasma focus device. *J. Fusion Energy* **30**, 358–366 (2011). doi:[10.1007/s10894-011-9405-4](https://doi.org/10.1007/s10894-011-9405-4)
116. M. Afrashteh, M. Habibi, Study of dense nitrogen plasma irradiation of aluminum targets by APF plasma focus device. *J. Fusion Energy* **31**, 223–226 (2012). doi:[10.1007/s10894-011-9463-7](https://doi.org/10.1007/s10894-011-9463-7)
117. L. Rico, B.J. Gomez, J. Feugeas, O. de Sanctis, Crystallization of amorphous zirconium thin film using ion implantation by a plasma focus of 1 kJ. *Appl. Surf. Sci.* **254**, 193–196 (2007). doi:[10.1016/j.apsusc.2007.07.028](https://doi.org/10.1016/j.apsusc.2007.07.028)
118. I.A. Khan et al., Nitridation of zirconium using energetic ions from plasma focus device. *Thin Solid Films* **516**, 8255–8263 (2008). doi:[10.1016/j.tsf.2008.03.012](https://doi.org/10.1016/j.tsf.2008.03.012)
119. I.A. Khan et al., Synthesis of zirconium oxynitride (ZrON) nanocomposite films on zirconium substrate by dense plasma focus device. *Int. J. Mod. Phys. B* **22**, 3941–3955 (2008)
120. I.A. Khan et al., Synthesis of nano-crystalline zirconium aluminium oxynitride (ZrAlON) composite films by dense plasma Focus device. *Appl. Surf. Sci.* **255**, 6132–6140 (2009). doi:[10.1016/j.apsusc.2009.01.066](https://doi.org/10.1016/j.apsusc.2009.01.066)
121. I.A. Khan et al., Deposition of zirconium carbonitride composite films using ion and electron beams emitted from plasma focus device. *Nucl. Instrum. Methods Phys. Res. Sect. B-Beam Interact. Mat. Atoms* **268**, 2228–2234 (2010). doi:[10.1016/j.nimb.2010.03.030](https://doi.org/10.1016/j.nimb.2010.03.030)
122. G. Murtaza et al., Carburizing of zirconium using a low energy Mather type plasma focus. *Surf. Coat. Technol.* **205**, 3012–3019 (2011). doi:[10.1016/j.surfcoat.2010.11.015](https://doi.org/10.1016/j.surfcoat.2010.11.015)
123. I.A. Khan, R.S. Rawat, R. Ahmad, M.A.K. Shahid, Deposition of alumina stabilized zirconia at room temperature by plasma focus device. *Appl. Surf. Sci.* **288**, 304–312 (2014). doi:[10.1016/j.apsusc.2013.10.025](https://doi.org/10.1016/j.apsusc.2013.10.025)
124. S.R. Mohanty et al., Energetic ion irradiation of American diamond in a plasma focus device and characterization of irradiated material. *Nucl. Instrum. Methods Phys. Res. Sect. B-Beam Interact. Mat. Atoms* **243**, 113–118 (2006). doi:[10.1016/j.nimb.2005.07.199](https://doi.org/10.1016/j.nimb.2005.07.199)
125. M. Bhuyan, S.R. Mohanty, C.V.S. Rao, P.A. Rayjada, P.M. Raole, Plasma focus assisted damage studies on tungsten. *Appl. Surf. Sci.* **264**, 674–680 (2013). doi:[10.1016/j.apsusc.2012.10.093](https://doi.org/10.1016/j.apsusc.2012.10.093)
126. J. Siddiqui et al., Growth and study of plasma assisted nanostructured hard tantalum nitride thin films. *J. Fusion Energy* **34**, 1193–1202 (2015). doi:[10.1007/s10894-015-9943-2](https://doi.org/10.1007/s10894-015-9943-2)
127. V.A. Gribkov, et al., Experimental studies of radiation resistance of boron nitride, C2C ceramics Al₂O₃ and carbon-fiber composites using a PF-1000 plasma-focus device. *Physica Scripta* **83**, doi:[10.1088/0031-8949/83/04/045606](https://doi.org/10.1088/0031-8949/83/04/045606) (2011)
128. M. Habibi, M.H.S. Alavi, Argon ion beam interaction on polyethylene terephthalate surface by a 4 kJ plasma focus device. *Pramana-J. Phys.* **86**, 599–607 (2016). doi:[10.1007/s12043-015-1024-6](https://doi.org/10.1007/s12043-015-1024-6)
129. R.S. Rawat, Dense plasma focus—from alternative fusion source to versatile high energy density plasma source for plasma nanotechnology. *15th Latin American Workshop on Plasma Physics (Lawpp 2014) and 21st Iaea Tm on Research Using Small Fusion Devices (Rusfd)* **591**, doi:[10.1088/1742-6596/591/1/012021](https://doi.org/10.1088/1742-6596/591/1/012021) (2015)
130. M. Chernyshova et al., Interaction of powerful hot plasma and fast ion streams with materials in dense plasma focus devices. *Fusion Eng. Des.* **113**, 109–118 (2016). doi:[10.1016/j.fusengdes.2016.11.003](https://doi.org/10.1016/j.fusengdes.2016.11.003)
131. R. Sagar, M.P. Srivastava, Amorphization of thin film of CdS due to ion irradiation by dense plasma focus. *Phys. Lett. A* **183**, 209–213 (1993)
132. P. Agarwala, S. Annapoorni, M.P. Srivastava, R.S. Rawat, P. Chauhan, Magnetite phase due to energetic argon ion irradiation from a dense plasma focus on hematite thin film. *Phys. Lett. A* **231**, 434–438 (1997)

133. R.S. Rawat et al., Effect of argon ion irradiation on Sb₂Te₃ films in a dense plasma focus device. *Mater. Res. Bull.* **35**, 477–486 (2000)
134. R.S. Rawat, P. Arun, A.G. Vedeshwar, P. Lee, S. Lee, Effect of energetic ion irradiation on CdI₂ films. *J. Appl. Phys.* **95**, 7725–7730 (2004). doi:[10.1063/1.1738538](https://doi.org/10.1063/1.1738538)
135. S. Karamat et al., Nitrogen doping in pulsed laser deposited ZnO thin films using dense plasma focus. *Appl. Surf. Sci.* **257**, 1979–1985 (2011). doi:[10.1016/j.apsusc.2010.09.038](https://doi.org/10.1016/j.apsusc.2010.09.038)
136. J.J. Lin, et al., FePt nanoparticle formation with lower phase transition temperature by single shot plasma focus ion irradiation. *J. Phys. D-Appl. Phys.* **41**, doi:[10.1088/0022-3727/41/13/135213](https://doi.org/10.1088/0022-3727/41/13/135213) (2008)
137. Z.Y. Pan et al., Nanostructuring of FePt thin films by plasma focus device: pulsed ion irradiation dependent phase transition and magnetic properties. *Appl. Phys. A-Mat. Sci. Process.* **96**, 1027–1033 (2009). doi:[10.1007/s00339-009-5138-x](https://doi.org/10.1007/s00339-009-5138-x)
138. Z.Y. Pan et al., Lowering of L1(0) phase transition temperature of FePt thin films by single shot H⁺ ion exposure using plasma focus device. *Thin Solid Films* **517**, 2753–2757 (2009). doi:[10.1016/j.tsf.2008.11.113](https://doi.org/10.1016/j.tsf.2008.11.113)
139. M.P. Srivastava, S.R. Mohanty, S. Annapoorni, R.S. Rawat, Diode like behaviour of an ion irradiated polyaniline film. *Phys. Lett. A* **215**, 63–68 (1996)
140. D.E. Alexander, L.E. Rehn, P.M. Baldo, Y. Gao, *Appl. Phys. Lett.* **62**, 1597 (1993)
141. R.S. Rawat, W.M. Chew, P. Lee, T. White, S. Lee, Deposition of titanium nitride thin films on stainless steel - AISI 304 substrates using a plasma focus device. *Surf. Coat. Technol.* **173**, 276–284 (2003). doi:[10.1016/s0257-8972\(03\)00628-5](https://doi.org/10.1016/s0257-8972(03)00628-5)
142. R. Gupta, M.P. Srivastava, V.R. Balakrishnan, R. Kodama, M.C. Peterson, Deposition of nanosized grains of ferroelectric lead zirconate titanate on thin films using dense plasma focus. *J. Phys. D-Appl. Phys.* **37**, 1091–1094 (2004). doi:[10.1088/0022-3727/37/7/022](https://doi.org/10.1088/0022-3727/37/7/022)
143. R.S. Rawat, T. Zhang, K.S.T. Gan, P. Lee, R.V. Ramanujan, Nano-structured Fe thin film deposition using plasma focus device. *Appl. Surf. Sci.* **253**, 1611–1615 (2006). doi:[10.1016/j.apsusc.2006.02.047](https://doi.org/10.1016/j.apsusc.2006.02.047)
144. T. Zhang, K.S.T. Gan, P. Lee, R.V. Ramanujan, R.S. Rawat, Characteristics of FeCo nano-particles synthesized using plasma focus. *J. Phys. D-Appl. Phys.* **39**, 2212–2219 (2006). doi:[10.1088/0022-3727/39/10/033](https://doi.org/10.1088/0022-3727/39/10/033)
145. R.S. Rawat et al., Nano-phase titanium dioxide thin film deposited by repetitive plasma focus: Ion irradiation and annealing based phase transformation and agglomeration. *Appl. Surf. Sci.* **255**, 2932–2941 (2008). doi:[10.1016/j.apsusc.2008.08.055](https://doi.org/10.1016/j.apsusc.2008.08.055)
146. Z.Y. Pan, et al., Nanostructured magnetic CoPt thin films synthesis using dense plasma focus device operating at sub-kilojoule range. *J. Phys. D-Appl. Phys.* **42**, 175001, doi:[10.1088/0022-3727/42/17/175001](https://doi.org/10.1088/0022-3727/42/17/175001) (2009)
147. Y. Malhotra, S. Roy, M.P. Srivastava, C.R. Kant, K. Ostrikov, Extremely non-equilibrium synthesis of luminescent zinc oxide nanoparticles through energetic ion condensation in a dense plasma focus device. *J. Phys. D-Appl. Phys.* **42**, 155202, doi:[10.1088/0022-3727/42/15/155202](https://doi.org/10.1088/0022-3727/42/15/155202) (2009)
148. E. Gharehabani et al., Synthesis of nanostructured multiphase Ti(C, N)/a-C films by a plasma focus device. *Nucl. Instrum. Methods Phys. Res. Sect. B-Beam Interact. Mat. Atoms* **268**, 2777–2784 (2010). doi:[10.1016/j.nimb.2010.06.027](https://doi.org/10.1016/j.nimb.2010.06.027)
149. Z.Y. Pan et al., Miniature plasma focus as a novel device for synthesis of soft magnetic FeCo thin films. *Phys. Lett. A* **374**, 1043–1048 (2010). doi:[10.1016/j.physleta.2009.12.037](https://doi.org/10.1016/j.physleta.2009.12.037)
150. G. Macharaga et al., TiO₂ nano-cluster thin films by dense plasma focus and ion implantation effect on its photocatalytic activity. *J. Adv. Oxid. Technol.* **14**, 308–313 (2011)
151. G.R. Etaati, M.T. Hosseinejad, M. Ghoranneviss, M. Habibi, M. Shirazi, Deposition of tungsten nitride on stainless steel substrates using plasma focus device. *Nucl. Instrum. Methods Phys. Res. Sect. B-Beam Interact. Mat. Atoms* **269**, 1058–1062 (2011). doi:[10.1016/j.nimb.2011.02.083](https://doi.org/10.1016/j.nimb.2011.02.083)

152. M.T. Hosseinnajad, M. Ghorannevis, G.R. Etaati, M. Shirazi, Z. Ghorannevis, Deposition of tungsten nitride thin films by plasma focus device at different axial and angular positions. *Appl. Surf. Sci.* **257**, 7653–7658 (2011). doi:[10.1016/j.apsusc.2011.03.155](https://doi.org/10.1016/j.apsusc.2011.03.155)
153. S. Javadi, M. Ghorannevis, A. Hojabri, M. Habibi, M.T. Hosseinnajad, Deposition of chromium thin films on stainless steel-304 substrates using a low energy plasma focus device. *J. Fusion Energy* **31**, 242–248 (2012). doi:[10.1007/s10894-011-9461-9](https://doi.org/10.1007/s10894-011-9461-9)
154. S.K. Ngoi et al., Formation of nano-crystalline phase in hydrogenated amorphous silicon thin film by plasma focus ion beam irradiation. *J. Fusion Energy* **31**, 96–103 (2012). doi:[10.1007/s10894-011-9435-y](https://doi.org/10.1007/s10894-011-9435-y)
155. M.T. Hosseinnajad, M. Shirazi, Z. Ghorannevis, M. Ghorannevis, F. Shahgoli, Using mather-type plasma focus device for fabrication of tungsten thin films. *J. Fusion Energy* **31**, 426–431 (2012). doi:[10.1007/s10894-011-9488-y](https://doi.org/10.1007/s10894-011-9488-y)
156. Z.A. Umar et al., Hard $\text{TiC}_x/\text{SiC}/\text{A-C}$: H nanocomposite thin films using pulsed high energy density plasma focus device. *Nucl. Instrum. Methods Phys. Res. Sect. B-Beam Interact. Mat. Atoms* **301**, 53–61 (2013). doi:[10.1016/j.nimb.2013.03.007](https://doi.org/10.1016/j.nimb.2013.03.007)
157. J.J. Lin, et al., Backward plume deposition as a novel technique for high deposition rate Fe nanoclusters synthesis. *Nanotechnology* **18**, doi:[10.1088/0957-4484/18/11/115617](https://doi.org/10.1088/0957-4484/18/11/115617) (2007)
158. K.S. Tan, R.J. Mah, R.S. Rawat, Dense plasma focus device based high growth rate room temperature synthesis of nanostructured zinc oxide thin films. *IEEE Trans. Plasma Sci.* **43**, 2539–2546 (2015). doi:[10.1109/tps.2015.2445055](https://doi.org/10.1109/tps.2015.2445055)
159. L. García-Gancedo et al., Room-temperature remote-plasma sputtering of c-axis oriented zinc oxide thin films. *J. Appl. Phys.* **112**, 014907 (2012)
160. C. Sima et al., Porous nanostructured ZnO films deposited by picosecond laser ablation. *Mater. Sci. Eng., B* **177**, 1188–1193 (2012)
161. S. Lee et al., High rep rate high performance plasma focus as a powerful radiation source. *IEEE Trans. Plasma Sci.* **26**, 1119–1126 (1998)
162. S. Stauss, Y. Imanishi, H. Miyazoe, K. Terashima, High rate deposition of ZnO thin films by a small-scale inductively coupled argon plasma generated in open air. *J. Phys. D Appl. Phys.* **43**, 155203 (2010)
163. C. James, B. Bures, R. Madden, M. Krishnan, R. Adler, in *2011 IEEE Pulsed Power Conference*, pp. 1522–1525 (IEEE)
164. U. Ilyas et al., Enhanced ferromagnetic response in ZnO: Mn thin films by tailoring composition and defect concentration. *J. Magn. Magn. Mater.* **344**, 171–175 (2013). doi:[10.1016/j.jmmm.2013.05.040](https://doi.org/10.1016/j.jmmm.2013.05.040)
165. U. Ilyas et al., Alteration of Mn exchange coupling by oxygen interstitials in ZnO: Mn thin films. *Appl. Surf. Sci.* **258**, 6373–6378 (2012). doi:[10.1016/j.apsusc.2012.03.043](https://doi.org/10.1016/j.apsusc.2012.03.043)
166. U. Ilyas, et al., Oxygen rich p-type ZnO thin films using wet chemical route with enhanced carrier concentration by temperature-dependent tuning of acceptor defects. *J. Appl. Phys.* **110**, doi:[10.1063/1.3660284](https://doi.org/10.1063/1.3660284) (2011)
167. S. Karamat et al., Ferromagnetism in ZnCoO thin films deposited by PLD. *Appl. Phys. A-Mat. Sci. Process.* **101**, 717–722 (2010). doi:[10.1007/s00339-010-5928-1](https://doi.org/10.1007/s00339-010-5928-1)
168. S. Karamat et al., Structural, optical and magnetic properties of $(\text{ZnO})(1-x)(\text{MnO}_2)(x)$ thin films deposited at room temperature. *Appl. Surf. Sci.* **254**, 7285–7289 (2008). doi:[10.1016/j.apsusc.2008.05.318](https://doi.org/10.1016/j.apsusc.2008.05.318)
169. D. Mardare, A. Stancu, On the optical constants of TiO_2 thin films. *Ellipsometric stud. Mat. Res. Bull.* **35**, 2017–2025 (2000). doi:[10.1016/s0025-5408\(00\)00408-6](https://doi.org/10.1016/s0025-5408(00)00408-6)
170. D. Mardare, M. Tasca, M. Delibas, G.I. Rusu, On the structural properties and optical transmittance of TiO_2 r.f. sputtered thin films. *Appl. Surf. Sci.* **156**, 200–206 (2000). doi:[10.1016/s0169-4332\(99\)00508-5](https://doi.org/10.1016/s0169-4332(99)00508-5)
171. B. Lin, Z. Fu, Y. Yia, *Appl. Phys. Lett.* **79**, 943 (2001)

172. J.J. Lin, et al., FePt: Al₂O₃ nanocomposite thin films synthesized by magnetic trapping assisted pulsed laser deposition with reduced intergranular exchange coupling. *J. Phys. D-Appl. Phys.* **41**, doi:[10.1088/0022-3727/41/9/095001](https://doi.org/10.1088/0022-3727/41/9/095001) (2008)
173. Y. Wang et al., Elimination of impurity phase formation in FePt magnetic thin films prepared by pulsed laser deposition. *Appl. Surf. Sci.* **288**, 381–391 (2014). doi:[10.1016/j.apsusc.2013.10.036](https://doi.org/10.1016/j.apsusc.2013.10.036)
174. Z.Y. Pan et al., Oriented growth of CoPt nanoparticles by pulsed laser deposition. *Appl. Phys. A-Mat. Sci. Process.* **101**, 609–613 (2010). doi:[10.1007/s00339-010-5937-0](https://doi.org/10.1007/s00339-010-5937-0)
175. J. Moreno, P. Silva, L. Soto, Optical observations of the plasma motion in a fast plasma focus operating at 50J. *Plasma Sources Sci. Technol.* **12**, 39–45 (2003)

Plasma Science and Technology for Emerging
Economies

An AAAPT Experience

Rawat, R.S. (Ed.)

2017, VI, 805 p. 418 illus., 220 illus. in color., Hardcover

ISBN: 978-981-10-4216-4